

FRICTION MODELING, IDENTIFICATION AND COMPENSATION

THÈSE N° 1988 (1999)

PRÉSENTÉE AU DÉPARTEMENT DE GÉNIE MÉCANIQUE

ÉCOLE POLYTECHNIQUE FÉDÉRALE DE LAUSANNE

POUR L'OBTENTION DU GRADE DE DOCTEUR ÈS SCIENCES TECHNIQUES

PAR

Friedhelm ALTPETER

Ingénieur en microtechnique diplômé EPF
de nationalité suisse et originaire d'Ausserbinn (VS)

acceptée sur proposition du jury:

Prof. R. Longchamp, directeur de thèse
Prof. D. M. Auslander, rapporteur
Dr C. Canudas de Wit, rapporteur
Prof. A. Curnier, rapporteur
Dr M. Kocher, rapporteur
Dr P. Myszkowski, rapporteur

Lausanne, EPFL
1999

To my parents

*The people walking in darkness have seen a great light;
on those living in the land of the shadow of death a light
has dawned.*

Isaiah 9

Preface

SYSTEMS with friction offer many interesting topics for research, mainly in Switzerland where people are surrounded by numerous applications related to the use, reduction, or compensation of friction. In winter, for example, downhill skiing requires a minimization of the friction force between the snow and the skis. At the same time, driving a car requires chains on steep roads in order to maximize the adhesion between the ground and the wheels. Another popular sport, practiced during the whole year, is rock-climbing. Here the friction force between the rock and the special shoes is an essential element for a success in the route engaged.

Besides everyday applications of friction in transports and sports, Switzerland is the home of micro-mechanics in watchmaker industry. Furthermore, many machine-tool manufacturers are faced with the problems of friction in their axis drives. These industries are collaborating intensively with the two technical universities at Zürich and Lausanne, in order to improve understanding of their problems, to find interesting solutions, and to reduce the cost of their products.

All these ingredients form an excellent foundation for this PhD-thesis, together with the exceptional working environment at the Institut d'automatique, École Polytechnique Fédérale de Lausanne. Many people contributed to the success of this work: first I would like to thank the professors Roland Longchamp and Dominique Bonvin for the employment at the Institut d'automatique and their interest in the results presented in this PhD-thesis. My gratitude also belongs to my supervisor Dr. Piotr Myszkowski for the time and effort he spent for this work. For the excellent collaboration, their interest in research, and the reception (including the pies after lunch), I would like to thank all the people from Charmilles Technologies S.A., Meyrin, and especially Mr. Jean Waelti for his patience, Dr. Michel Kocher for his criticism, Mr. René Demellayer for allowing us to work with his machine, and Dr. André Grosjean and Dr. Jorge Cors for their support. Finally, I would like to express my gratitude to Prof. Fathi Ghorbel, Rice University, Houston, Texas, and Prof. Dan-Sorin Neculescu, University of Ottawa, for the collaboration and the visit at their universities in fall 1997.

Other people helped in solving the everyday problems that appeared during my stay at the Institut d'automatique: Marie-Claire our secretary, Titof in the electronics and mechanics shop, Christophe the ‘mister real-time’, and Martin an excellent partner for discussions and rock-climbing.

This research was supported financially by the Commission pour la Technologie et l’Innovation (CTI) from the Swiss government under grant nos. 2874.1 and 3444.1.

Friedhelm Altpeter, June 8, 1999.

Abstract

HIGH-PRECISION tracking requires excellent control of slow motion and positioning. Recent advances have provided dynamic friction models that represent almost all experimentally observed properties of friction. The state space formulation of these new mathematical descriptions has the property that the state derivatives are continuous functions. This enables the application of established theories for nonlinear systems. The existence of locally stable fixed points does not imply for nonlinear systems the absence of limit cycles (periodic orbits) or unstable solutions. Therefore, global properties of PI velocity and PID position control are analyzed using a passivity and Lyapunov based approach. These linear control laws are then extended by nonlinear components based on the friction model considered. The applications presented in this work are in the domains of mechatronics and machine-tools.

Version abrégée

L'ASSERVISSEMENT de haute précision d'entraînements vise à la maîtrise de mouvements lents et du positionnement. Récemment, des modèles dynamiques ont été proposés, modèles qui représentent la plupart des phénomènes de frottement observés expérimentalement. Dans la représentation d'état de ces nouvelles descriptions mathématiques, la dérivée de l'état est une fonction continue. Ceci permet l'application des théories établies au sujet de systèmes non linéaires. L'existence de points d'équilibre localement stables n'implique pas, pour un système non linéaire, l'absence de cycles limites (trajectoires périodiques) ou de solutions instables. Les propriétés globales des boucles de réglage PI de vitesse et PID de position sont alors analysées en utilisant les approches de passivité et de Lyapunov. Ces lois de commande linéaires sont ensuite améliorées par des contributions non linéaires à la commande basées sur le modèle du frottement considéré. Les applications qui sont présentées proviennent des domaines de la mécatronique et des machines-outils.

Zusammenfassung

HOCHPRÄZISIONSANSTEUERUNGEN von Antrieben bezwecken das Erzielen vorgegebener Kriechbewegungen und das Erreichen einer genauen Achsenpositionierung. Vor kurzem wurden Reibmodelle vorgestellt, die die meisten beobachteten Reibeigenschaften beinhalten. In den Zustandsgleichungen dieser neuen mathematischen Beschreibungen sind die Ableitungen der Zustände nach der Zeit kontinuierliche Funktionen. Dies ermöglicht die Anwendung verbreiteter Theorien für nichtlineare Systeme. Örtlich stabile Fixpunkte, sowie Grenzzyklen (periodische Schwingungen) und instabile Lösungen des Anfangswertproblems, können bei einem nichtlinearen System gleichzeitig auftreten. Daher sind die globalen Eigenschaften von PI Geschwindigkeits- und PID Positionsregelkreisen zu untersuchen, was mittels Passivität von Untergruppen und der Lyapunovmethode möglich ist. Diese linearen Regler werden anschliessend durch das Hinzufügen reibmodellbasierter nichtlinearer Elemente verbessert. Die vorgestellten Anwendungen stammen aus den Bereichen Mechatronik und Werkzeugmaschinen.

Contents

Notations	xvi
1 Introduction	1
1.1 Motivation and Domain of Application	1
1.2 Problem Formulation and Postulations	3
1.3 Topics Considered	5
1.4 State of the Art	5
1.5 Organization of the Thesis	7
2 Tribology	9
2.1 Normal Loading of Rough Surfaces	10
2.2 Interface Properties and Lubrication	13
2.2.1 Dry Contact	14
2.2.2 Boundary Lubrication	14
2.2.3 Elasto-hydrodynamic Lubrication	15
2.2.4 Mathematical Descriptions	15
2.3 Longitudinal Loading of Rough Surfaces	16
2.3.1 Distributed Element Hysteresis Model	16
2.3.2 Stiffness at Rest	18
2.3.3 Viscous Damping for Presliding	19
2.3.4 Break-away force	19
2.3.5 Transition from Sticking to Sliding	20
2.4 Current Trends in Tribology and Summary	21
3 Integrated Friction Modeling	23
3.1 Kinetic Friction Model (KFM)	24
3.1.1 Closed Form Mathematical Description	24
3.1.2 Model Properties	26
3.1.3 Simulation Aspects	27
3.2 Lund-Grenoble (<i>LuGre</i>) Model	27
3.2.1 Brief Description	29
3.2.2 Model Properties	29
3.2.3 Limitations	33
3.3 Comparison of the Two Friction Models	33
3.3.1 Small Parameter: Characteristic Space Constant	34

3.3.2	Explicit Separation of Dynamics	34
3.3.3	Friction Force Prediction: Unidirectional Motion	35
3.3.4	Friction Force Prediction: Zero velocity transition at constant acceleration	37
3.3.5	Discussion of Model Complexity Required	39
3.4	Model Parameter Identification	39
3.4.1	Steady-State Velocity–Friction Force Characteristics	40
3.4.2	High Speeds without Velocity Reversal	41
3.4.3	Small Displacements (Presliding)	42
3.4.4	Dahl’s Curve	44
3.4.5	Discussion of Model Parameter Identification	44
3.5	Integrated Friction Modeling: A Summary	45
4	Synthesis of PID Controllers	47
4.1	PI Velocity Control	48
4.1.1	Time-Domain Phenomena	48
4.1.2	Closed-Loop Synthesis	50
4.1.3	Global Stability	50
4.1.4	Local Asymptotic Stability	53
4.1.5	Global Asymptotic Stability	56
4.1.6	Relevance of the Results for PI Velocity Regulation	65
4.2	PID Position Control	66
4.2.1	Time-Domain Phenomena	66
4.2.2	Simplified PID Synthesis	67
4.2.3	Global Asymptotic Stability	69
4.3	Discussion of Results	71
5	Enhanced Regulation and Tracking Performance	73
5.1	Feedforward Friction Compensation	74
5.1.1	KFM Based Compensation Applied to the <i>LuGre</i> Model	74
5.1.2	<i>LuGre</i> Model Based Compensation	75
5.1.3	Robust Stability	77
5.1.4	Adaptive <i>LuGre</i> Model Based Compensation	79
5.2	Friction State Observers	81
5.2.1	Tracking Error Based Correction	81
5.2.2	Luenberger-like State Observer	82
5.3	Input–Output Linearization by State Feedback	86
5.3.1	KFM Based Compensation Applied to the <i>LuGre</i> Model	86
5.3.2	<i>LuGre</i> Model Based Compensation	88
5.4	Discussion	89
6	Applications	91
6.1	Lubricant Selection	92
6.2	Modeling of an Inertial Drive	93
6.2.1	Description of the Setup	93

6.2.2	Simple Control	95
6.2.3	Analysis of the V-Bearing	96
6.2.4	Modeling	98
6.3	Control of a Vertical Axis for EDM	101
6.3.1	Brief Description of the EDM Process	102
6.3.2	Drive of the Vertical Axis and Overall Control Structure	104
6.3.3	Identification Results	105
6.3.4	PI Velocity Control	109
6.3.5	PID Position Control	110
6.3.6	Feedforward Friction Compensation	113
6.3.7	Input–Output Linearization by State Feedback	114
6.3.8	Catalogue of solutions	116
7	Conclusions	119
7.1	Relevance of the Methodologies Proposed	119
7.2	Further Research Directions	120
A	Modeling of Complex Systems	123
A.1	Bond Graphs for Mechanical Systems	123
A.2	From Bond Graphs to Ordinary Differential Equations	125
B	C-Code Program Listing: Real-Time Task	127
Bibliography		135
Curriculum Vitae		143
List of Publications		145
Index		147

List of Figures

1.1 Principal domain of application: machine-tools.	2
1.2 Problem formulation and postulations.	4
2.1 Engineering surface resulting from milling.	10
2.2 Two dimensional contact model.	11
2.3 Lubrication regimes.	14
2.4 Distributed element hysteresis model.	17
2.5 Shearing of one asperity.	18
3.1 Kinetic friction model.	25
3.2 Properties of kinetic friction model.	26
3.3 Input-output phenomena, captured by the <i>LuGre</i> model.	28
3.4 System passivity.	31
3.5 Limitations of the <i>LuGre</i> model.	33
3.6 Dynamic friction force lags KFM (simulation data).	37
3.7 Zero velocity transition at constant acceleration.	39
3.8 Illustration of particular regimes used for identification.	40
3.9 Acquisition in closed-loop.	42
3.10 Comparison of identification results based on different experiments.	45
4.1 Time-domain phenomena for PI velocity control.	49
4.2 Functional analysis: dependence of $\ h_v(t)\ _1$ on λ for $\eta = 1$.	52
4.3 Block diagram: linearization for PI velocity control.	54
4.4 Root-locus analysis: linearization for PI velocity control with $F_s > F_c$.	55
4.5 Limit cycles observed with PI velocity control (simulation data).	57
4.6 Block diagram PI velocity control.	58
4.7 PI velocity regulation—Lyapunov analysis.	60
4.8 PI velocity regulation—stability criterion.	62
4.9 Time-domain phenomena for PID position control: the hunting effect.	67
4.10 Bode analysis of the quasi linear regimes.	68
4.11 Block diagram for PID position control.	70
5.1 Block diagram for model based feedforward friction compensation.	74
5.2 Block diagram for cascaded control loops.	76
5.3 Feedforward robustness analysis.	78
5.4 Block diagram for adaptive model based feedforward friction compensation.	80
5.5 Block diagram of a Luenberger-like state observer for a drive with friction.	83

5.6	Block diagram for input–output linearization by state feedback.	86
5.7	Performance of KFM friction compensation based on sensed velocity.	87
6.1	Lubricant selection.	92
6.2	Photograph of an inertial drive.	94
6.3	Drawing of an inertial drive.	94
6.4	Simple stick-slip control.	95
6.5	Description of the races analyzed.	96
6.6	Experimental verification of tribological results.	97
6.7	Bond graph of an inertial drive.	98
6.8	Electrical discharge machining.	101
6.9	Operation of electrical discharge machining.	103
6.10	Scheme of a vertical axis drive and block diagram for EDM control.	104
6.11	Identification: steady-state characteristics.	105
6.12	Identification: dynamics for presliding.	106
6.13	Identification: Dahl’s curve.	107
6.14	Performance of PI velocity control.	109
6.15	Performance of PID positioning.	111
6.16	PID positioning: simplified synthesis with Bode plots.	112
6.17	Sinus tracking: PD, PID, and PID with <i>LuGre</i> feedforward.	114
6.18	Sinus tracking: input–output linearization.	116
A.1	Graphical representations of a drive with friction.	125

List of Tables

2.1	Models describing the relationship between velocity and friction force.	16
6.1	Statistical parameters of equivalent surface.	96
6.2	Numerical values for a vertical EDM axis (in parenthesis, the values with only limited confidence).	108
6.3	Parameters for real-time experiments (position control).	115
6.4	Catalogue of solutions for position control.	117
A.1	Software packages for object oriented modeling.	124

Notations

Chapter 2

β	spectrum width parameter
δ	asperity deformation
Λ	electrical conductance
ν	Poisson ratio
ρ	dimensionless peak radius
σ_0	stiffness
$\sigma_0 g(\cdot)$	nonlinearities of velocity–friction force characteristics
σ_1	surface material (viscous) damping
σ_2	viscous friction coefficient
τ_B	shear strength
$\varphi(F_{si})$	Coulomb slider strength distribution
ζ	dimensionless peak height

A_r	real area of contact
D_L	peak density
E	Young's modulus
E^*	surface elasticity modulus
F	friction force
F_c	Coulomb level
F_s	break-away force
G	shear modulus
J	inertia (mass)
L	contact length
N	number of asperities
P_x	longitudinal load
P_z	normal load
R	asperity radius
$2a$	contact width
$f(\zeta, \rho)$	joint probability density function describing topology of rough surface
b	width of apparent area of contact

i	Dahl model exponent
s	standard deviation of surface height
\dot{s}	standard deviation of surface slope
\ddot{s}	standard deviation of surface curvature
t	dimensionless surface height
v_s	characteristic velocity of velocity–friction force characteristics
x	direction longitudinal to motion
\tilde{x}	deviation from position at rest
\dot{x}	relative velocity
y	direction transversal to motion
z	direction normal to surface

Chapters 3–5

ϵ	'small' number
σ_0	stiffness at rest
$\sigma_0 g(\cdot)$	nonlinearities of velocity–friction force characteristics
σ_1	surface material (viscous) damping
σ_2	viscous friction coefficient
F	friction torque (force)
F_c	Coulomb level
F_s	break-away torque (force)
F_g	torque (force) caused by amplifier offsets and/or gravity
$G(s)$	transfer function
J	inertia (mass)
S	storage function
T	final time
V	Lyapunov function candidate

e	position tracking error
\dot{e}	velocity tracking error
h	sampling period
kh	sampling time
k_v	velocity feedback gain
k_p	position feedback gain
k_i	integral gain
q	position
\dot{q}	velocity
\ddot{q}	acceleration
r	reference position
t	time
u	torque (force) control action
v_s	characteristic velocity of velocity–friction force characteristics
w	perturbation signal
x	state vector
x_s	characteristic space constant
z	friction state
\mathcal{L}_2	set of finite energy signals
\mathcal{L}_∞	set of bounded signals
$\ u(t)\ _1 = \int u(t) dt$	one-norm
$\ u(t)\ _2 = \sqrt{\int u(t) ^2 dt}$	two-norm
$\ u(t)\ _\infty = \sup u(t)$	infinity-norm

Chapter 1

Introduction

TN almost all mechanical systems, there are parts in contact undergoing relative motion. Tribology is the science and technology of such interacting surfaces. The popular associated terms are friction, wear, and lubrication. This study presents recent control engineering results for drives with friction. For convenience, some terms are defined first:

Tribology: the science of the mechanisms of friction, lubrication, and wear of interacting surfaces that are in relative motion.

Friction: a force that resists the tangential relative motion or tendency to such motion of two bodies in contact.

Lubricant: a substance, such as grease or oil, that reduces friction and wear when applied as a surface coating to moving parts.

Wear: is the progressive damage, involving material loss, which occurs on the surface of a component as a result of its motion relative to the adjacent working part; it is almost unavoidable companion of friction.

1.1 Motivation and Domain of Application

Friction is present in almost any industrial drive. This plus the fact that friction phenomena are nonlinear make the topics of friction modeling, identification and compensation very interesting and challenging.

These three topics are discussed herein mainly in the context of machine-tools. Some machine parts considered are shown in Figure 1.1: (a) a ballscrew-and-nut transmission that is used to transform rotational into linear motion, and (b) a linear roller bearing that is widely used to guide the tools and the table of a machine-tool. Other machine elements experiencing friction are preloaded ball bearings, motor brushes, harmonic gear drives *etc.*

Although not directly related to problems of drive control, it is useful to look back at some elements of the history of tribology [37]. In early civilizations, tribology was primarily the technology of wear, lubrication, and mechanical friction force reduction. The optimization of wear was, for example, used to increase the efficiency of hole drilling. The first lubricants that were introduced between surfaces in relative motion were water or animal fat. In order to achieve additional friction force reduction, wheels or logs were used in transportation.

a) Ballscrew-and-nut transmission



b) Linear roller bearing

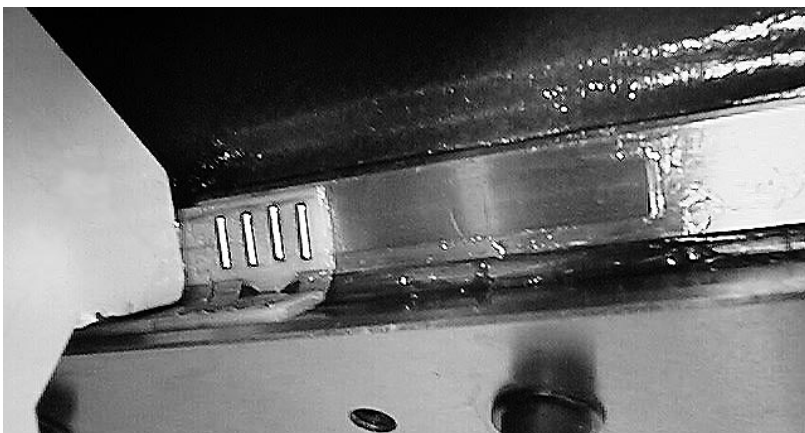


Figure 1.1: Principal domain of application: machine-tools.

In the past, the physical topics of friction were discussed mainly by material scientists and mechanical design engineers. The aspects of control engineering have been introduced with adequate rigor only later [5]. The fundamentals for advanced friction compensation have been presented recently by the group working at Lund and Grenoble [27]. The relevance of their contribution is mainly the successful use of an integrated friction model for synthesis of an enhanced controller that achieves efficient friction compensation for a simple drive.

In order to provide a generic solution for the control of drives with friction, a large variety of aspects are discussed here: starting with a description of the physical phenomena, continuing with the integrated friction modeling and parameter identification, and finishing with the standard and the advanced methodologies of friction force compensation.

1.2 Problem Formulation and Postulations

The problem solved herein is the synthesis of a stable control with desired performance for drives with friction. The approach proposed is based on two steps: (i) modeling of the drive that is specified with technical drawings, and (ii) synthesis of the controller. This is illustrated in Figure 1.2. The simple drives considered here are formed of a motor, a load, bearings and a position/velocity sensor. The friction is introduced by the bearings and by the brushes of the motor (if a DC motor is used).

In the first step towards a solution of the control problem, modeling of the drive is considered. The mathematical model that results should have the following properties: (i) the model structure should be complex enough to capture the dominant phenomena observed; (ii) the parameters of the model are selected such that a specified cost-function is optimized, expressing the fact that the difference is minimized between the data predicted by the model and observed experimentally; and (iii) after parameter identification and for a particular application considered, it is possible to reduce appropriately the complexity of the model. The postulations proposed for this first phase are the following:

Identification methodology. Classical identification methods do not apply directly to the determination of the model parameters for a given setup, since friction is a nonlinear phenomenon. However, it is observed that various particular experiments can be used for the identification of reduced parameter sets. With three experiments, it is possible to estimate all the parameters for a simple drive with friction.

Model order reduction. A relationship between complex modern and simple classical models can be established with a singular perturbation approach. This theory allows rigorous model order reduction (*i.e.* model simplification) in certain particular cases. The analysis suggests the existence of a fundamental parameter, the characteristic space constant, that decides whether a displacement analyzed is ‘small’ or ‘large’. It results that the use of modern complex models is required in all situations with ‘small’ displacements.

In the second step, the synthesis of stable control leading to desired behavior is performed. The mathematical model of the system is nonlinear because of the nature of

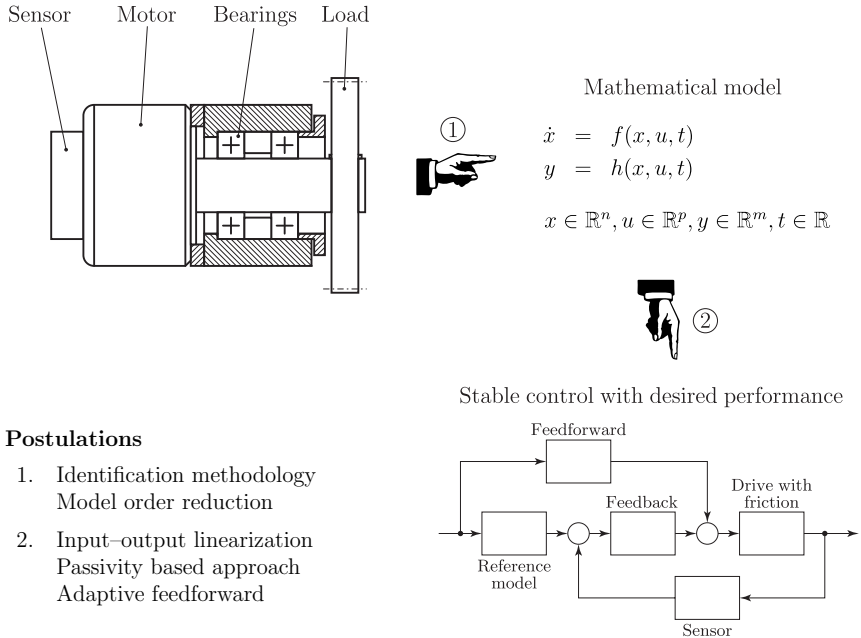


Figure 1.2: Problem formulation and postulations.

friction. This introduces some problems for the analysis of stability of the closed-loop system with a constant reference input. The states are ideally asymptotically stable, but they can also be unstable (escape to infinity), stable with some steady-state tracking error, stable with a periodic, or stable with a chaotic orbit. In addition, feedforward control can be useful to achieve acceptable tracking for a specified frequency spectrum and amplitude range of the reference signal. The postulations proposed for this second phase are the following:

Input-output linearization. In order to achieve acceptable tracking for a large frequency spectrum and a wide amplitude range of the reference signal, it is almost inevitable to apply linearization techniques. Besides the high loop-gain approach, input-output linearization can be achieved either by feedback based on an estimation of the actual states, or by feedforward based on an appropriately generated reference trajectory for the states of the system.

Passivity based approach. The synthesis of the control loop aims normally to achieve global asymptotic stability of the desired operating point. Then the system approaches asymptotically the operating point starting from any initial condition. This goal can be achieved with a passivity based ap-

proach applied to the controller synthesis. This methodology uses the input–output properties of appropriately chosen subsystems, that are interconnected to form the full system. The key concept is that all the subsystems are dissipating some kind of energy. Furthermore, it is possible to apply the operator theory to establish the proofs of robust stability even for reference tracking.

Adaptive feedforward. When different control methodologies are compared in a catalogue of solutions, it results that proportional–integral–derivative (PID) control, enhanced by adaptive feedforward, is the most interesting algorithm. The identification effort is reduced and robust stability is achieved if the adaptation gains are sufficiently small. In addition, acceptable step response and excellent sinus tracking performance are achieved.

1.3 Topics Considered

The objective of this thesis is to discuss the large variety of aspects that need to be considered for the use of drives with friction. This enables establishment of a catalogue of solutions that is useful for the control engineer. The topics considered are the following.

- Introducing the physical phenomena observed for two interacting surfaces
- Providing a mathematical model for each of these phenomena separately
- Considering two models for friction that are well suited for controller synthesis
- Comparing these two models in terms of their ability to predict friction force
- Presenting a methodology for modeling of (complex) drives with friction
- Proposing of a methodology for model parameter identification
- Studying common control approaches
- Motivating and analyzing widely used PI velocity control
- Motivating and analyzing widely used PID position control
- Presenting a survey of methods for performance enhancement
- Proposing solutions to the problem of friction state observation
- Discussing the topic of robustness versus modeling errors
- Illustrating the theoretical considerations of this thesis
- Discussing a particular actuator technology that is based on friction
- Applying PID and enhanced controller synthesis to an industrial drive

1.4 State of the Art

This thesis is based mainly on results in friction modeling and control synthesis presented recently by a group at Lund and Grenoble [27]. They have shown that the tracking performance can be increased with a control algorithm that is based on a model that represents

most of the input–output phenomena that are reported in the literature. Nevertheless, the author is convinced that a detailed study of the physics of friction is useful for the design of high performance drives. This because it is possible to simplify the task of controller synthesis considerably by an appropriate mechanical design and lubrication selection.

Detailed introductions to the subject topics of tribology are available [13], containing mainly definitions for most of the common terms used in the science of contacting surfaces. The statistical model for rough surfaces presented by Greenwood and Williamson [45] and its extension by Francis [41] forms a fundamental concept that is required for the understanding of friction phenomena. Owing to surface roughness, two machine parts are contacting at a large number of small spots, distributed over the whole surface. The properties of each contact point contribute to the overall behavior of the interface and therefore to the observed macroscopic phenomena of friction. This concept has been used before to establish a simple model for distributed element hysteresis [55]. Now it is possible to evaluate the relationship between certain friction model parameters and characteristics of the surface topology and the contacting materials [4].

An extended survey of friction modeling was presented recently [9] including a large number of literature references. Classical friction modeling is based on the experiments of the French scientist de Coulomb [34]. The behavior of a loaded slide on a flat surface was analyzed for different constant pulling forces at various speeds. Later, several dynamic effects, that are associated with friction, have been observed. The Dahl model [32] is a compact mathematical formulation for some of these dynamic phenomena. This model was originally developed for ball bearings, but its structure applies to sliding bearings as well. The recent contribution of a group at Lund and Grenoble [27] is, however, the first literature reference known to the author that uses extensively modern modeling results for controller synthesis. The Lund–Grenoble model has been designed to represent observed input–output behavior by an appropriate extension of the Dahl model. Furthermore, controller synthesis is presented using modern analysis tools for nonlinear systems. Whilst tribological aspects are generally discussed in undergraduate courses for mechanical engineers, the point of view of the control engineer has been introduced only recently. Numerous topics about control of drives with friction are discussed systematically [5, 8]. Analysis of the performances of PID control, considering the Coulomb model with static friction, have been undertaken [7, 91]. Results for an alternative extension of Dahl’s dynamic friction model have been presented, and PID position and PI velocity control has been analyzed [18]. Although these results are insightful for the understanding of the performance of PID control applied to drives with friction, no literature references are known to the author that consider the *LuGre* friction model.

Advanced friction compensation has been subjected to numerous publications that have been summarized recently [9]. It is surprising that, as far as the author knows, Dahl’s friction model which was developed in the late sixties and early seventies has been used for the synthesis of control only in the nineties. In a first step, the Dahl model was subjected to a mathematical analysis of its properties [15, 16]. These results motivated an extension of the Dahl model and a Lyapunov function based stability analysis [26]. Recently, several additional contributions to nonlinear control synthesis have been presented. These literature references are all focusing on input–output linearization by feedback based on the estimated state vector. In a first step, only the nominal pa-

rameter case was considered [2, 27]. Next, adaptive schemes were developed for specific parametric model perturbations that are presumably related to changes in preload or temperature [25, 94].

Two applications are presented at the end of the thesis: an inertial slider actuator and a drive for a vertical machine-tool axis. Inertial drives were developed in the late eighties for probe positioning in scanning tunneling microscopes [75, 80]. If driven by piezocrystals, these new actuators present the advantage that extremely fine positioning (in the nanometer range) is possible with high accuracy and at reasonable cost. The second application is the control of the drive of a vertical axis that is used in a modern machining technology, called Electrical Discharge Machining (EDM). In the EDM process, metal is removed by generating high frequency sparks through a small gap filled with a dielectric fluid. The terms of EDM are defined by standards and the various machines are classified into the two major classes of die-sinkers and wire machines [96]. A complete description of the EDM process and the concepts of machining parameter selection is available [36, 74]. Therein, it is emphasized that the appropriate selection of the polarities for the electrode (tool) and the workpiece is fundamental for an economically interesting operation.

1.5 Organization of the Thesis

The core of the thesis is organized into five chapters. The fundamentals of tribology, that seem to be useful for the control engineer, are summarized in Chapter 2. Models of friction that are well suited for controller synthesis are presented in Chapter 3. The aspects of control are discussed in two steps: (i) standard PID control (Chapter 4), and (ii) performance enhancement by feedforward or feedback (Chapter 5). The methodologies presented are illustrated in Chapter 6. The elements presented chapter by chapter are the following.

Chapter 2 Tribology. The normal loading of rough surfaces is discussed in Section 2.1 recalling modeling of rough surfaces and the evaluation of the real area of contact for a given supported load. A survey of interface properties of dry and lubricated contacts is provided in Section 2.2, leading to an empirical mathematical description of the relationship between friction force and relative velocity. The microscopic behavior for longitudinal loading of rough surfaces is discussed in Section 2.3 presenting, amongst others, a relationship between physical properties of materials and the phenomena observed for small displacements. The chapter is concluded in Section 2.4 with some remarks on current trends in tribology.

Chapter 3 Integrated Friction Modeling. First two widely used models are presented: the Kinetic Friction Model (KFM) in Section 3.1 and Lund-Grenoble (*LuGre*) model in Section 3.2. At the same time, the fundamental properties of each model are discussed. These two models are compared in Section 3.3 with a singular perturbation analysis: their ability to predict the friction force of a simple drive is considered. The results give some indications that help to chose the adequate model complexity for a given situation. The problem of modeling complex mechanical systems with friction between parts

in relative motion remains. The approach, which is briefly summarized in Appendix A, proposes a rigorous methodology to establish the system of differential-algebraic equations even for complex mechanical systems. Finally, a methodology for model parameter identification which is based on four special experiments that are exciting only particular parts of the system is presented in Section 3.4.

Chapter 4 Design of PID Controllers. In Section 4.1 it is shown that PI control is required to stabilize the system for a given (constant) reference velocity. Furthermore, in Section 4.2 it is demonstrated that positioning requires a PID control structure to achieve asymptotic stability of the positioning error. Intuitive understanding of transient behavior is difficult for a global, nonlinear system analysis. Therefore, both control objectives (velocity control and positioning) are also discussed applying linearization techniques.

Chapter 5 Enhanced Regulation and Tracking Performance. First, in Section 5.1 this chapter presents a survey of feedforward friction compensation techniques. In order to realize feedback compensation, in Section 5.2 it is necessary to discuss friction state observers. The resulting estimated state vector is used in Section 5.3 for controller synthesis based on the approach of input-output linearization by state feedback.

Chapter 6 Applications. In this chapter, two applications are presented: (i) the modeling of an inertial drive is presented in Section 6.2, including a tribological study of the surfaces in relative motion; and (ii) the identification and control of the vertical axis of an industrial electro-discharge machining installation is discussed in Section 6.3. At the end a catalogue of solutions for the control of drives with friction is provided.

Chapter 2

Tribology

Objectives

- Introducing the physical phenomena observed for two interacting surfaces
- Providing a mathematical model for each of these phenomena separately

MOST engineering mechanisms are composed of a certain number of interfaces between the machine parts. Therefore, it is mandatory, even for the control engineer, to know some basics of tribology, which is the science and technology of two interacting surfaces in relative motion.

The topics reviewed in this chapter are: (i) the behavior of rough surfaces in contact, (ii) the resistance to motion whenever a solid slides over another which is called friction, and (iii) the influence of lubrication which is the application of materials to the interface in order to produce low friction and wear. The laws of wear, however, are not discussed herein, since the author was rarely faced with problems of the erosion from one or both solid surfaces in sliding, rolling or impact motion relative to one another.

It must be emphasized that the character of this chapter is somewhat encyclopedic, but it is useful for what follows to discuss at least some basics of tribology. Furthermore, a relationship is established between the input-output observation based models and the physical phenomena. This is useful for an optimal mechanical design of drives which reduces the problems encountered afterwards by the control engineer.

Detailed introductions to the topics of tribology are available [13], containing mainly definitions for most of the common terms used in the science of contacting surfaces. Further references are cited in the following sections.

This chapter is organized as follows. The normal loading of rough surfaces is discussed in Section 2.1 recalling modeling of rough surfaces and the evaluation of the real area of contact for a given supported load. A survey of interface properties of dry and lubricated contacts is provided in Section 2.2, leading to an empirical mathematical description of the relationship between friction force and relative velocity. The microscopic behavior for

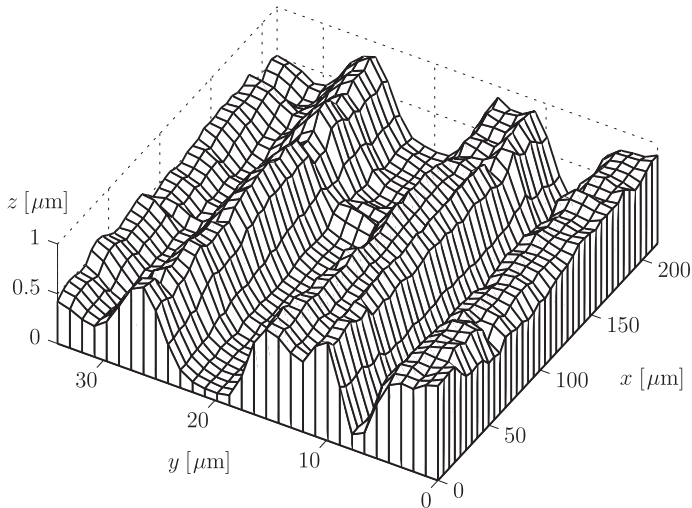


Figure 2.1: Engineering surface resulting from milling.

longitudinal loading of rough surfaces is discussed in Section 2.3 presenting, amongst others, a relationship between physical properties of materials and the phenomena observed for small displacements. The chapter is concluded in Section 2.4 with some remarks on current trends in tribology.

2.1 Normal Loading of Rough Surfaces

Because friction phenomena are related to the interface between mechanical parts, it is necessary in a first step to analyze the behavior of engineering surfaces in contact. The most important observation is the fact that, at a microscopic scale, the surfaces of machine parts look like the land surface of Switzerland with its mountains and valleys, see Figure 2.1. Therefore, when two surfaces are pressed together, they are in contact only at specific spots. The real area of contact is therefore much smaller than the apparent area of contact. This implies that in fact overall friction phenomena result from summing up the behavior of a large number of contact points. The problem of finding a macroscopic model of friction is solved therefore in two steps: (i) a statistical model for rough surfaces is specified; and (ii) the properties of all asperities are summed up, weighted by the probability to find an asperity of the characteristics considered. This approach is used here for establishing the relationship between the normal load and the resulting real area of contact for the interface between two rough surfaces. Note that fundamentally different micromechanisms can lead to the same macroscopic law if such a statistical averaging is applied. This abstraction leads to generic solutions which apply to a large variety of

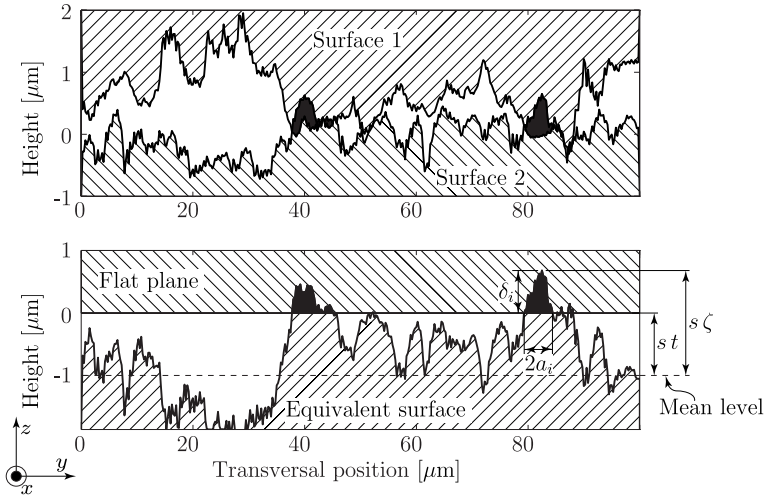


Figure 2.2: Two dimensional contact model.

physical systems.

Without loss of generality consider the contact model illustrated in Figure 2.2. For this two dimensional topology the interface is integrally described by its profile. The longitudinal dimension is obtained simply by translation. Note that a profile contains all necessary information for the evaluation of the real area of contact, also in the case of an isotropic surface topology. For a better understanding, the x -axis (longitudinal), y -axis (transversal) and z -axis (normal) are indicated in this and subsequent Figures. Furthermore, without loss of generality, suppose that motion is along the longitudinal axis. This simplified model is an approximate description for the surface topology illustrated in Figure 2.1.

The evaluation of the real area of contact can be based on the statistical model for rough surfaces, presented first by Greenwood and Williamson and extended later by Francis [41, 45]. Therein, it is assumed that the mechanical contact behavior of two macroscopically plane surfaces is equivalent to loading their algebraic sum, the equivalent surface, against a smooth plane surface. This concept of the equivalent surface is illustrated in Figure 2.2.

The solution of the problem is generalized by considering the dimensionless peak height ζ and surface height t , which are related, see Figure 2.2, to asperity deformation δ and the standard deviation s of the surface height by

$$\frac{\delta}{s} = \zeta - t \quad (2.1)$$

In addition, it is convenient [41] to define the relationship between the dimensionless peak

radius ρ , the asperity radius R , and the standard deviation \bar{s} of surface curvature by

$$\rho = \frac{R\bar{s}}{\sqrt{1.5}} \quad (2.2)$$

A Gaussian joint probability density function of dimensionless peak height and radius is proposed to describe the topology of rough surfaces [70]

$$f(\zeta, \rho) = \frac{\sqrt{3}}{\pi \rho^2 \sqrt{1 - \beta^2}} \left(\frac{1}{\rho^2} - 1 + e^{-\frac{1}{\rho^2}} \right) \cdot e^{-\frac{0.5}{1 - \beta^2} (\zeta^2 - 2\beta \frac{\zeta}{\rho} + \frac{1}{\rho^2})} \quad (2.3)$$

where $\beta = \frac{\sqrt{1.5}\bar{s}^2}{\bar{s}\bar{s}}$ is the spectrum width parameter. The standard deviation of the surface slope is denoted by \bar{s} .

This model is used to evaluate the macroscopic behavior of the surface [41]. Since the properties of the macroscopic contact are evaluated by integration over all asperity contacts, it would be interesting to find an integrable probability function $f(\zeta, \rho)$ instead of the Function (2.3). Nevertheless, corresponding literature references are not known to the author and additional investigations are outside the scope of this thesis since numerical and approximate solutions are straightforward.

For a Hertzian contact and under the assumption of small deformations (where the dimensionless peak radius ρ is independent of the surface height t) the normal load P_z is related to surface elasticity modulus

$$E^* = \frac{E}{2(1 - \nu^2)} \quad (2.4)$$

and the topology parameters for a line contact by

$$4 \frac{P_{zi}}{L} \frac{R_i}{\pi E^*} = a_i^2 \quad (2.5)$$

and for a point contact by

$$\left(\frac{3}{4} \frac{P_{zi}}{L} \frac{R_i}{E^*} \right)^{\frac{2}{3}} = a_i^2 \quad (2.6)$$

respectively. Young's modulus is E and ν denotes the Poisson ratio. Technical details are well documented in the literature [100].

Finally, integration over all contacts gives the load supported by the overall interface

$$P_z(t) = N \int_{\zeta=t}^{\infty} \int_{\rho=0}^{\infty} P_{zi}(\delta_i) f(\zeta, \rho) d\rho d\zeta \quad (2.7)$$

where the asperity deformation $\delta_i = s(\zeta - t)$ is specified by (2.1) and the function $P_{zi}(\delta_i)$ is given by the either of the Relations (2.5) or (2.6). For a line contact

$$P_{zi}(\delta_i) = \frac{1}{4} L \pi E^* \left(2\delta_i - \frac{\ddot{s}\delta_i^2}{\rho_i \sqrt{1.5}} \right) = \frac{1}{4} L \pi E^* \left(2 - \frac{\ddot{s}s(\zeta - t)}{\rho_i \sqrt{1.5}} \right) s(\zeta - t) \quad (2.8)$$

The number of asperities is denoted by N and depends for line contacts on the surface roughness and the width b of the apparent area of contact. The density of peaks has been related [41] to the surface topology parameters by

$$D_L = \frac{1}{2\pi} \frac{\dot{\sigma}}{\dot{\sigma}} \quad (2.9)$$

Therefore, the number of asperities is proportional to the width of the apparent area of contact according to

$$N = D_L b \quad (2.10)$$

Similarly, the area of contact A_{ri} for one asperity is used to find the real area of contact of the interface $A_r(t)$. For example, the real area for a line contact is

$$A_{ri} = 2La_i = 2L\sqrt{\delta_i(R_i - \delta_i)} \stackrel{\delta_i \ll R_i}{\approx} 2L\sqrt{\delta_i R_i} \quad (2.11)$$

It is assumed in (2.11) that asperity deformation does not modify its radius R_i . The real area of contact as a function of dimensionless surface height t results after integration over all asperities

$$A_r(t) = N \int_{\zeta=t}^{\infty} \int_{\rho=0}^{\infty} A_{ri}(\delta_i) f(\zeta, \rho) d\rho d\zeta \quad (2.12)$$

Since no analytic solution for equations of type (2.7) and (2.12) exists, numerical methods are required. It results that the relationship between P_z and A_r is quasi linear for small deformations where the surface height t is large. Furthermore, a brief analysis of (2.7), (2.10) and (2.12) shows that both $P_z(t) \propto A$ and $A_r(t) \propto A$ are proportional to the apparent area of contact A . In addition, it follows that the real area of contact $A_r(P_z)$ as a function of normal load is independent of the apparent area of contact.

In the literature, measurement of electrical conductance is proposed to verify experimentally the dependence of the real area of contact as a function of the normal load. For crossed cylinders as well as for flat surfaces, the electrical conductances Λ are evaluated as a function of normal load P_z [20]. For crossed cylinders, the measured relation is $\Lambda = k_2 \sqrt{P_z}$, which agrees with theoretical results for plastic deformation. The experimental results for a flat, unpolished surface show a linear dependence of the electrical conductance $\Lambda \propto P_z$ at small loads. Unfortunately, the relationship between Λ and the real area of contact A_r of random rough surfaces is not straightforward which reduces the usefulness of this validation approach.

2.2 Interface Properties and Lubrication

Once the real area of contact is evaluated, it is possible to analyze the shearing properties of these contacts. Therefore, it is necessary to observe the behavior of the interface between dry and lubricated surfaces. It has been noticed [5] that the physics of lubrication are not the same at all speeds. This observation is motivated by the experimental investigation of the friction force as a function of velocity for oil lubricated bearings by Stribeck at the beginning of this century [90]. He observed: (i) that the coefficient of friction first decreases for increasing velocities (this is for different applied normal forces); and (ii) that

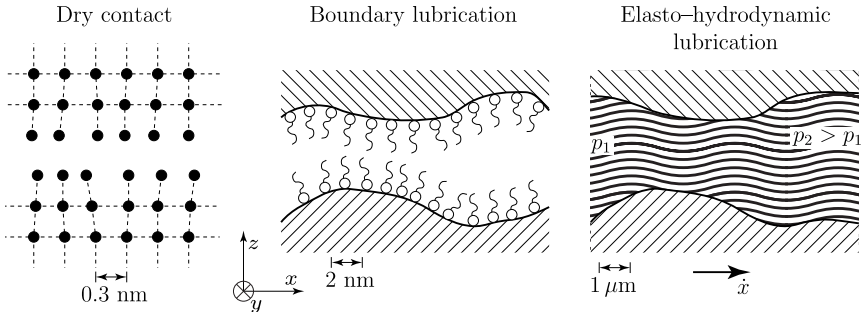


Figure 2.3: Lubrication regimes.

the minimum for the coefficient of friction is obtained for bigger velocities when normal force is increased. Therefore, the velocity–friction force characteristic is often called the Stribeck curve.

For an intuitive explanation and a detailed description of the relationship between the relative velocity and the friction force it is useful to follow the considerations made in the context of robot control [5]. Various regimes of lubrication are distinguished, see Figure 2.3: dry contact, boundary lubrication and elasto-hydrodynamic lubrication. These phenomena are characterized by different scales for the interfacial gap. The atomic lattice constant characterizes a dry contact, the molecular size is a good estimate for the gap size in boundary lubrication, and the surface roughness specifies the geometrical scales for elasto-hydrodynamic lubrication at slow speeds.

2.2.1 Dry Contact

The behavior of dry contacts is described by a molecular theory of friction [92]. Although general solutions are not yet available, particular cases have been studied. The properties of atomically flat iron surfaces, for example, have been predicted [69]. The understanding of the physics of dry contacts are important mainly for the design of micro-mechanisms and space vehicles. The contacting surfaces in micro-mechanisms are often formed of atomically flat silicon. The problems to be solved during design of space vehicles are related to the fact that standard lubricants are rapidly evaporated in a vacuum.

2.2.2 Boundary Lubrication

Boundary lubrication is present when the velocity is insufficient to build a fluid film between the surfaces. Displacement is related to shearing of solid-to-solid contacts. It is often assumed that friction in boundary lubrication is necessarily more important than in fluid lubrication at small velocities [90]. This, however, is not always the case because certain boundary lubricants reduce the break-away force (necessary to initiate macroscopic motion) below the kinetic friction level (the force that opposes steady motion).

Low friction in boundary lubrication is realized by addition of molecules to the lubricant that bind well to the metal surfaces without being corrosive. These molecules need to have sufficient strength to withstand sliding forces without decomposition and yet have low shear strength when moving relative to each other.

With modern lubrication technology it is therefore possible to obtain a monotonic characteristic between velocity and friction force which is favorable to the elimination of the undesirable phenomenon of stick-slip motion. The practical interest of boundary lubricants is illustrated [39] with experimental data comparing the requirements for stable small speed motion of: (i) a dry contact surface, with lubricated interfaces, using (ii) paraffin oil, and (iii) a boundary lubricant. It is concluded that the boundary lubricant produces a smaller negative steady-state velocity-friction force slope compared to paraffin oil.

2.2.3 Elasto-hydrodynamic Lubrication

It has been recognized in the literature that many loaded contacts of low geometrical conformity such as gears, rolling contact bearings and cams frequently behave like they are hydrodynamically lubricated. Operating experience suggested that severe metal-to-metal contact was not taking place, and this led to a theoretical analysis of the lubrication conditions. The theory of elasto-hydrodynamic lubrication takes into account surface elasticity and the viscosity-pressure characteristics [38]. The behavior of the lubricant in the interface is modeled by the Reynolds' equation [81].

These considerations lead to nonlinear relationships for interfacial gap and frictional traction depending on sliding speed and normal load. The corresponding dynamic equations are presented for a journal bearing with hydrodynamic lubrication [50]. A comparison between the resulting simulation data [50] and the experimental observations for a lubricated line contact [51] shows, besides other things, a qualitative agreement of the 'dynamics at small velocities' illustrated in Figure 3.3c.

2.2.4 Mathematical Descriptions

Once experimental data is available for the velocity-friction force characteristics of a given drive, a mathematical description has to be found in order to analyze control stability and tracking performance. An overview of different formulations and references has been presented previously [5]. A unified model for the steady-state characteristics between velocity and friction force is

$$F(\dot{x}) = \sigma_2 \dot{x} + \sigma_0 g(\dot{x}) \operatorname{sign}\dot{x} \quad (2.13)$$

where \dot{x} denotes velocity, σ_2 is the viscous friction coefficient, and $\sigma_0 g(\dot{x})$ describes the nonlinearities of velocity-friction force characteristics. The model is illustrated in Figure 3.1, where \dot{x} is replaced by \dot{q} for consistency of notations in Chapter 3. Table 2.1 contains some mathematical formulations for $\sigma_0 g(\dot{x})$ and the corresponding literature references. The notations are in agreement with those used in Section 3.1.

For a given drive, composed of a large number of interfaces, physical considerations that support one mathematical formulation rather than another are in general very com-

Type	$\text{Nonlinearity } \sigma_0 g(\dot{x})$	References
Linear	F_c	[34]
Piecewise Linear	$F_s - \text{sat}(R \dot{x} , F_s - F_c)$	[86]
Exponential	$F_c + (F_s - F_c) e^{- \dot{x} /v_s}$	[93]
Gaussian	$F_c + (F_s - F_c) e^{-(\dot{x}/v_s)^2}$	[5]
Generalized Exponential	$F_c + (F_s - F_c) e^{-\alpha \dot{x} ^\delta}$	[19], [59]
Laurentzian	$F_c + (F_s - F_c) \frac{1}{1 + (\dot{x}/v_s)^2}$	[51]

Table 2.1: Models describing the relationship between velocity and friction force.

plex. Thus, modeling for control purposes should be based on criteria for matching with experimental data. The parameter identification is based on minimization of some cost function (*e.g.* a weighted quadratic estimation error). The model structure is selected afterwards in order to minimize the specified criterion.

2.3 Longitudinal Loading of Rough Surfaces

When the two primary phenomena, the real area of contact and the interface properties, are analyzed, it is possible to describe the behavior for longitudinal loading. The approach of finding a macroscopic model by integration of the properties for the numerous contact spots remains an efficient method also for the analysis of longitudinal loading. In this section, it is noted first that two particular regimes can be distinguished: (i) the behavior before ‘break-away’, *i.e.* the properties for very small displacements; and (ii) the friction force resulting from large unidirectional motions. Next, modeling of the transition between these two regimes is discussed.

2.3.1 Distributed Element Hysteresis Model

The evaluation of the real area of contact, presented in Section 2.1, is based on the fact that the phenomena related to friction are distributed over numerous contacting asperities. By analogy, it is possible to evaluate the macroscopic behavior of two rough surfaces, pressed against each other and subject to a shearing force. Although an analytic solution of the contact properties could be found, an exact solution is outside the scope of this summary. However, two particular situations can be distinguished: (i) if the mean shearing stress of all asperities equals zero, then the interface behaves like a spring-damper system; and (ii) if all junctions between asperities are broken after a large displacement, then the force transmitted through the macroscopic interface has settled to a constant value.

Below, the relationship is established that exists between the surface model for the two dimensional contact geometry, illustrated in Figures 2.1–2.2, the adhesion theory [12, 100],

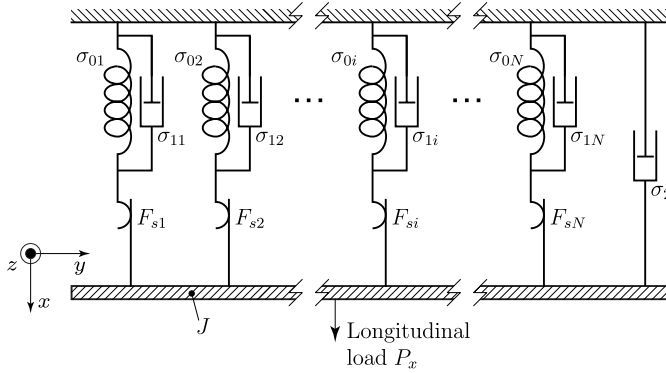


Figure 2.4: Distributed element hysteresis model.

and the model developed for distributed Coulomb friction elements [55].

A schematic view of the configuration considered is shown in Figure 2.4. The key concept is to represent the behavior of a certain number of asperities by summing up the properties of separate (spring, dashpot, slider) elements [57]. In the context considered, see Figures 2.1, 2.2 and 2.5, each element corresponds to a contact region of width $2a_i$. The stiffness, strength and viscous dissipation for each asperity are denoted by σ_{0i} , $F_{si} = A_{ri}\tau_{Bi}$ and σ_{1i} , respectively. For dry and boundary lubricated contacts τ_{Bi} is the shear strength of the interface. The area of a particular contact spot is $A_{ri} = 2a_i L$ for a linear and $A_{ri} = \pi a_i^2$ for a fully isotropic configuration.

This distributed element hysteresis model has the interesting property that global performance in two particular regimes is directly related to physical parameters. For very small displacements, where the mean shearing stress of all asperities is almost zero, all Coulomb sliders are stuck and the system behaves linearly

$$J \ddot{x} + \left(\sigma_2 + \sum_i \sigma_{1i} \right) \dot{x} + \left(\sum_i \sigma_{0i} \right) \tilde{x} = P_x \quad (2.14)$$

where J is the inertia and \tilde{x} denotes deviation from position at rest, *i.e.* $P_x(\tilde{x} = 0) = 0$. This regime (2.14) is called presliding.

The second particular regime describes large x -displacements, where all junctions between asperities are broken. Because motion is assumed to be unidirectional, all Coulomb sliders move after some specific displacement. Since viscous traction for dry contacts or in boundary lubrication is small, *i.e.* $\sigma_2 \dot{x} \ll \sum_i F_{si}$, the tangential force results mainly from the force needed to overcome all F_{si} forces

$$P_x(x \rightarrow \infty) = \sum_i F_{si} \quad (2.15)$$

The literature reference [55], dealing with the distributed element hysteresis model, focused on the evaluation of the transitional effects resulting after a sign-change of the

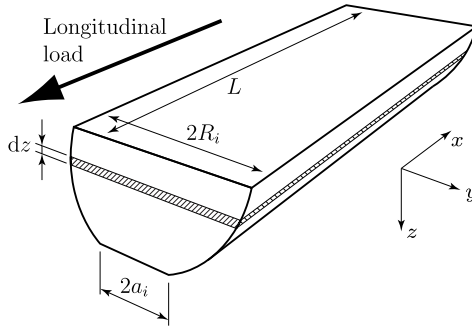


Figure 2.5: Shearing of one asperity.

velocity \dot{x} . The developments are summarized in Section 2.3.5 and a relationship to the Dahl friction model [32] is established. However, below, the two particular regimes (2.14) and (2.15) are of particular relevance for model parameter identification, in Section 3.4, and performance analysis by linearization, in Section 4.2.2.

2.3.2 Stiffness at Rest

First, the parameters describing the presliding regime (2.14) are discussed. Assume that the stiffness at rest $\sigma_0 = \sum_i \sigma_{0i}$ is dominated by the asperity deformation rather than shearing of the interface. It follows that the stiffness at rest should not depend on lubrication, a fact that is confirmed experimentally in Section 6.2.3.

In order to obtain a result for rough surfaces consider, without loss of generality, the simple model of an asperity shown in Figure 2.5 (a flattened half-cylinder of radius R_i and length L). Some basic considerations about mechanics of deformable solids lead to the conclusion that shearing in the direction of the x -axis and the resulting displacement Δx are related to the applied longitudinal load P_x by

$$\Delta x = \frac{P_x}{G} \int_{z=0}^{\sqrt{R_i^2 - a_i^2}} \frac{dz}{A(z)} = \frac{P_x}{G} \int_{z=0}^{\sqrt{R_i^2 - a_i^2}} \frac{dz}{2L\sqrt{R_i^2 - z^2}}$$

and the tangential stiffness for one contact, assuming $a_i \ll R_i$ is

$$\sigma_{0i} = \frac{P_x}{\Delta x} = \frac{2GL}{\int_0^{\sqrt{R_i^2 - a_i^2}} \frac{dz}{\sqrt{R_i^2 - z^2}}} \approx \frac{2GL}{\pi} \quad (2.16)$$

where G is the shear modulus. Therefore, it results that all contacts have the same stiffness, and the total stiffness at rest is

$$\sigma_0 = N \frac{2GL}{\pi} \int_{\zeta=t}^{\infty} \int_{\rho=0}^{\infty} f(\zeta, \rho) d\rho d\zeta \quad (2.17)$$

where the dimensionless surface height t is a function of supported normal load according to (2.7). The number of asperities N is specified by (2.10).

For the contact topology, considered in this section, the numerical solution of Equations (2.7) and (2.17) shows the linear dependence $\sigma_0 \propto P_z$ for small normal loads P_z . Furthermore, the general case of tangential compliance for elastic bodies in contact is discussed in the literature [68]. Therefore, based on these considerations it should be possible to evaluate the stiffness at rest for any surface topology.

2.3.3 Viscous Damping for Presliding

Experimental analysis of dynamics in the presliding regime has shown the importance of the material losses that are modeled by the term $\sum_i \sigma_{1i} \dot{x}_i$ in Equation (2.14). Since material damping depends on the alloy, the mechanical surface finish and the thermal treatment, numerical values are not tabulated in the literature. In addition, the viscous model is only a rough representation of physical reality.

Material damping has been discussed for machine design [52, 88]; and dynamic fracture [11]. Nevertheless, predictions of the parameter σ_1 , based on physical properties, are outside the scope of this thesis. Therefore, the parametric identification, presented in Section 3.4, must be applied.

2.3.4 Break-away force

It is the interfacial shear strength that dominates the break-away force (sometimes also called static friction level); the strength of the asperities plays only a minor role. This has been suggested at least for lubricated contacts where the influence of lubrication on both friction level and wear are analyzed [78].

The influence of pressure on shear strength is the subject of several literature references. For example, a nonlinear characteristic with hysteresis, due to plastic deformation, has been observed for a conformal contact [22]. The shear strength of thin lubricant films has been discussed for a glass sphere on glass plate contact [23]. Unfortunately, these results do not allow predictions such as for the stiffness at rest in a given context.

An alternative approach is based on experimental results. For friction at an atomic scale the experimental data show a linear dependence of friction force with normal load for a Si_3N_4 tip sliding over surfaces of silicon, diamond, and graphite [83]. Based on the idea of molecular attraction and repulsion [92], recent results have been presented for a sharp tip moving over a clean atomically flat surface [47, 87]. These results have been adapted for consideration of the interface of two atomically flat surfaces [69] and a solution of the relations has been proposed for α -iron. Numerical results have been presented for a very limited number of atoms [66], showing even a velocity–force relation that is similar to macroscopically observed velocity–friction force relationship.

Nevertheless, despite all these modeling efforts, no results are known to the author that would allow virtual prototyping of a mechanical system. This could be explained by the difficulty in describing the chemical and physical properties of the surfaces considered. Dominant parameters still need to be specified and tabulated.

Although quantitative prediction of the break-away friction level seems not yet possible, the linear behavior for small loads, that is experimentally observed in Section 6.2.3, is motivated by: (i) the linear dependence $A_r \propto P_z$, and (ii) the assumption that the interfacial shear strength τ_B is a constant for small pressures, *i.e.* $F_{si} = A_{ri}\tau_B$.

2.3.5 Transition from Sticking to Sliding

After analysis of the two particular operating points, very small displacements (evaluation of the stiffness at rest) and unidirectional motion (evaluation of break-away force and the Coulomb level), finally, it remains to find a description for the transition between these two regimes. No really physically motivated approaches are known to the author that would relate a particular transition shape to the material properties and surface topology of the contacting surfaces. Nevertheless, there is a relationship between the model for distributed element hysteresis and the Dahl friction model.

Consider the system illustrated in Figure 2.4 for small unidirectional velocities. Different distribution functions for failure processes have been discussed in the literature [98] that could describe the properties of the Coulomb sliders. Assume that the distribution of the strength of the Coulomb sliders is exponential, *i.e.*

$$\varphi(F_{si}) = \frac{1}{F_s} e^{-F_{si}/F_s} \quad (2.18)$$

This is not necessarily realistic but leads to a simple formulation of friction force as a function of position. In fact, for the initial values $x = 0$ and $P_x = 0$, the tangential load as a function of displacement with $\dot{x} > 0$ is

$$\begin{aligned} P_x(x) &= \underbrace{\int_0^{\sigma_0 x} F \varphi(F) dF}_{\text{yielded sliders}} + \underbrace{\sigma_0 x \int_{\sigma_0 x}^{\infty} \varphi(F) dF}_{\text{stuck sliders}} \\ &= F_s(1 - e^{-\frac{\sigma_0 x}{F_s}}) \end{aligned} \quad (2.19)$$

Similarly, $P_x(x)$ is evaluated for negative velocities. A brief analysis of the expressions shows that this friction model can be expressed in the following differential form

$$\dot{P}_x = \frac{dP_x}{dx} \dot{x} = \sigma_0(\dot{x} - \frac{P_x}{F_s} |\dot{x}|) \quad (2.20)$$

which is valid for positive and negative velocities \dot{x} . Note that the particular exponential shape (2.18) of the distribution $\varphi(F)$ is used in the above developments only to provide simple expressions. In fact, for any particular, but monotonic, shape of the relationship between position and friction force, a corresponding distribution $\varphi(F)$ can be evaluated.

A comparison of (2.20) with the friction model proposed by Dahl in the early seventies [32] shows a perfect match. The fundamental concept of Dahl was that the mathematical model of solid friction, as opposed to fluid friction, consists simply of the observation that the time rate of change of solid friction can be expressed as

$$\frac{dF(x)}{dt} = \frac{dF(x)}{dx} \dot{x} \quad (2.21)$$

where $F(x)$ is the friction force which is a function of displacement x , but which is rate \dot{x} independent. The friction function slope $\frac{dF(x)}{dx}$ is strictly positive at all times and Dahl proposed the relation

$$\frac{dF(x)}{dx} = \sigma_0 \left| 1 - \frac{F}{F_s} \operatorname{sign} \dot{x} \right|^i \operatorname{sign} \left(1 - \frac{F}{F_s} \operatorname{sign} \dot{x} \right) \quad (2.22)$$

in order to represent the experimentally observed phenomena. For convenience, the notations used in (2.22) are adapted to the notations used herein. Later, an example of experimental data for ball bearings has been reported [33]. In addition, it has been noticed already [32] that various transition shapes, modeled by different exponents i , are related to material properties, namely ductile and brittle materials.

Obviously, the Dahl model (2.22) with the exponent $i = 1$ is equivalent to the model (2.20) resulting from the distributed element hysteresis model with the exponential strength distribution function (2.18). Therefore, the relationship is established between tribological studies and integrated friction modeling, based on input–output characteristics. In fact, this observation represents another relevant contribution of this chapter.

2.4 Current Trends in Tribology and Summary

The current trends in tribology that are of particular interest also for the control engineer may be classified into the following categories: handbooks and textbooks, atomic scale phenomena, and transitions (friction as a function of velocity and position).

Handbooks and textbooks. Recently [13, 14, 102], a considerable effort has been made in order to provide a survey of the state of the art in tribology and to give beginners an insight into the basics of tribology. These tutorial texts are very helpful in understanding the physics of friction.

Atomic scale phenomena. Atomic scale phenomena of friction can now be measured [65, 67], which enables validation of theoretical considerations like those for friction without wear [99]. Detailed studies of friction at small normal loads [87] include experimental data. Although at the moment the direct value of this kind of literature is not obvious to the control engineer, the phenomena discussed will perhaps to be included into the modeling of modern micro/nano-systems in the future.

Transitions: friction as a function of velocity and position. Besides fundamental studies, publications are also written on the application of the theory to particular mechanical situations. These article include some predictions for the relationship between velocity and friction force [50], but also the prediction of the relationship between relative position and friction force [31]. These practical studies will be used intensively when the results are included into the virtual prototyping of mechanical systems: the control engineer will be able to influence the mechanical design in order to simplify the synthesis of a suitable controller.

In this chapter, the physical fundamentals of friction have been presented. This is required for the integrated friction modeling in the next chapter. The methodology of averaging the properties for one asperity over the whole surface of contact seems to be a generic approach that could be used for the modeling of other similar processes. However it is noticed that the effort of physical modeling of all phenomena is excessive which motivates the use of mathematical models that represent with ‘sufficient’ quality the input–output properties of the system considered. In the context of control engineering, ‘sufficient’ means relevant for the analysis/synthesis of a control loop that is supposed to achieve specified tracking and regulation performances.

Chapter 3

Integrated Friction Modeling

Objectives

- Considering of two models for friction that are well suited for controller synthesis
- Comparing of these two models in terms of their ability to predict friction force
- Presenting of a methodology for modeling of (complex) drives with friction
- Proposing of a methodology for model parameter identification

THE physics of particular friction phenomena have been discussed in Chapter 2. Whilst this study is sufficient for mechanical design purposes, for example the choice of the materials for a given application, it should be noted that a closed form description is required for the models used by the control engineer. This description should represent a number of phenomena. Therefore, such models, which are well suited for simulation or controller synthesis, are called ‘integrated’ friction models in the sense that they integrate a variety of phenomena in just one formulation.

Therefore, this chapter aims to present a survey of friction modeling for simulation and control purposes and to establish an explicit link between the classical and recent modeling approaches. Furthermore, the problem of model parameter identification, which has been rarely discussed in the literature, is solved. In this context, the reliability of the proposed methodology for identification should be examined thoroughly. However, herein only a rough analysis of the quality and cost for the identification of each model parameter is presented. A detailed discussion is outside the scope of this work which is mainly driven by practical requirements from industry.

Whilst tribology is extensively discussed in undergraduate courses for mechanical engineers, the point of view of the control engineer has only recently been introduced. Numerous topics in control of drives with friction have been discussed systematically [5, 8]. A complete review of friction modeling has been presented recently [9] including a large

number of literature references. From these texts it can be concluded that, basically, friction models can be classified into kinetic friction models (KFM) and dynamic friction models. The KFM describe friction force as a static relation between velocity and applied external forces. They are based on the early experimental observations of Coulomb [34]. Nevertheless, the KFM provide only rough models of reality, where dynamic effects are present. There are a large variety of approaches to including this memory associated with friction phenomena. However, below it is proposed to concentrate discussion on the model recently proposed by a group working at both Lund and Grenoble [27].

This chapter is organized as follows. First two widely used models are presented: the kinetic friction model (KFM) in Section 3.1 and the Lund Grenoble (*LuGre*) model in Section 3.2. Herein, the fundamental properties of each model are discussed. The two models are compared in Section 3.3 with a singular perturbation analysis, investigating their ability to predict the friction force of a simple drive. The results provide indications that help in choosing the adequate model complexity for a given situation. The problem of modeling complex mechanical systems with friction between parts in relative motion still remains. The approach, which is briefly summarized in Appendix A, proposes a rigorous methodology for establishing the differential-algebraic equations even for complex mechanical systems. Finally, a methodology for model parameter identification, which is based on four special experiments that are exciting only particular parts of the system, is presented in Section 3.4.

3.1 Kinetic Friction Model (KFM)

In kinetic friction models (KFM) friction force F during motion is a function of velocity \dot{q} only. Based on an experimental setup, proposed by the French scientist Amontons, extended observations have been reported by de Coulomb [34]. Therein, the behavior of a loaded slide on a flat surface for different constant pulling forces at various speeds was measured. Because, for the setup analyzed, viscous friction was relatively small, it was observed that kinetic friction is almost constant and opposite to the direction of motion. This kinetic friction is called the Coulomb level and is denoted by F_c , see Figure 3.1. Static friction, *i.e.* the friction force that is present when there is apparently no motion of the slide on the plane, compensates applied force up to a certain level, known as the break-away force F_s . The details concerning the relation of friction force as a function of constant velocity have been discussed in Section 2.2 where one of the observations was that F_c is not necessarily equal to F_s .

Firstly, a closed form mathematical description of the KFM is presented below which is a mandatory introduction to all discussion following. After the model properties are illustrated with simulation data showing the phenomenon of stick-slip motion. Finally, the different aspects of simulation of drives with friction are reviewed.

3.1.1 Closed Form Mathematical Description

Although the KFM is used widely, a rigorous formulation of the model, including the behavior at zero velocity, is rarely provided in the numerous publications available currently.

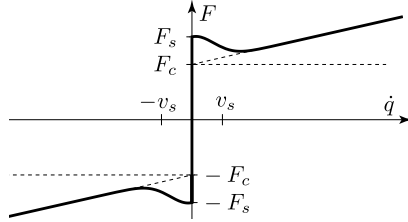


Figure 3.1: Kinetic friction model.

Consider therefore a simple drive, modeled as an inertia J with position q and control input u

$$J\ddot{q} = u - F_{\text{KFM}}(\dot{q}, u) - F_g \quad (3.1)$$

and the following adopted kinetic friction model

$$F_{\text{KFM}}(\dot{q}, u) = \sigma_2 \dot{q} + \sigma_0 g(\dot{q}) \operatorname{sign}\dot{q} + (1 - |\operatorname{sign}\dot{q}|) \operatorname{sat}(u - F_g, F_s) \quad (3.2)$$

where

$$\operatorname{sat}(x, M) = \begin{cases} M & , \forall x > M \\ x & , \text{if } -M \leq x \leq M \\ -M & , \forall x < -M \end{cases} \quad (3.3)$$

$$\operatorname{sign}\dot{q} = \begin{cases} +1 & , \forall \dot{q} > 0 \\ 0 & , \text{if } \dot{q} = 0 \\ -1 & , \forall \dot{q} < 0 \end{cases} \quad (3.4)$$

$$\sigma_0 g(\dot{q}) = F_s e^{-\dot{q}^2/v_s^2} + F_c (1 - e^{-\dot{q}^2/v_s^2}) \quad (3.5)$$

The behavior at zero velocity is described by the third term to the right-hand side of (3.2) which is motivated by the approach of modeling variable structure systems [40]. The meaning of the sign-function is switching between the three different models at negative, zero and positive velocity. The concept is that friction force F is a function of velocity \dot{q} and applied force u .

Equation (3.5) is one of the parametric models, listed in Table 2.1, for the nonlinear relationship between velocity and friction force. Although this model represents observed behavior, no literature references have been found that would relate this particular (Gaussian) shape to the physical phenomena of boundary and elastohydrodynamic lubrication. Viscous friction at high speed is denoted by $\sigma_2 \dot{q}$. The influence of gravity or amplifier offsets on the control variable is F_g , the characteristic velocity of Stribeck's curve, is denoted by v_s .

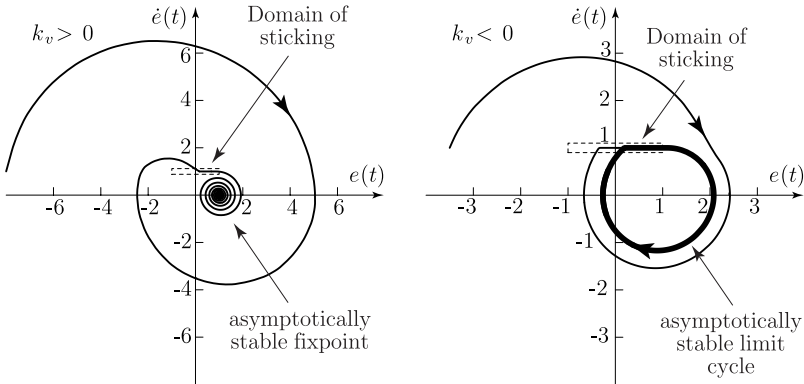


Figure 3.2: Properties of kinetic friction model.

3.1.2 Model Properties

An effective way to illustrate the properties of the KFM is to demonstrate its ability to predict stick-slip motion. This phenomenon is a succession of periods of time, where the system is apparently at rest (sticking), followed by intervals of motion (slipping). For a brief overview of the properties of the KFM in general and of the stick-slip motion phenomenon in particular, consider a simple drive with Coulomb friction only, *i.e.* $F_s = F_c$ and $\sigma_2 = 0$, modeled by

$$\ddot{e} = -e - k_v \dot{e} + F_{\text{KFM}}(1 - \dot{e}, e + k_v \dot{e}) \quad (3.6)$$

with $e = t - q$. Time is denoted by t and the friction force $F_{\text{KFM}}(\dot{q}, u)$ is specified by (3.2). The definition of the position tracking error $e = t - q$ corresponds to a constant velocity reference, and the choice of the PD position controller $u = e + k_v \dot{e}$ corresponds to common practice. The present situation is comparable to the one previously considered [76] for the study as to whether a periodic or a chaotic behavior results for the system states from a periodic excitation signal.

The phase plane of certain trajectories, resulting from convenient parameters and initial conditions, is shown in Figure 3.2. The domain of sticking is indicated explicitly, *i.e.* the line segment in the phase plane where the system, for a period of time, is apparently at rest ($\dot{q} = 0$) and the control action is insufficient to initiate motion ($\ddot{q} = 0$). Inside this region, the sat-function in the friction model (3.2) just compensates for the applied control action; whilst outside the dotted area, control action is larger than the break-away friction F_s . The two plots illustrate the behavior for the following situations: (i) in the case of negative velocity feedback where $k_v > 0$ it is obvious that the fixed point $(1, 0)$ of the system is reached asymptotically, and (ii) if positive velocity feedback is applied ($k_v < 0$) then an asymptotically stable limit cycle is reached.

A rigorous stability analysis [7] is outside the scope of this section. Nevertheless, certain essentials should be pointed out: The state of the system, namely $x(t) = [e(t) \dot{e}(t)]^T$,

$\forall t > t_0$, exists and is uniquely defined for any initial condition $x(t = t_0)$. In addition, $x(t)$ is a continuous function of time. These mathematical topics of uniqueness and continuity have been discussed more rigorously [84] and a proof of the above statements has been presented based on the theory of differential inclusions [10].

The time derivative of the state \dot{x} for a transition from sticking to sliding is a continuous function of the time as long as the controller $u(x, t)$ is a continuous function of both the state and time. However, it is obvious that the transitions from motion to sticking are generally coupled with a discontinuity of the acceleration \ddot{q} . These two facts are very important for the modeling of drives with flexible transmission elements where discontinuous accelerations excite high frequency modes which would be negligible if all states would evolve in a continuous manner.

The situation illustrated on the right-hand side in Figure 3.2 can also occur in the general case if $F_s > F_c$; all other parameters k_v , k_p , etc. are assumed to be positive. The problem of stick-slip motion, which is related to the appearance of the asymptotically stable limit cycle, needs to be checked in detail as soon as $(\sigma_2 + k_v + \sigma_0 \frac{dg(\dot{q})}{d\dot{q}}) < 0$ within a velocity interval around zero.

3.1.3 Simulation Aspects

A discussion of simulation aspects of drives with friction has been presented for several model formulations [48]. In fact, a correct numerical solution of the initial value problem is very difficult, and precision is often low at velocity reversals due to the discontinuities of the KFM. Different solutions can be found in the literature: (i) if friction force is assumed to be zero at rest, i.e. the last term in (3.2) is not considered, a description results which is far from reality; (ii) if the sign-function is replaced by a saturated high gain acceleration is possible already for small forces, which does not correspond to reality either; and (iii) the most accurate simulation approach is the Karnopp model [58] that adapts the zero velocity region of (3.2)–(3.4) for computer implementation

$$\text{sign}\dot{q} = \begin{cases} +1 & , \forall \dot{q} > m \\ 0 & , \text{if } \dot{q} \in [-m, m] \\ -1 & , \forall \dot{q} < -m \end{cases} \quad (3.7)$$

where m is a small number, depending on the computing precision. The improvement in the quality of computer simulation, achieved with the introduction of the dead zone (3.7), results from a better detection of the periods of sticking by the numerical differential equation solver.

3.2 Lund–Grenoble (*LuGre*) Model

The essential elements of the concepts presented in Chapter 2 are integrated in the friction model that has been developed by researchers working at both Lund and Grenoble [27]. Whereas, herein it is one of the aims to establish a link between tribology and modeling for control. The contributors to the *LuGre* model have indicated that they aimed simply

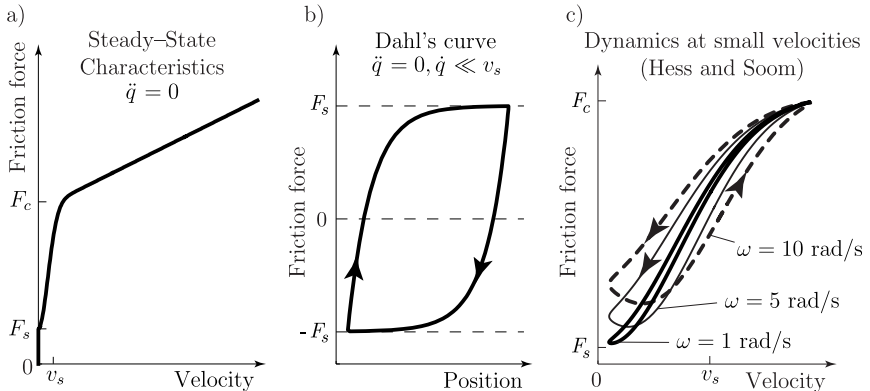


Figure 3.3: Input–output phenomena, captured by the *LuGre* model.

to represent the input–output phenomena illustrated in Figure 3.3 and described in the literature. The main elements are the following:

- (i) An intuitive explanation of the friction phenomena is the bristle model [48]. The physical paradigm underlying this model is a pair of facing surfaces with bristles extending from each. The bristles on one surface are bonded with opposing bristles from the other surface. The friction force contributed by each bristle is assumed to be proportional to the strain on the bristle. When the strain on any particular bristle exceeds a certain level then the bond is broken.
- (ii) It has been observed experimentally [30, 89] that friction force is not only related to relative velocity but is also a function of position. A typical position–friction force hysteresis loop is shown in Figure 3.3b. This position dependence can be described by the hysteresis model proposed by Dahl [32]. Later, Dahl’s model has been subject to a thorough mathematical analysis [16].
- (iii) Certain time dependent phenomena for unidirectional motion have been discussed previously [82]. The postulation is that a fading memory effect is appended to the instantaneous influence of time varying relative velocities. The corresponding phenomena have been observed experimentally [51] for triangular velocity profiles.
- (iv) In order to increase the simulation performance achieved with the ‘reset integrator model’, it has been proposed [48] to add some viscous friction, that is active for small displacements only. This particular viscous term has not only been added for convenience of simulation, but also to include physical realism: the oscillations occurring after entering into a ‘sticking’ mode vanish owing to energy dissipation into the surrounding material.

Firstly, this section presents a brief description of the *LuGre* model. The main model properties are analyzed in a second step. Simulation of the *LuGre* model is in general straightforward. Nevertheless, it is observed that certain phenomena that are not captured by the *LuGre* model remain.

3.2.1 Brief Description

Consider the dynamic model [27] for a simple drive with friction, describing a rotational inertia J with angular coordinate q and control input u

$$J\ddot{q} = u - F_{LuGre}(\dot{q}, z) - F_g \quad (3.8)$$

$$F_{LuGre}(\dot{q}, z) = \underbrace{\sigma_0 z + \sigma_1 \left(\dot{q} - \frac{|\dot{q}|}{g(\dot{q})} z \right)}_{\sigma_1 \dot{z}} + \sigma_2 \dot{q} \quad (3.9)$$

$$\dot{z} = \dot{q} - \frac{|\dot{q}|}{g(\dot{q})} z \quad (3.10)$$

where $g(\dot{q})$ is specified by the Gaussian model (3.5). The friction interface between two surfaces is considered as a contact between bristles, and the variable z denotes an additionally introduced state that models the average deflection of these bristles. The bending of the bristles generates the friction force $\sigma_0 z + \sigma_1 \dot{z}$ where σ_0 and σ_1 represent material stiffness and damping coefficients.

Note that the analogy between the contact of bristles and the junctions formed between some asperities of two rough surfaces is only used for a better understanding of the friction phenomena. In addition, it is emphasized that the two extensions with respect to Dahl's model [32] are the following: (i) the introduction of the nonlinear relation $\sigma_0 g(\dot{q})$ between steady-state velocity and friction force, and (ii) the modeling of viscous damping at small displacements by the term $\sigma_1 \dot{z}$.

3.2.2 Model Properties

The first property of the *LuGre* model that is checked is the existence of a solution to the initial value problem. For this, it is convenient to reformulate the model (3.5), (3.8)–(3.10) for a simple drive in a state space form

$$\dot{x} = \underbrace{\begin{bmatrix} \dot{q} \\ \frac{1}{J} \left(-\sigma_0 z - \sigma_1 \left(\dot{q} - \frac{|\dot{q}|}{g(\dot{q})} z \right) - \sigma_2 \dot{q} - F_g \right) \\ \dot{q} - \frac{|\dot{q}|}{g(\dot{q})} z \end{bmatrix}}_{= f(x)} + \underbrace{\begin{bmatrix} 0 \\ \frac{u(x, t)}{J} \\ 0 \end{bmatrix}}_{= \gamma(x, t)} \quad (3.11)$$

where the state of the system is denoted by $x = \begin{bmatrix} q & \dot{q} & z \end{bmatrix}^T$.

Fact 3.1 Assume control action $u(x, t)$ is bounded and continuous in the state x and the time t , then at least one continuous solution $x(t) \in \mathcal{C}^1(t), t \in [t_0, t_1]$ exists that solves the initial value problem for the system (3.11) with initial state $x(t_0) = x_0$.

Proof. The right-hand side of (3.11) is continuous and bounded. The postulate results from the existence theory for nonlinear ordinary differential equations (ODE), summarized recently [71]. Although $t_1 > t_0$, control actions $u(x, t)$ exist such that certain states escape to infinity in finite time t_{crit} . In this situation $t_1 < t_{\text{crit}}$. ■

Owing to Fact 3.1, standard ODE-solvers can be used to find a solution $x(t)$ verifying (3.11) and the initial condition $x(t_0) = x_0$. Nevertheless, note that dynamic step size Runge–Kutta algorithms are very slow when the velocity \dot{q} is large due to the model's stiffness. This property is used in Section 3.3 for model order reduction with a singular perturbation approach.

Whilst proof of the existence of a solution to the initial value problem is trivial, it seems to be cumbersome to show also the uniqueness of this solution. In fact, the model cannot be linearized around zero velocity $\dot{q} = 0$, and furthermore the Lipschitz condition

$$\|f(x_2) + \gamma(x_2, t) - f(x_1) - \gamma(x_1, t)\| \leq L \|x_2 - x_1\| \quad (3.12)$$

is not verified globally. The Lipschitz constant L is in fact dependent on the domain of velocities considered and increases for large velocities. Therefore, it is hard to prove uniqueness of $x(t)$ globally. Nevertheless, the system (3.11) conforms [24] with Lipschitz locally (if $u(x, t)$ is Lipschitz) and therefore, the uniqueness of $x(t)$ is guaranteed locally, which is sufficient for the purpose of the analysis presented below.

A second fact required for the synthesis of standard and advanced control of drives with friction, discussed in the following chapters, is the property that the friction state is bounded.

Fact 3.2 The set $\bar{\mathcal{L}} = \{z : |z| \leq \sup g(\cdot)\}$ is an invariant set of the friction state z .

Proof. see [27] ■

Furthermore, note that the initial friction state satisfies $z(t_0) \in \bar{\mathcal{L}}$ because when two sliding surfaces touch, the junction deformation is zero, i.e. $z(t_{\text{touch}}) = 0$.

Additional elements for controller synthesis are related to statements on passivity of maps between signals. The objective is to apply a modular design to a group of interacting elements with the subsystems presenting all adequate properties. The corresponding theory for interconnection of subsystems that are all dissipating energy [35, 103] enables the analysis of the global properties even for very large systems.

Fact 3.3 The mapping $\dot{q} \mapsto z$ is passive.

Proof. see [27] ■

Furthermore, this property of passivity is employed [27] for the synthesis of a nonlinear controller consisting of an acceleration feedforward, a PD error control and a friction

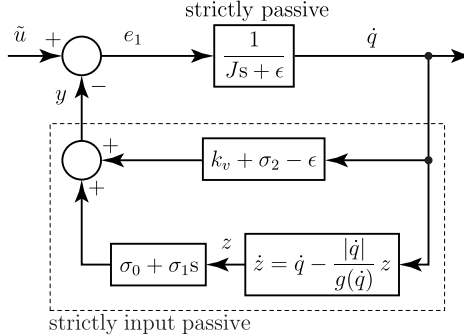


Figure 3.4: System passivity.

observer based input–output linearization. Therein, it is shown for the nominal parameter case that the friction estimation error, as well as the position error, decay asymptotically towards zero for any twice differentiable reference trajectory. The drawbacks of this approach are the two limitations: (i) velocity measurement is assumed, and (ii) the proof is valid only for the nominal parameter case. In addition, stability with integral action in the error controller is not shown.

Intuitively, friction is an energy dissipating phenomenon. Therefore, it is expected that the map $\tilde{u} \mapsto \dot{q}$ from applied force to velocity is passive; this is of course only possible after removing the offset F_g from the control variable by $\tilde{u} = u - F_g$. Unfortunately, the *LuGre* model does not accord with this intuitive reasoning: the problem arises from the $\sigma_1 \dot{z}$ term that was originally added in order to increase damping for small displacements. Therefore, in order to be passive, a drive with friction has to verify a minimal viscous gain condition.

Fact 3.4 Any ‘finite energy’ force input $\tilde{u} \in \mathcal{L}_2$ results in a ‘finite energy’ velocity output $\dot{q} \in \mathcal{L}_2$, if

$$\sigma_2 + k_v > \sigma_1 \frac{\sup g(\cdot) - \inf g(\cdot)}{\inf g(\cdot)} + \epsilon \quad (3.13)$$

where $\epsilon > 0$.

Proof. Consider the block diagram shown in Figure 3.4. Because the map $e_1 \mapsto \dot{q}$ is strictly passive, the postulation results from the passivity theorem [35] in the case that the map $\dot{q} \mapsto y$ is passive. This is shown by considering the storage function $S_2 = \frac{1}{2}\sigma_0 z^2$. Its time derivative is

$$\dot{S}_2 = \sigma_0 z \left(\dot{q} - \frac{|\dot{q}|}{g(\dot{q})} z \right)$$

The mapping $\dot{q} \mapsto y$ is passive if $\dot{S}_2 \leq \dot{q}y$. In fact, the supply rate $\dot{q}y$ is

$$\dot{q}y = \left((k_v + \sigma_2 - \epsilon) \dot{q}^2 - \sigma_1 \frac{|\dot{q}|}{g(\dot{q})} z \dot{q} + \sigma_1 \dot{q}^2 \right) + \sigma_0 \dot{q}z$$

where it is emphasized that the term

$$-\sigma_1 \frac{|\dot{q}|}{g(\dot{q})} z \dot{q} + \sigma_1 \dot{q}^2 = \sigma_1 \left(1 - \frac{z}{g(\dot{q})} \operatorname{sign} \dot{q} \right) \dot{q}^2$$

is problematic because it is negative during periods of time where $|z| > g(\dot{q})$ and $\operatorname{sign} z = \operatorname{sign} \dot{q}$. The solution for obtaining at least a passive mapping $\dot{q} \mapsto y$ is to require a ‘sufficiently’ large viscous damping $\sigma_2 + k_v$ in the condition (3.13) of Fact 3.4. Finally, the passivity theorem proves the postulation since

$$\begin{aligned} \dot{S}_2 &= \dot{q}y - (k_v + \sigma_2 + \sigma_1 - \epsilon) \dot{q}^2 + \sigma_1 \frac{|\dot{q}|}{g(\dot{q})} z \dot{q} - \sigma_0 \frac{|\dot{q}|}{g(\dot{q})} z^2 \\ &\stackrel{\text{Fact 3.2}}{\leq} \dot{q}y - \left(k_v + \sigma_2 - \epsilon - \sigma_1 \frac{\sup g(\cdot) - \inf g(\cdot)}{\inf g(\cdot)} \right) \dot{q}^2 - \sigma_0 \frac{|\dot{q}|}{g(\dot{q})} z^2 \\ &\leq \dot{q}y \end{aligned} \quad \blacksquare$$

For the case where estimated velocity $\hat{v}(t) = \frac{1}{T_f}(q - \int_{t_0}^t \hat{v}(\tau) d\tau)$ is used for feedback, it must be emphasized that it is not possible to use the approach of Fact 3.4 to prove that the velocity signal is $\dot{q} \in \mathcal{L}_2$. This is because the transfer function of the linear part of the system becomes

$$\frac{T_f s + 1}{J T_f s^2 + (J - \epsilon T_f)s + (k_v - \epsilon)}$$

which is not SPR for any $\epsilon > 0$.

Fact 3.5 *The mapping $\tilde{u} \mapsto \dot{q}$ with feedback of measured velocity according to $\tilde{u} = u - F_g + k_v \dot{q}$ is strictly output passive if*

$$\sigma_2 + k_v > \sigma_1 \frac{\sup g(\cdot) - \inf g(\cdot)}{\inf g(\cdot)} \quad (3.14)$$

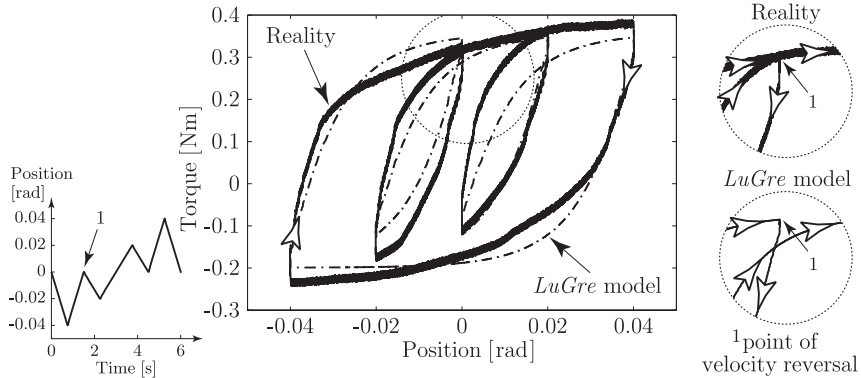
Proof. When the considerations of the proof of Fact 3.4 are combined

$$\begin{aligned} \tilde{u} \dot{q} &= (e_1 + y) \dot{q} \\ \tilde{u} \dot{q} &\geq \dot{q} (J \ddot{q} + \epsilon \dot{q}) + \sigma_0 z \left(\dot{q} + \frac{|\dot{q}|}{g(\dot{q})} z \right) + \left(k_v + \sigma_2 - \epsilon - \sigma_1 \frac{\sup g(\cdot) - \inf g(\cdot)}{\inf g(\cdot)} \right) \dot{q}^2 \\ \tilde{u} \dot{q} &\geq \underbrace{J \dot{q} \ddot{q} + \sigma_0 z \left(\dot{q} + \frac{|\dot{q}|}{g(\dot{q})} z \right)}_{= S_1} + \underbrace{\left(k_v + \sigma_2 - \sigma_1 \frac{\sup g(\cdot) - \inf g(\cdot)}{\inf g(\cdot)} \right) \dot{q}^2}_{=: \alpha} \end{aligned}$$

where $S_1 = \frac{1}{2} J \dot{q}^2 > 0$ and $S_2 = \frac{1}{2} \sigma_0 z^2 > 0$. Therefore

$$\langle \tilde{u} | \dot{q} \rangle_T \geq \alpha \| \dot{q} \|_T^2$$

with $\alpha > 0$ if the condition (3.14) holds. \blacksquare

Figure 3.5: Limitations of the *LuGre* model.

3.2.3 Limitations

Although almost all phenomena observed for drives with friction are reproduced by the *LuGre* friction model, there exists, however, a minor difference for small displacements between the actual friction force and the predicted friction force. The phenomenon is illustrated in Figure 3.5 by a comparison of experimental data from a vertical electro-discharge machining axis and simulation data resulting from a convenient choice of the model parameters. This phenomenon has already been reported in the late seventies [72]. However, the experimental technology and alternative approaches to modeling are still the subject of research [54]. The observation is that every point of velocity reversal will be recovered in the parametric position–friction force plot, once the force resumes the corresponding value (no matter how many reversals happen previously). This phenomenon is called the reversal point memory and can be modeled, by the Preisach model for hysteresis [97] for example. The simulation data shown in Figure 3.5 for the *LuGre* model clearly illustrates the fact that the *LuGre* model is not able to predict the reversal point memory that is observed experimentally.

The modeling of this special type of frictional memory has been addressed in parallel by two research groups [42, 53]. The resulting models represent well the observed phenomena, but owing to their implementation of the reversal point memory there is only a small chance of doing conventional nonlinear controller synthesis like that presented for the *LuGre* model in the following chapters.

3.3 Comparison of the Two Friction Models

Clearly, the two friction models introduced in Sections 3.1–3.2 differ in complexity. For the synthesis of a controller satisfying the specifications of a given application, a model is required that represents dominant phenomena, but is not too complex. A singular

perturbation approach is applied in this section in order to compare the two friction models: an explicit separation of dynamics is presented in a first step in order to analyze in the following step the ability to predict friction force for some particular velocity profiles, namely unidirectional motion and velocity reversals at constant acceleration.

3.3.1 Small Parameter: Characteristic Space Constant

In order to transform the *LuGre* model (3.5), (3.8)–(3.10) into a standard singular perturbation form, set

$$x_s = \frac{F_s}{\sigma_0} = \epsilon \bar{x}_s = O(\epsilon) \quad (3.15)$$

where $\bar{x}_s = O(1)$. Note that the dimension of x_s is a displacement. The parameter x_s is called the characteristic space constant/displacement of the drive [4] and it is shown that x_s is constant even for varying normal forces N (unlike F_s , F_c and σ_0 which are nearly proportional to N , see Section 6.2.3). For simplicity, assume below that $O(F_s) = O(F_c)$, which is motivated by practice because this should be one of the major specifications for lubricant selection. Furthermore, set

$$\zeta = \frac{z}{\epsilon} \quad (3.16)$$

$$\bar{g}(\dot{q}) = \frac{g(\dot{q})}{\epsilon} \quad (3.17)$$

which transforms the model (3.8)–(3.10) for a simple drive into

$$J\ddot{q} = u - \left(\sigma_0 \epsilon \zeta + \sigma_1 \dot{q} - \sigma_1 \frac{|\dot{q}|}{\bar{g}(\dot{q})} \zeta + \sigma_2 \dot{q} \right) - F_g \quad (3.18)$$

$$\epsilon \dot{\zeta} = \dot{q} - \frac{|\dot{q}|}{\bar{g}(\dot{q})} \zeta \quad (3.19)$$

The reduced order model for this system is given for $\epsilon = 0$. Relation (3.19) reduces to an algebraic equation that is solved for ζ . For zero velocity the variable $\bar{\zeta}$ of the reduced order system could theoretically take any value, but since the objective here is to establish a relationship to the reduced order KFM (3.1)–(3.5), set

$$\bar{\zeta} = \begin{cases} \bar{g}(\dot{q}) \operatorname{sign}\dot{q} & , \forall \dot{q} \neq 0 \\ \operatorname{sat}\left(\frac{u - F_g}{\bar{\sigma}_0}, \bar{g}(0)\right) & , \dot{q} = 0 \end{cases} \quad (3.20)$$

3.3.2 Explicit Separation of Dynamics

Denoting the deviation from the unperturbed model by $\eta = \zeta - \bar{\zeta}$ and introducing the KFM (3.2) into Equation (3.18) leads after algebraic manipulations to

$$J\ddot{q} = u - \left(F_{\text{KFM}} - \left(\epsilon \eta \left(\sigma_1 \frac{|\dot{q}|}{\bar{g}(\dot{q})} - \sigma_0 \right) + \underbrace{\sigma_1 \frac{|\dot{q}|}{\bar{g}(\dot{q})} (1 - |\operatorname{sign}\dot{q}|) \operatorname{sat}(u - F_g, F_s)}_{= 0, \forall \dot{q}} \right) \right) - F_g \quad (3.21)$$

Because the last term of (3.21) is always zero, the reduced order dynamics $J\ddot{q} = u - F_{\text{KFM}} - F_g$ are only subject to the perturbation $\epsilon\eta\left(\sigma_1\frac{|\dot{q}|}{g(\dot{q})} - \sigma_0\right)$. The perturbation dynamics can be deduced from $\eta = \zeta - \bar{\zeta}$, (3.19) and (3.20), leading to

$$\dot{\zeta} = -\frac{|\dot{q}|}{g(\dot{q})}\eta$$

where it should be noted that it is not possible to write the perturbation dynamics with the variable η only because $\dot{\eta}$ is not defined for zero velocity $\dot{q} = 0$.

Now it is possible to express the model with a clear separation of the reduced order model and its perturbation p

$$J\ddot{q} = u - (F_{\text{KFM}} - p) - F_g \quad (3.22)$$

$$p = \epsilon(\zeta - \bar{\zeta})\left(\sigma_1\frac{|\dot{q}|}{g(\dot{q})} - \sigma_0\right) \quad (3.23)$$

$$\begin{aligned} \epsilon\dot{\zeta} &= \underbrace{-\frac{|\dot{q}|}{\bar{g}(\dot{q})}}_{\leq 0}(\zeta - \bar{\zeta}) \\ &\leq 0 \end{aligned} \quad (3.24)$$

From Equations (3.22)–(3.24) it follows that the KFM is a reduced order form of the *LuGre* model, while p plays the role of the ‘difference’ between the *LuGre* model and the KFM. Unfortunately, a relationship between these two models using Tikhonov’s theorem [60] is not possible because: (i) the *LuGre* model is not differentiable; (ii) the solution $\bar{\zeta}$ (3.20) to the algebraic equation when setting $\epsilon = 0$ in (3.24) is discontinuous, and (iii) the fast subsystem (3.24) in the *LuGre* model is not exponentially stable, uniformly in \dot{q} and for all \dot{q} .

3.3.3 Friction Force Prediction: Unidirectional Motion

Here, the two friction models KFM and *LuGre* are compared with a detailed discussion of the ‘fast’ subsystem (3.23)–(3.24). Therefore, the two models are analyzed for their difference p in predicted friction force resulting from a given (differentiable) velocity signal \dot{q} , *i.e.* consider the map $\dot{q} \mapsto p$. Because in general, standard Tikhonov’s theorem cannot be used to relate the *LuGre* model to the KFM, only discussion of particular cases is provided here, which has proved to be useful in comparing between the two models.

Tikhonov’s theorem can sometimes be applied locally in the regime of nonzero velocities without velocity reversals. Assume $t \in [t_0, T]$ and: (i) motion is unidirectional, *i.e.* $\text{sign}\dot{q}(t) \equiv \text{constant}$; (ii) velocity is bounded, *i.e.* $\exists v_{\max} = \max |\dot{q}(t)| < \infty$; and (iii) velocity is never zero, *i.e.* $\exists v_{\min} = \min |\dot{q}(t)| > 0$. Under these assumptions, the ‘fast’ subsystem (3.23)–(3.24) can be expressed in a proper singular perturbation format

$$p = \epsilon\eta\left(\sigma_1\frac{|\dot{q}|}{g(\dot{q})} - \sigma_0\right) \quad (3.25)$$

$$\begin{aligned} \epsilon\dot{\eta} &= -\frac{|\dot{q}|}{\bar{g}(\dot{q})}\eta - \epsilon\frac{d\bar{g}}{d\dot{q}}\ddot{q} \\ &\leq 0 \end{aligned} \quad (3.26)$$

Furthermore, analyze the Lyapunov function candidate

$$V = \frac{1}{2} \eta^2 \quad (3.27)$$

and its derivative through the solution of the system (3.25)–(3.26) which is

$$\dot{V} = -\frac{|\dot{q}|}{\epsilon \bar{g}(\dot{q})} \eta^2 - \eta \frac{d\bar{g}}{d\dot{q}} \dot{q} \quad (3.28)$$

There are two different cases: (i) the perturbation p decays exponentially to zero if the second term $-\eta \frac{d\bar{g}}{d\dot{q}} \dot{q}$ in (3.28) is zero, and (ii) the perturbation p approaches asymptotically some boundary layer if the term $\frac{d\bar{g}}{d\dot{q}} \dot{q}$ is bounded, *i.e.*

$$M = \max \left| \frac{d\bar{g}}{d\dot{q}} \dot{q} \right| < \infty \quad (3.29)$$

Exponential stability is achieved if $F_c = F_s$ *i.e.* $\frac{d\bar{g}}{d\dot{q}} = 0$, or if $\dot{q} = 0$, *i.e.* at constant velocity \dot{q} . The derivative of the Lyapunov function satisfies under these conditions

$$\dot{V} \leq -\alpha \eta^2 \quad (3.30)$$

with

$$\alpha = \min \frac{|\dot{q}|}{\epsilon \bar{g}(\dot{q})} = \frac{v_{\min}}{x_s \max \left\{ 1, \frac{F_c}{F_s} \right\}} \quad (3.31)$$

therefore

$$|\eta(t)| \leq |\eta_0| e^{-\alpha t} \quad (3.32)$$

the triangular inequality $|a + b| \leq |a| + |b|$ in combination with (3.25) and (3.32) leads to

$$|p| \leq \epsilon \left(\sigma_0 + \sigma_1 \frac{v_{\max}}{x_s \min \left\{ 1, \frac{F_c}{F_s} \right\}} \right) |\eta_0| e^{-\alpha t} \quad (3.33)$$

In other words, the perturbation p decays exponentially with a time constant $T_p = \frac{1}{\alpha}$ that depends on the smallest velocity v_{\min} and the characteristic space constant x_s . Owing to the fact that x_s is $O(\epsilon)$ it also follows that T_p is $O(\epsilon)$. It should be emphasized that the speed of convergence of the predicted friction force by the KFM towards the prediction of the *LuGre* model is strongly related to the characteristic space constant x_s according to (3.31). Note that here Tikhonov's theorem applies locally because the ‘fast’ subsystem (3.25)–(3.26) is exponentially stable.

An asymptotically stable boundary layer is reached in the general case where $F_c \neq F_s$ and $\dot{q} \neq 0$. The perturbation p decays asymptotically towards the boundary layer specified by

$$\lim_{t \rightarrow \infty} |p(t)| \leq \epsilon^2 \left(\sigma_0 + \sigma_1 \frac{v_{\max}}{x_s \min \left\{ 1, \frac{F_c}{F_s} \right\}} \right) \frac{M \max \bar{g}(\dot{q})}{v_{\min}} \quad (3.34)$$

because

$$\dot{V} < 0 \quad \forall |\eta| > \frac{M}{v_{\min}} \epsilon \max \bar{g}(\dot{q}) \quad (3.35)$$

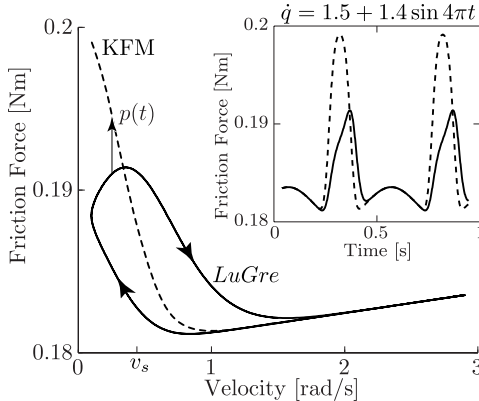


Figure 3.6: Dynamic friction force lags KFM (simulation data).

Discussion. The second term in (3.26), *i.e.* $-\epsilon \frac{d\dot{q}}{d\dot{q}} \dot{q}$ is related to the dynamics observed experimentally [51], and illustrated in Figure 3.6 with simulation data. The observed phenomenon is a dynamic loop that friction force exhibits at ‘slow’ velocities: the fact that the friction force lags the time varying velocity signal is a property that is not accounted for by the KFM (dashed line). The *LuGre* friction model was designed in order to represent the experimentally observed dynamic properties. The simulation results [27] show only the qualitative behavior of the model. The singular perturbation analysis from this section, however, explains the mechanism responsible for the hysteresis behavior. The difference between the KFM and the *LuGre* model that is expressed in Equation (3.22) by the perturbation p , is large for small velocities where $\frac{d\dot{q}}{d\dot{q}}$ is large, *i.e.* around the characteristic velocity v_s of the velocity–friction force relationship. In addition, from (3.34) the magnitude of p increases with increasing accelerations, *i.e.* increasing frequencies of the velocity signal \dot{q} . This fact is in accordance with the experimental observations [51] and with the simulation results [27].

For $\dot{q} \gg v_s$, the value of $\frac{d\dot{q}}{d\dot{q}}$ is very small. The value of M is therefore small which implies a small boundary layer. The KFM might therefore be an adequate representation of reality for applications where velocity is always high. For the situation illustrated in Figure 3.6, this is the case during periods where the velocity $\dot{q} > 2 \frac{\text{rad}}{\text{s}}$. Here the *LuGre* and the KFM predict approximately the same friction force. Nevertheless, it should be emphasized that asymptotic stability of p cannot be shown.

3.3.4 Friction Force Prediction: Zero velocity transition at constant acceleration

Zero velocity transitions are encountered in a large number of applications, since the operating range of a given setup is generally bounded and sooner or later, the initial

position will be recovered. In addition, performances show already that zero velocity transitions are related to very difficult problems for analysis and controller synthesis owing to the highly nonlinear system behavior. Therefore, consider for simplicity a transition through zero velocity at $t = 0$ with constant acceleration a , since a general analysis has proved to be quite cumbersome. Thus the velocity is

$$\dot{q} = at, \forall t \geq 0 \quad (3.36)$$

In practice, this behavior can be achieved by an appropriate control. In addition assume that $F_s = F_c$, and the fast dynamics (3.24) reduce to

$$\epsilon \dot{\zeta} = -\frac{a t \epsilon \sigma_0}{F_s} (\zeta - \bar{\zeta}) \quad (3.37)$$

where $\bar{\zeta} = \frac{F_s}{\epsilon \sigma_0} \text{sign}\dot{q}$. Without loss of generality assume that $\bar{\zeta} = \frac{F_s}{\epsilon \sigma_0}, \forall t > 0$. The general solution for (3.37) is

$$\zeta(t) = \frac{F_s}{\epsilon \sigma_0} + C e^{-\frac{a t^2 \sigma_0}{2 F_s}}, \forall t > 0 \quad (3.38)$$

where C is an integration constant, dependent on the initial conditions. Because the system has moved previously over a long distance, assume that the system (3.37) is initially at rest, *i.e.* $\lim_{t \rightarrow 0^-} (\zeta - \bar{\zeta}) = 0$. Owing to the continuity of the solutions to Equation (3.37), the initial condition for (3.38) is $\lim_{t \rightarrow 0^+} \zeta(t) = -\frac{F_s}{\epsilon \sigma_0}$, which implies that the integration constant $C = -2 \frac{F_s}{\epsilon \sigma_0}$. The model perturbation p is evaluated from the combination of (3.23) and (3.38) for $t > 0$

$$p = 2 F_s e^{-\frac{a t^2}{2 F_s}} \left(1 - \frac{\sigma_1}{F_s} a t \right) \quad (3.39)$$

which implies

$$\lim_{t \rightarrow 0^+} \dot{p}(t) = -2 \sigma_1 a \quad (3.40)$$

These theoretical results are illustrated with experimental data in Figure 3.7. The KFM perturbation p is estimated based on Equation (3.22) and an appropriate choice of KFM parameters. The qualitative behavior of the estimated KFM perturbation is in accordance with Equation (3.39). In addition, Relation (3.40) is validated: the slope of p just after the zero velocity transition depends linearly on the acceleration.

Quantitative validation of the result (3.39) can be achieved by matching the theoretical curve for p with the experimental data shown in Figure 3.7. The estimation for the parameters F_s and σ_0 , based on this experiment, is of the same order of magnitude as the results obtained with the identification method proposed in Section 3.4.

The main conclusions that can be deduced from Equation (3.39) are: (i) the amplitude $p(0^+)$ of the KFM perturbation depends on the system parameter F_s only, *i.e.* $p(0^+) = 2F_s$; and (ii) the duration is influenced by both the systems parameters (x_s, F_s, σ_1) and by the acceleration a .

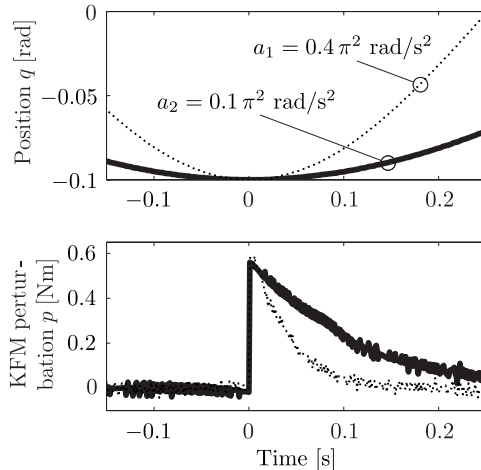


Figure 3.7: Zero velocity transition at constant acceleration.

3.3.5 Discussion of Model Complexity Required

This section presents a singular perturbation analysis of two friction models. The relationship established between the KFM and the *LuGre* model shows that model order reduction with standard singular perturbation methods is possible only for large velocities without velocity reversals. For the particular case of zero velocity transitions at constant acceleration, an analytical expression of the difference between the KFM and the *LuGre* model is presented. It is concluded that the amplitude of this difference equals twice the friction level F_s while duration depends both on system parameters and acceleration.

These rather theoretical results actually mean the following: in order to predict friction for a crane used for loading containers in a harbor, the KFM is sufficient since the required precision is several times larger than the characteristic space constant. On the other hand, the positioning of a machine-tool axis requires the consideration of the *LuGre* model since specified precision is often smaller than the characteristic space constant.

3.4 Model Parameter Identification

Classical identification methods do not apply directly to the determination of the friction model parameters for a given setup, since friction is a nonlinear phenomenon. Therefore, a special approach to parameter estimation is necessary [3, 4, 62]. This section includes the description of a methodology that allows identification of all the parameters of the *LuGre* friction model. For experimental data related to the concepts presented in this section, refer to Section 6.3.3.

As illustrated in Figure 3.8, it is observed that various particular experiments can be

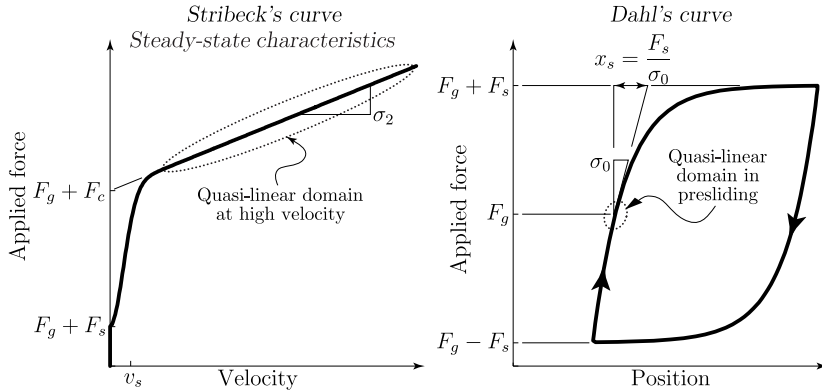


Figure 3.8: Illustration of particular regimes used for identification.

used for parametric identification: (i) the steady-state characteristics of friction force as a function of velocity (Section 3.4.1), (ii) the analysis of the system's dynamics between applied force and measured velocity (or position) at high speeds (Section 3.4.2), (iii) the quasi-linear domain of the presliding regime (Section 3.4.3), and (iv) the position–force relation, called Dahl's curve (Section 3.4.4). A comparison of the usefulness of these approaches is made in Section 3.4.5 where both identification quality and time necessary to obtain the data are considered.

Note: Direct nonlinear estimation schemes based on only one, sufficiently rich experiment, have failed to provide an acceptable parameter estimation.

3.4.1 Steady-State Velocity–Friction Force Characteristics

Define the steady-state by $\dot{z} = 0$ and $\ddot{q} = 0$. The zero acceleration implies that motion is unidirectional, *i.e.* $\text{sign}\dot{q} = \text{constant}$. Then the model (3.5), (3.8) and (3.10) reduces to the static relation

$$u = F_g + \sigma_2 \dot{q} + \left(F_c + (F_s - F_c) e^{-(\dot{q}/v_s)^2} \right) \text{sign}\dot{q} \quad (3.41)$$

Note that this relation is nonlinear in the variable \dot{q} as well as in the parameters F_s , F_c , and v_s . Therefore, a classical least-squares algorithm does not apply. Nevertheless, by means of nonlinear optimization techniques, certain cost function (*e.g.* the Euclidian norm of the prediction error vector) can be minimized.

In order to measure one point of the steady-state velocity–friction force characteristics, the velocity of the system has to be kept constant for a considerable time. Since the system is characterized by low damping and perturbations are present, this is only possible by means of some stabilizing control (*e.g.* PID). In order to obtain reproducible results in the presence of inevitable perturbations, the same path should be followed. Therefore, it is proposed to use a triangular reference position trajectory of fixed amplitude but with

various frequencies in order to obtain information for various velocities. Furthermore, results can depend on the way the points on the static characteristics are stepped through. Various speeds are therefore selected arbitrarily, which allows transformation of systematic perturbations (*e.g.* temperature influences) into noise (random signals) in the measured velocity–torque relation.

By means of the `fminu`-function of the Optimization Toolbox of MATLABTM, parameters can be fitted in order to minimize the mean quadratic prediction error. A comparison of identification results is illustrated in Figure 3.10 at the end of this section. It is easy to estimate parameters F_c , F_g and σ_2 using the steady-state characteristics. In addition, medium quality information about F_s and v_s is available.

3.4.2 High Speeds without Velocity Reversal

Parameter identification within the high speed regime is straightforward and therefore widely used. However, unmodeled process dynamics increase the uncertainty related to the estimated parameter values. Thus, the following description is included for completeness only. This is because the proposed identification methodology is more sensitive to these perturbations than the other approaches presented herein.

If velocity \dot{q} remains constant, the internal friction state z reaches its steady-state value $z_{ss} = g(\dot{q}) \operatorname{sign}\dot{q}$. Moreover, for high speeds characterized by $\dot{q} \gg v_s$, the friction force is given by

$$F = F_c \operatorname{sign}\dot{q} + \sigma_2 \dot{q} \quad (3.42)$$

By substituting $z = z_{ss}$ and $\dot{z} = 0$ in (3.8), the differential equation valid for this regime is

$$J \ddot{q} + \sigma_2 \dot{q} = -F_g - F_c \operatorname{sign}\dot{q} + u \quad (3.43)$$

Note that this system becomes linear in the deviation variable $\tilde{u} = u - F_c \operatorname{sign}\dot{q} - F_g$. In fact, the transfer function from \tilde{u} to q is given by

$$\frac{Q(s)}{\tilde{U}(s)} = \frac{\frac{1}{\sigma_2}}{s \left(1 + s \frac{J}{\sigma_2} \right)} \quad (3.44)$$

Investigation of the system dynamics at high speeds must be done in a closed-loop. The experimental setup is then protected against moving outside its working range. The drawback is that the application of standard open-loop identification techniques is strongly limited. Nevertheless, the theory for frequency response acquisition is well developed even for closed-loop system identification [46, 63].

Measurement and process noise can be eliminated from the experimental frequency response by the intercorrelation method. Suppose, as in Figure 3.9, that the system is stabilized in a discrete time closed-loop configuration around a setpoint q_r with sampling period h . Then an excitation signal $s(kh)$, for example a pseudo random binary noise (PRBS), can be added to the reference or control variable $u(kh)$. Process output is perturbed by $w(kh)$ so that the actual measured signal is $\dot{q}(kh)$. Under a standard hypothesis

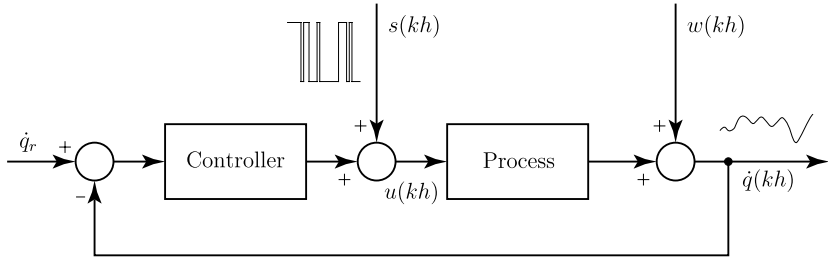


Figure 3.9: Acquisition in closed-loop.

that the signals $s(kh)$ and $w(kh)$ are uncorrelated, the process Fourier transform is given by

$$G(e^{j\omega h}) = \frac{\mathbb{E}[S^*(\omega h)Q(\omega h)]}{\mathbb{E}[S^*(\omega h)U(\omega h)]} \quad (3.45)$$

where $U(\omega h)$ and $Q(\omega h)$ are the discrete Fourier-transforms of $u(kh)$ and $q(kh)$, respectively, while $S^*(\omega h)$ denotes the complex conjugate of $S(\omega h)$. $\mathbb{E}[\cdot]$ gives the expectation of its argument. Note that the evaluation of the Fourier transforms for experimental data requires the multiplication of the signals by, for example a Han-window, to eliminate boundary effects.

The hypothesis that $s(kh)$ and $w(kh)$ are uncorrelated is verified for a large class of perturbations, for example noise in analog lines. It can be shown that, for quantization noise introduced by the analog-to-digital converter, results are reasonable so long as the signal range is 10 times greater than the quantization step.

In general, identification methodologies for linear systems take into account unmodeled process dynamics resulting for example from flexible transmission elements, by appropriate signal filtering. However, no approaches have been found that would reject the influence of nonlinear model perturbations. Unfortunately, considerable position dependent perturbations are often present in standard drives. These perturbations are the torque resulting from variable reluctance, or the influence of geometric machining errors of the elements in relative motion. Hence the noise signal $w(kh)$ is dependent on $u(kh)$ and therefore also on $s(kh)$. This implies that its influence cannot be eliminated by the intercorrelation method. Thus the high velocity experiment provides little, poor and costly information for parameters. Fortunately, identification based on data from the high velocity regime is obsolete since it is possible, with data from the presliding and the steady-state characteristics experiment, to estimate the inertia J and the viscous friction coefficient σ_2 , respectively. This fact is illustrated in Figure 3.10 by a comparison of the identification results.

3.4.3 Small Displacements (Presliding)

The presliding regime is specified by small junction deformation where the internal friction state $|z| \ll g(\dot{q})$. Equation (3.10) reduces to $\dot{z} = \dot{q}$ which after integration leads to

$z = q + q_0$, where q_0 is an integration constant related to displacement for relaxed junctions. The system dynamics within small displacements are described therefore by

$$J\ddot{q} + (\sigma_1 + \sigma_2)\dot{q} + \sigma_0(q + q_0) = u - F_g \quad (3.46)$$

Note that this system, written in the deviation variables $\tilde{q} = q + q_0$ and $\tilde{u} = u - F_g$, is linear. The transfer function is given by

$$\frac{\tilde{Q}(s)}{\tilde{U}(s)} = \frac{\frac{1}{\sigma_0}}{\frac{J}{\sigma_0}s^2 + \frac{\sigma_1 + \sigma_2}{\sigma_0}s + 1} \quad (3.47)$$

The main problem with the presliding regime analysis arises from the correct initialization of the internal state variable z . This variable is related to the mean junction deformation and $z = 0$ corresponds to an absence of stress. It is presumed that this steady-state can be attained by compensating with a constant value $u(t) = u_0$ gravity or other offset terms identified from previously acquired steady-state characteristics. Afterwards, the system is excited, and kept in the presliding regime, by the use of torque signals of amplitude much lower than the break-away torque. Therefore, with the proposed excitation signal $u(t) = u_0 + u_\delta(t)$, where $|u_\delta(t)| < 0.1 \min\{F_c, F_s\}$, open-loop experiments become possible. Obviously, moving into and keeping the system within the region around $z \approx 0$ is a very critical point. Presently, however, there are no alternative methods to achieve this objective than those proposed above.

Since acquisition of experimental data for the presliding regime is achieved in an open-loop, standard identification methods apply. The identification of a parametric model is the optimal selection of a model from a specified model set by minimizing a given performance index. If the identification procedure converges to the global minimum of the cost function, the resulting model provides the best real system representation within the given model set, and for the data supplied. This remark gives rise to two well-known issues: (i) the model validation step becomes mandatory, and (ii) different model structures should be investigated [63]. A general linear model structure can be defined as

$$A(q^{-1})q(kh) = \frac{B(q^{-1})}{F(q^{-1})}u(kh) + \frac{C(q^{-1})}{D(q^{-1})}w(kh) \quad (3.48)$$

where q^{-1} denotes the backward shift operator. In this chapter, only two model structures are considered: (i) the ARX-model, where $C = D = F = 1$ in (3.48), and (ii) the Box–Jenkins (BJ) structure, where $A = 1$.

First consider the identification of the BJ structure. It is a nonlinear optimization problem that can be solved, for example using the Identification Toolbox of MATLAB™. The outcome of the BJ approach gives very satisfactory results, both for the parameter values and for the variances resulting from the use of different data supplied. Note that it is not even necessary to evaluate deviation variables \tilde{u} and \tilde{q} for a given data set because constant perturbations can be integrated in the error model $\frac{C(q^{-1})}{D(q^{-1})}w(kh)$.

Next, the iterative Instrumental Variable (IV) method [101] and the standard least-squares algorithm (LS) are discussed. Noted that the offset term in (3.46) must be removed

by introducing the deviation variables \tilde{u} and \tilde{q} before the ARX-model based methods (LS, IV) are applied. Unfortunately, the LS-method is a biased estimator for the parameters of an ARX-model if noise $w(kh)$ is present. It has been observed experimentally [3] that the viscous friction parameter $\sigma_1 + \sigma_2$ is particularly sensitive to measurement noise. Clearly, the best results are obtained using BJ and IV methods. The choice between these two is context dependent. Note that no theoretical considerations have been found addressing convergence, neither of the nonlinear BJ nor of the iterative IV algorithm. Furthermore, experience has shown that in general, for systems with considerable nonlinearities, methods based on linearization and on PRBS excitation lead to only medium estimation results for the static gain of the system ($\frac{1}{\sigma_0}$ in the case of presliding).

3.4.4 Dahl's Curve

Dahl's curve, shown in Figure 3.8, is a position–force plot acquired for very low velocities. It illustrates the fact that friction acts like a filter, where time scale is replaced by space [16, 17]. Dahl's curve can be used for parameter identification by means of linear methods under the assumption that velocity is constant and small, resulting in $\ddot{q} \approx 0$ and $g(\dot{q}) = \frac{F_s}{\sigma_0}$. Then the model (3.5), (3.8) and (3.10) reduces to

$$\begin{cases} \dot{z} = \dot{q} - \sigma_0 \frac{|\dot{q}|}{F_s} z \\ u = \sigma_0 z + F_g \end{cases} \quad (3.49)$$

Introducing the approximation

$$\dot{x} \approx \frac{x(kh + ah) - x(kh - ah)}{2ah} = \frac{\Delta x(kh)}{2ah} \quad (3.50)$$

where α is an identification parameter and Relation (3.50) transforms (3.49) into the difference equation

$$\Delta u(kh) = \sigma_0 \Delta q(kh) - \frac{\sigma_0}{F_s} |\Delta q(kh)| u(kh) + \frac{\sigma_0 F_g}{F_s} |\Delta q(kh)| \quad (3.51)$$

Since the discrete model (3.51) has the form of an auto-regressive system with linear dependence on parameters, the least-squares or the instrumental variable method can be applied. This approach does not guarantee unbiased results because acquisition is possible in closed-loop only (at least PID position control is required). Nevertheless, it is observed experimentally that results for the parameter σ_0 fit better measured characteristics than the estimation of σ_0 based on the small displacements experiment.

3.4.5 Discussion of Model Parameter Identification

An identification methodology to estimate the parameters of the *LuGre* friction model has been proposed above. The key concept is the use of model properties to identify a reduced number of parameters in the convenient context of linear dynamic systems. This approach allows application of standard identification techniques.

The results, based on different experiments, are illustrated in Figure 3.10. The following identification procedure is proposed:

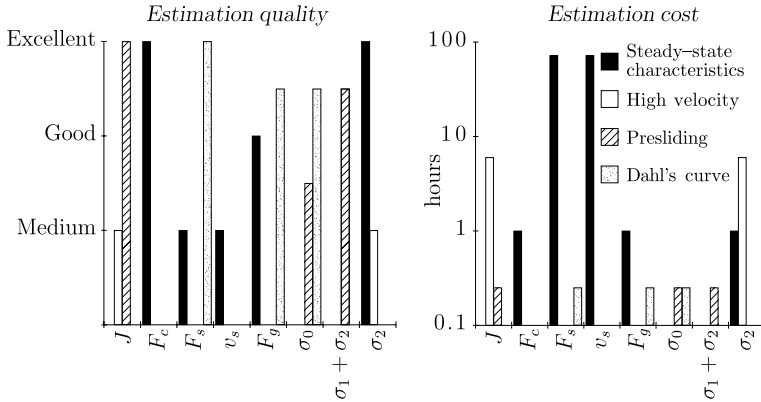


Figure 3.10: Comparison of identification results based on different experiments.

1. Steady-state characteristics: good results for F_c , F_g and σ_2
 - High velocity: quality insufficient
2. Presliding: good results for J and $\sigma_1 + \sigma_2$
3. Dahl's curve: good results for F_s , F_g and σ_0

Note that it is very difficult to estimate the characteristic velocity v_s of the velocity–friction force relationship. To achieve enough data points at low velocity to estimate F_s and v_s , long experimentation (10–100 hours) is mandatory. In addition, it is observed that uncertainty attached to the contribution of gravity and offset terms remains. This is mainly caused by the presence of position dependent perturbations, occasioned by electromagnetic effects or surface irregularities. The relevance of this observation is that both estimations for F_g and σ_0 are influenced by the position at which the identification experiments are carried out.

3.5 Integrated Friction Modeling: A Summary

Integrated friction modeling, as discussed in this chapter, was originally based on input–output observations. Nevertheless, several relations exist with the physical phenomena presented in Chapter 2.

The most important element is the normalization of the KFM by the introduction of the dynamics that are mainly characterized by the two parameters σ_0 and F_s . In a first step, this normalization serves to improve the ability of the model to represent observed phenomena. Furthermore, for dynamic friction models, it is always possible to establish a causal relation between relative velocity and friction force.

The next observation that results from the comparison of the two friction models, is the importance of the material damping, characterized by the parameter σ_1 . This

contribution to the friction force, that was originally introduced for purely numerical reasons, has shown to be well related to physical phenomena and the following chapters show its importance in the synthesis of a stable control loop.

Finally, a complete model parameter identification methodology is proposed which is essential for the practical application of the topics discussed herein.

Chapter 4

Synthesis of PID Controllers

Objectives

- Studying common control approaches
- Motivating and analyzing widely used PI velocity control
- Motivating and analyzing widely used PID position control

CLASSICAL controller synthesis consists of a robust perturbation rejection, implemented, in common practice, with a proportional–integral–derivative (PID) control. This approach is widely used in industry because such a simple and reliable solution is preferred to complex methodologies, presenting the risk of machine damage in case of failure. In order to guarantee reliability, strong stability conditions, explicit in terms of the system parameters, should be obtained for this PID control. The resulting relations enable the user to tune the control algorithm parameters in order to achieve a desired robust performance.

In view of establishing these stability conditions, performances of PID control needs to be analyzed, considering an appropriate friction model. Results for Coulomb's model with static friction have been presented previously [7, 91]. Therein, it has been concluded that a minimal velocity feedback, or viscous damping, is required to achieve asymptotically stable motion. In parallel with the group working at Lund and Grenoble [27], an alternative extension of Dahl's dynamic friction model has been proposed [18]. Therein, in addition to the concept of linear space invariant systems, results have been presented for PID position and PI velocity control. Although these results are useful for the understanding of the performance of PID control applied to drives with friction, they do not help in solving the issues addressed here because Bliman's friction model [18] does not contain a surface material damping term, like the $\sigma_1 \dot{z}$ contribution to the *LuGre* friction force which is governed by Equation (3.9).

No additional literature references have been found that consider the properties achieved with the *LuGre* friction model. Therefore, velocity and position control syn-

thesis is discussed in this chapter, using a PID control structure and by considering the *LuGre* friction model. Global stability proofs are established using a Lyapunov analysis, the small gain theorem, and the passivity method [35, 60, 103].

This chapter is organized as follows. In Section 4.1 it is shown that PI control is required to stabilize the system for a given (constant) reference velocity. Furthermore, in Section 4.2 it is demonstrated that positioning requires a PID control structure to achieve asymptotic stability of the positioning error. An intuitive understanding of transient behavior is difficult when analysis is based on the global, nonlinear properties of the system. Therefore, it is also useful to discuss both control objectives (velocity control and positioning) applying linearization techniques, where time-domain properties are well related to the analysis tools root-locus and Bode plots. The chapter is finally concluded in Section 4.3 with a discussion of the main results. The synthesis of enhanced control algorithms is left to Chapter 5.

4.1 PI Velocity Control

The synthesis of complex industrial control systems is often simplified with an architecture of cascaded control loops. For the electromechanical drive of a machine-tool axis illustrated in Figure 6.10, for example, the first loop is the current control; next, there is the velocity loop; and finally, a position loop is added. In this context of cascaded control loops, the synthesis of velocity control is required to achieve desired global performance.

The structure of controllers implemented in industry is often restricted to PID, since the customer prefers a simple solution, which he is able to maintain himself. Therefore, the only choice remaining is to decide whether to use integral action or not, and whether derivative action is required or not. The response is straightforward when recalling the transfer function (3.44) obtained for large velocities $\dot{q} \gg v_s$. The Laplace transform $\Omega(s)$ of the velocity $\dot{q}(t)$ is here related to the Laplace transform $\tilde{U}(s)$ of the deviation from its steady-state value of the control variable $\tilde{u}(t)$ by

$$\frac{\Omega(s)}{\tilde{U}(s)} = \frac{\frac{1}{\sigma_2}}{1 + \frac{J}{\sigma_2}s} \quad (4.1)$$

To obtain a zero steady-state velocity error, PI control

$$u = k_p \int_{\tau=t_0}^t (\dot{q}_r - \dot{q}) d\tau + k_v(\dot{q}_r - \dot{q}) \quad (4.2)$$

is required, where k_p and k_v denote the controller gains.

4.1.1 Time-Domain Phenomena

The well-known result stating that high PI controller gains are appropriate for increasing the stability is supported by the theoretical considerations presented below. Particularly, the elimination of the stick-slip phenomenon, illustrated in Figure 4.1a, requires minimal position and velocity gains k_p and k_v .

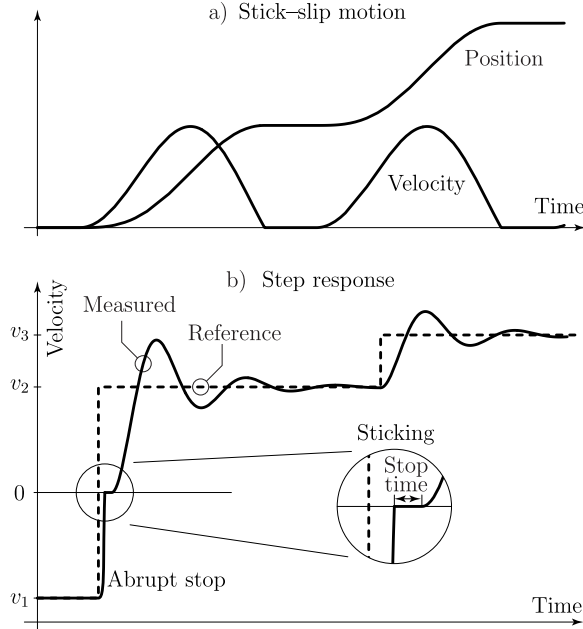


Figure 4.1: Time-domain phenomena for PI velocity control.

An additional motivation for high gain control is related to the limited performance of PI velocity tracking. The macroscopically observed stop time or zero velocity interval resulting at velocity reversals is illustrated in Figure 4.1b with the reference step from v_1 to v_2 . This phenomenon is reduced for high controller gains and large reference steps. However, noise amplification, flexible transmission elements *etc.* impose gain limits. In practice, a compromise has to be found.

Concerning the macroscopically observed zero velocity interval, note that in reality, the absolute zero velocity is present for some particular time instants only. The *LuGre* friction model accounts for this microscopic phenomenon, whilst the KFM predicts only the macroscopic stop time.

Finally, two particular details of the step response can be emphasized. The transition from motion to sticking is in general quite abrupt, whereas the break-away is performed in a relatively smooth manner if $F_s \leq F_c$. A second phenomenon could be deduced from the singular perturbation analysis provided in Section 3.3: the performance for large velocities, for example the step from v_2 to v_3 in Figure 4.1, is almost identical to the behavior of a linear, second order system.

4.1.2 Closed-Loop Synthesis

The closed-loop synthesis is achieved by setting the reference velocity to a constant value $\dot{q}_r = v_0$. In the context of friction compensation, the notion of stability implies the following: (i) for stick-slip motion as illustrated in Figure 4.1a, the system is stable, but not asymptotically stable; and (ii) desired regular motion is equivalent to a global asymptotic stability.

First, the autonomous system equations $\dot{x} = f_g(x)$ for the model (3.5), (3.8), (3.10), and (4.2) are written by defining the state vector

$$\dot{x} = \begin{bmatrix} e \\ \dot{e} \\ z \end{bmatrix} = \begin{bmatrix} \int_{\tau=t_0}^t (\dot{q}_r - \dot{q}) d\tau \\ \dot{q}_r - \dot{q} \\ z \end{bmatrix} \quad (4.3)$$

Equilibrium points of this system are evaluated by solving $f_g(x_{ss}) = 0$. As stability of the steady motion is analyzed, it is further assumed that $v_0 \neq 0$. A brief analysis of the dynamic equations results in the fact that a single isolated solution x_{ss} exists, since it has been assumed $v_0 \neq 0$.

Furthermore, it is convenient to write the system in the deviation variables $\tilde{x} = x - x_{ss}$. This shifts the equilibrium point to the origin and cancels the constant term F_g . The system description becomes $\dot{\tilde{x}} = f(\tilde{x})$, where

$$\dot{\tilde{x}} = \begin{bmatrix} f_1(\tilde{x}) \\ f_2(\tilde{x}) \\ f_3(\tilde{x}) \end{bmatrix} = \begin{bmatrix} \dot{e} \\ -k_p \tilde{e} - (k_v + \sigma_2) \dot{\tilde{e}} + \sigma_0 \tilde{z} + \sigma_1 f_3(\tilde{x}) \\ v_0 - \dot{\tilde{e}} - \frac{|v_0 - \dot{\tilde{e}}|}{g(v_0 - \dot{\tilde{e}})} (\tilde{z} + g(v_0) \text{sign} v_0) \end{bmatrix} \quad (4.4)$$

The objective of the velocity feedback controller is to guarantee regular motion which excludes the stick-slip phenomenon. Thus, global asymptotic stability of the equilibrium point $\tilde{x} = 0$ of the system $\dot{\tilde{x}} = f(\tilde{x})$ must be checked. To achieve this objective, a three step analysis is proposed below:

- (i) It is noted in Section 4.1.3 that global stability is achieved for all physically reasonable parameters. Therefore, system states are always bounded.
- (ii) Conditions for local asymptotic stability are established next in Section 4.1.4. The effort the lubrication industry should make to supply oils and greases leading to a monotonic steady-state relationship between velocity and friction force is motivated by the fact that this property guarantees local asymptotic stability.
- (iii) In order to exclude the stick-slip phenomenon, conditions for global asymptotic stability are provided in Section 4.1.5.

4.1.3 Global Stability

Firstly, stability of the control loop has to be analyzed. Intuitively, owing to the dissipative character of friction, it appears to be natural that the states of the system (4.4) are bounded.

Fact 4.1 System (4.4) has bounded states iff $k_p > 0$ and $k_v + \sigma_2 > 0$.

Proof. Owing to Lemma 3.2, the state \tilde{z} is bounded. From the second row of relation (4.4) \tilde{e} and \tilde{z} are related by

$$J\ddot{\tilde{e}} + (k_v + \sigma_2)\dot{\tilde{e}} + k_p\tilde{e} = \sigma_0\tilde{z} + \sigma_1\dot{\tilde{z}} \quad (4.5)$$

A linear system H with impulse response $h(t)$ is \mathcal{L}_∞ -stable iff $\|H\|_\infty = \|h(t)\|_1 < \infty$ holds. Since $J > 0$, the norms $\|H_v\|_\infty$ and $\|H_p\|_\infty$ of the operators $H_v : \tilde{z} \mapsto \dot{\tilde{e}}$ and $H_p : \tilde{z} \mapsto \tilde{e}$ are bounded iff $k_p > 0$ and $k_v + \sigma_2 > 0$. The relations $\|\dot{\tilde{e}}\|_\infty = \|H_v\|_\infty \|\tilde{z}\|_\infty$ and $\|\tilde{e}\|_\infty = \|H_p\|_\infty \|\tilde{z}\|_\infty$ complete the proof. \blacksquare

The practical relevance of Fact 4.1 is a strong guarantee of reliability: the machine never enters an autodestructive regime for any ‘reasonable’ choice of the controller gains!

If however $\|\dot{\tilde{e}}\|_\infty$ or $\|\tilde{e}\|_\infty$ exceed admissible values, additional security switches are necessary to turn off power in case of failure. Therefore, it would be helpful for controller synthesis to evaluate $\|H_p\|_\infty$ and $\|H_v\|_\infty$ explicitly. Because analytical expressions are relatively complex, guidelines only are sketched below. Consider the two transfer functions

$$H_p(s) = \frac{\sigma_0 + \sigma_1 s}{Js^2 + (k_v + \sigma_2)s + k_p} \quad (4.6)$$

$$H_v(s) = \frac{\sigma_0 s + \sigma_1 s^2}{Js^2 + (k_v + \sigma_2)s + k_p} \quad (4.7)$$

The impulse responses of H_p and H_v are

$$h_p(t) = \begin{cases} \frac{\exp(-\lambda t)}{J\omega_1} \left((\sigma_0 - \lambda\sigma_1) \sin(\omega_1 t) + \sigma_1\omega_1 \cos(\omega_1 t) \right) & \text{if } \eta < 1 \\ \frac{\exp(-\lambda t)}{J} \left((\sigma_0 - \lambda\sigma_1)t + \sigma_1 \right) & \text{if } \eta = 1 \\ \frac{\exp(-\lambda t)}{J\omega_1} \left((\sigma_0 - \lambda\sigma_1) \sinh(\omega_1 t) + \sigma_1\omega_1 \cosh(\omega_1 t) \right) & \text{if } \eta > 1 \end{cases} \quad (4.8)$$

$$h_v(t) = \begin{cases} \frac{\exp(-\lambda t)}{J\omega_1} \left((\sigma_1(\lambda^2 - \omega_1^2) - \sigma_0\lambda) \sin(\omega_1 t) + (\sigma_0 - 2\sigma_1\lambda)\omega_1 \cos(\omega_1 t) \right) & \text{if } \eta < 1 \\ \frac{\exp(-\lambda t)}{J} \left(\lambda(\sigma_0 - \lambda\sigma_1)t + 2\lambda\sigma_1 - \sigma_0 \right) & \text{if } \eta = 1 \\ \frac{\exp(-\lambda t)}{J\omega_1} \left((\sigma_1(\lambda^2 + \omega_1^2) - \sigma_0\lambda) \sinh(\omega_1 t) + (\sigma_0 - 2\sigma_1\lambda)\omega_1 \cosh(\omega_1 t) \right) & \text{if } \eta > 1 \end{cases} \quad (4.9)$$

with $\lambda = \frac{k_v + \sigma_2}{2J}$, $\omega_0 = \sqrt{\frac{k_p}{J}}$, $\eta = \frac{\lambda}{\omega_0}$, and

$$\omega_1 = \begin{cases} \omega_0 \sqrt{1 - \eta^2} & \text{if } \eta < 1 \\ \omega_0 \sqrt{\eta^2 - 1} & \text{if } \eta > 1 \end{cases}$$

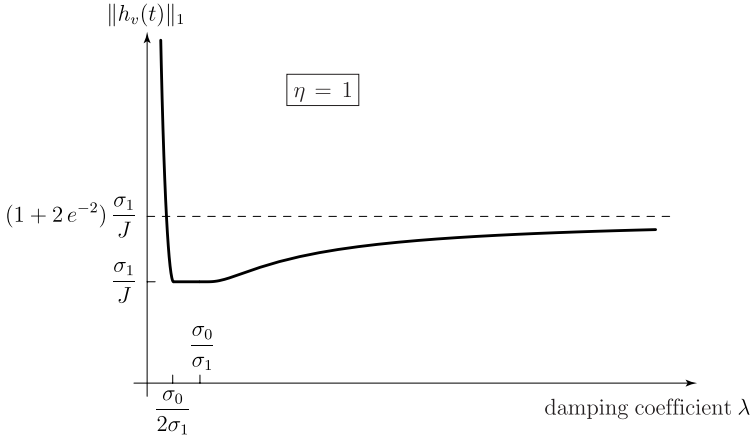


Figure 4.2: Functional analysis: dependence of $\|h_v(t)\|_1$ on λ for $\eta = 1$.

It is useful to examine the particular case of critical damping where $\eta = 1$. In general, *i.e.* if $\sigma_0 \neq \lambda\sigma_1$, there exists exactly one zero of the velocity impulse response, *viz.* $\exists t_1 : h_v(t_1) = 0$ with

$$t_1 = \frac{\sigma_0 - 2\lambda\sigma_1}{\lambda(\sigma_0 - \lambda\sigma_1)} \quad (4.10)$$

Then it is easy to evaluate the one-norm $\|h_v(t)\|_1$, since the indefinite integral $\int h_v(t) dt = h_p(t)$ is known

$$\|h_v(t)\|_1 = \begin{cases} h_p(0) = \frac{\sigma_1}{J} & \text{if } t_1 \leq 0 \\ |2h_p(t_1) - h_p(0)| = \left| \frac{2(\sigma_0 - \lambda\sigma_1)}{J\lambda} \exp\left(-\frac{\sigma_0 - 2\lambda\sigma_1}{\sigma_0 - \lambda\sigma_1}\right) - \frac{\sigma_1}{J} \right| & \text{if } t_1 > 0 \end{cases} \quad (4.11)$$

In order to improve understanding, it is proposed to analyze Equation (4.11) as a function of the damping coefficient λ , resulting in the plot illustrated in Figure 4.2. The corresponding upper bound on the velocity oscillation amplitude $\|\hat{e}\|_\infty$ for an eventual periodic motion is given in the proof of Fact 4.1. Because $\lambda \propto (k_v + \sigma_2) \propto \sqrt{k_p}$ for $\eta = 1$, it can be concluded that, in the region $\lambda < \frac{\sigma_0}{2\sigma_1}$, high gains in k_p and k_v reduce the importance of the phenomenon of stick-slip motion, illustrated in Figure 4.1a. This observation is in agreement with experimental evidence [6, 19, 77, 91].

A similar analysis is certainly possible for the general case $\eta \neq 1$ but the corresponding developments are definitely outside the scope of this work, since the analytical results are very complex.

4.1.4 Local Asymptotic Stability

The results presented in this section are based on the well-known lemmas of Lyapunov's first (indirect) method, relating the stability/instability of a nonlinear system $\dot{\tilde{x}} = f(\tilde{x})$ to the stability/instability of the corresponding linearized system $\dot{\tilde{x}} = \frac{\partial f}{\partial \tilde{x}}|_{\tilde{x}=0} \tilde{x}$.

The goal here is to motivate the effort required from lubrication industry to provide certain properties for the steady-state relationship between velocity and friction force, called for convenience 'steady-state characteristics'.

Linearization

The Jacobian $\frac{\partial f}{\partial \tilde{x}}$ of the nonlinear function $f(\tilde{x})$ specified in (4.4) is continuous in a domain around $\tilde{x} = 0$ delimited by $|\dot{\tilde{x}}| < |v_0|$. This allows the use of linearization techniques to determine local stability properties for all non-zero desired velocities. The concept is to analyze the eigenvalues of the Jacobian

$$A = \left. \frac{\partial f}{\partial \tilde{x}} \right|_{\tilde{x}=0} = \begin{bmatrix} 0 & 1 & 0 \\ -\frac{k_p}{J} & -\frac{k_v + \sigma_2 + \sigma_1 \frac{v_0 g'(v_0)}{g(v_0)}}{J} & \frac{\sigma_0 - \frac{\sigma_1 |v_0|}{g(v_0)}}{J} \\ 0 & -\frac{v_0 g'(v_0)}{g(v_0)} & -\frac{|v_0|}{g(v_0)} \end{bmatrix} \quad (4.12)$$

where $g'(v_0) = \left. \frac{dg(v)}{dv} \right|_{v=v_0}$.

It is well known that the equilibrium point $\tilde{x} = 0$, corresponding to desired continuous motion, of the nonlinear system (4.4) is (locally) asymptotically stable if the matrix A is Hurwitz. Therefore, it is aimed below to find conditions for the controller parameters k_p and k_v that constrain all the eigenvalues of A to have a negative real part.

In general where $F_s \neq F_c$, the root-locus for the linearized system $\dot{\tilde{x}} = A \tilde{x}$ is obtained from the equivalent block diagram depicted in Figure 4.3. It is convenient to consider the location of the roots as a function of the position gain k_p . Furthermore, deviations from equilibrium error and position depending control are denoted by \dot{e} and \dot{u}_p , respectively. When the loop transfer function $G(s)$ is determined analytically, rules for closed-loop root-locus can be applied to give its bounds, asymptotes and critical points. Some algebraic manipulations lead to

$$G(s) = \frac{s + \frac{|v_0|}{g(v_0)}}{s(as^2 + bs + c)} \quad (4.13)$$

where

$$\begin{aligned} a &= J \\ b &= J \frac{|v_0|}{g(v_0)} + k_v + \sigma_2 + \sigma_1 \frac{v_0 g'(v_0)}{g(v_0)} \\ c &= (k_v + \sigma_2) \frac{|v_0|}{g(v_0)} + \sigma_0 \frac{v_0 g'(v_0)}{g(v_0)} \end{aligned}$$

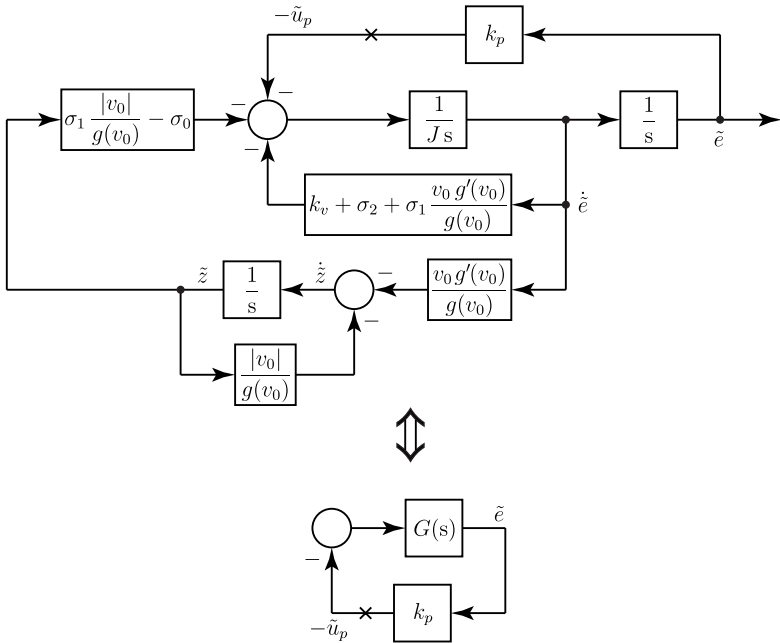


Figure 4.3: Block diagram: linearization for PI velocity control.

The open-loop transfer function $G(s)$ has one zero (denoted by the \circ symbol in Figure 4.4) and three poles (\times symbols). The root-locus presents two vertical asymptotes located at

$$x_a = \frac{\sum_{i=1}^3 p_i - \sum_{j=1}^1 z_j}{3-1} = \frac{-\frac{b}{a} + \frac{|v_0|}{g(v_0)}}{2} = -\frac{k_v + \sigma_2 + \sigma_1 \frac{v_0 g'(v_0)}{g(v_0)}}{2J} \quad (4.14)$$

where p_i and z_j denote the poles and the zeros of the transfer function $G(s)$. Depending on the shape of the steady-state characteristics, three cases can be distinguished: break away friction F_s being equal, smaller and larger than the Coulomb level F_c .

A Break Away Friction Equal to the Coulomb Level

First, consider the case where the steady-state characteristics are perfectly linear. Here, the break away friction equals the Coulomb level $F_s = F_c$ and $g'(v_0) = 0$. Under these assumptions, the eigenvalues of the Jacobian matrix A are given by

$$\lambda_1 = \frac{-k_v - \sigma_2 + \sqrt{(k_v + \sigma_2)^2 - 4Jk_p}}{2J} \quad (4.15)$$

a) High derivative gain k_v b) Medium derivative gain k_v c) Low derivative gain k_v

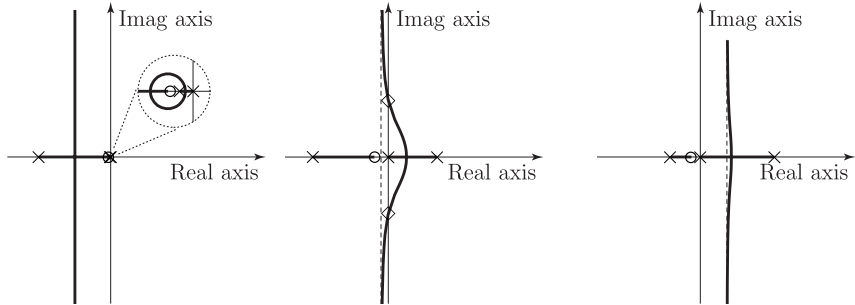


Figure 4.4: Root-locus analysis: linearization for PI velocity control with $F_s > F_c$.

$$\lambda_2 = \frac{-k_v - \sigma_2 - \sqrt{(k_v + \sigma_2)^2 - 4Jk_p}}{2J} \quad (4.16)$$

$$\lambda_3 = -\frac{|v_0|}{g(v_0)} \quad (4.17)$$

Thus, the nonlinear system $\dot{\tilde{x}} = f(\tilde{x})$, specified by (4.4), is (locally) asymptotically stable if $k_v + \sigma_2 > 0$ because all eigenvalues λ_i have negative real parts. The linearized system is overdamped if the position gain verifies

$$k_p < \frac{(k_v + \sigma_2)^2}{4J} \quad (4.18)$$

A Break Away Friction Smaller than the Coulomb Level

If the steady-state characteristics are monotonic, which implies $v_0 g'(v_0) \geq 0, \forall v_0$, then the asymptotes of the root-locus are located in the left complex half plane. In addition, since $c > 0$, the root-locus is completely in the left half plane, *i.e.* the system is asymptotically stable.

These considerations prove that monotonic steady-state characteristics imply local asymptotic stability for PI velocity control. As already mentioned, this fact motivates the request for the lubrication industries to supply oils and greases with the desired property. Nevertheless, note that local asymptotic stability does not exclude the existence of limit cycles (stick-slip motion) if initial conditions are ‘sufficiently’ far from the equilibrium point. This behavior is illustrated in Figure 4.5, where an unstable limit cycle separates the domain of attraction of the desired equilibrium point from the unwanted attractive limit cycle, corresponding to continuous stick-slip motion. In particular, velocity reversals easily drive the system out of the domain of attraction of the desired equilibrium point. Therefore, changing the direction of motion is often at the origin of undesirable ongoing vibrations.

A Break Away Friction Larger than the Coulomb Level

Nonmonotonic steady-state characteristics imply the existence of a domain where $v_0 g'(v_0) < 0$. The root-locus for three possible situations, shown in Figure 4.4, illustrates the fact that augmenting viscous damping k_v increases the range for stabilizing k_p gains. Note that a high k_p is preferred since it increases the closed-loop system bandwidth.

The linearized system is always stable if the root-locus is entirely in the complex left-half plane, see Figure 4.4a. This feature is attained if no open-loop roots are located in the right-half plane, i.e. if $b > 0$ and $c \geq 0$, corresponding to the condition for (local) asymptotic stable motion

$$k_v + \sigma_2 > \max \left\{ -\sigma_1 \frac{v_0 g'(v_0)}{g(v_0)} - J \frac{|v_0|}{g(v_0)}, -\sigma_0 g'(v_0) \operatorname{sign} v_0 \right\} \quad (4.19)$$

If one open-loop pole is in the right-half plane and the asymptotes specified by (4.14) verify $x_a < 0$, then asymptotic stability of the motion depends on the position gain k_p . The intersection of the root-locus with the imaginary axis, marked with the \diamond symbols in Figure 4.4b, is evaluated by imposing a zero remainder to the polynomial division of $s(as^2 + bs + c) + k_p(s + \frac{|v_0|}{g(v_0)})$ by $s^2 + \omega^2$. Stable motion is obtained for k_p satisfying

$$k_p > -\frac{bc}{\sigma_1 \frac{v_0 g'(v_0)}{g(v_0)} + \sigma_2 + k_v} \quad (4.20)$$

This property, namely the extinction of stick-slip oscillations for high position gains, has been observed experimentally [77]. Note that setting the equality in (4.20) leads to a situation where the center manifold theory has to be applied in order to decide whether the nonlinear system is stable or not.

Finally, when the asymptotes are located in the right half plane (see Figure 4.4c), the equilibrium point \tilde{x} is unstable. Therefore the instability condition is

$$k_v + \sigma_2 < -\sigma_1 \frac{v_0 g'(v_0)}{g(v_0)} \quad (4.21)$$

4.1.5 Global Asymptotic Stability

It has been verified in Section 4.1.3 that PI velocity control is stable for any reasonable parameter choice $k_p > 0$ and $\sigma_2 + k_v > 0$. Nevertheless, attractive and unstable orbits, illustrated in Figure 4.5, can exist in state space. In these situations even aperiodic/chaotic motion within the surface separating the domains of attraction of the outer orbit and the equilibrium point cannot be excluded *a priori*.

Conditions guaranteeing (local) asymptotic stability have been proposed in Section 4.1.4, and it is even possible to decide with Relation (4.21) when stick-slip motion is to be expected. In order to complete the analysis, a proof for global asymptotic stability is presented below in two steps: (i) conditions are provided that guarantee global asymptotic stability of a region around the desired equilibrium point, and (ii) additional

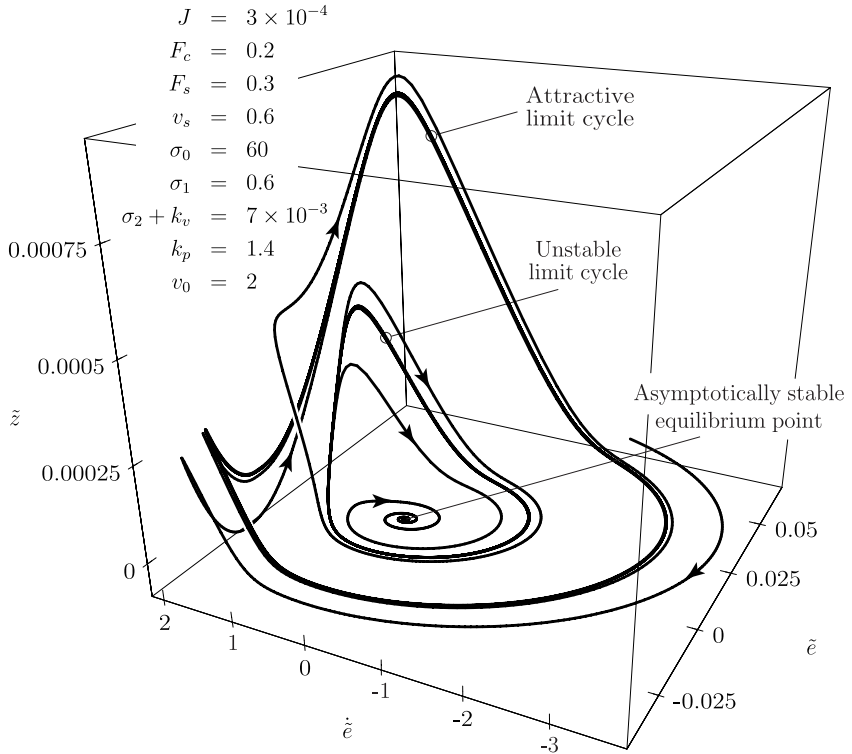


Figure 4.5: Limit cycles observed with PI velocity control (simulation data).

requisites make sure that this region is part of the domain of attraction of the equilibrium. This two-step approach is motivated by the observation that zero velocity transitions are cumbersome to handle whereas unidirectional motion can be analyzed with common tools for nonlinear systems. Therefore, first conditions are provided, that guarantee ultimate stability of a domain where $\text{sign}\dot{q}$ is constant. In the second step, the system behavior within this region is analyzed to find controller parameters that provide asymptotic stability of desired motion.

Lemma 4.1 *For PI velocity regulation, governed by the dynamics (4.4), ϵ exists with $0 < \epsilon < 1 - \alpha$ such that the positive invariant set $\mathcal{D} = \{|\dot{\tilde{e}}| \leq (\alpha + \epsilon)|v_0|\}$ is reached in finite time if*

$$k_p > 3\sigma_0 \left(k_1 + \frac{k_2}{\alpha} \right) \quad (4.22)$$

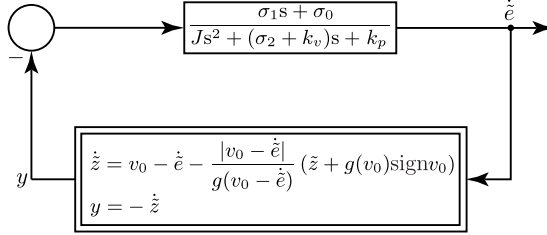


Figure 4.6: Block diagram PI velocity control.

$$k_v + \sigma_2 > \frac{\sigma_0}{\sigma_1} J + 3 \sigma_1 \left(k_1 + \frac{k_2}{\alpha} \right) \quad (4.23)$$

and

$$\frac{k_2}{2\alpha} \leq \frac{1 - \sqrt{1 - \frac{4J \frac{\sigma_0}{\sigma_1^2} \left(\frac{k_p}{\sigma_0} + \frac{k_v + \sigma_2}{\sigma_1} - J \frac{\sigma_0}{\sigma_1^2} \right)}{\left(\frac{k_p}{\sigma_0} + \frac{k_v + \sigma_2}{\sigma_1} + J \frac{\sigma_0}{\sigma_1^2} \right)^2}}}{1 + \sqrt{1 - \frac{4J \frac{\sigma_0}{\sigma_1^2} \left(\frac{k_p}{\sigma_0} + \frac{k_v + \sigma_2}{\sigma_1} - J \frac{\sigma_0}{\sigma_1^2} \right)}{\left(\frac{k_p}{\sigma_0} + \frac{k_v + \sigma_2}{\sigma_1} + J \frac{\sigma_0}{\sigma_1^2} \right)^2}} \cdot \min \left\{ \frac{k_p}{\sigma_0} - 3 \left(k_1 + \frac{k_2}{\alpha} \right), \frac{k_v + \sigma_2 - \frac{\sigma_0}{\sigma_1} J}{\sigma_1} - 3 \left(k_1 + \frac{k_2}{\alpha} \right) \right\}}. \quad (4.24)$$

where $\alpha \in (0, 1)$ is a constant related to the transitional behavior, and

$$k_1 = \frac{\sup g(\cdot) - \inf g(\cdot)}{\inf g(\cdot)} \geq 0 \quad (4.25)$$

$$k_2 = \frac{\sup g(\cdot) + \inf g(\cdot)}{\inf g(\cdot)} > 0 \quad (4.26)$$

It is useful to discuss briefly the conditions of the lemma before presenting its proof: Whilst Relations (4.22)–(4.23) are relatively simple to verify, checking (4.24) is more difficult because, for example, a fixed position gain k_p specifies a closed interval of stabilizing velocity gains k_v . This interval is a function of the system parameters $F_s, F_c, \sigma_0, \sigma_1, \sigma_2$ and J . Precise knowledge of these parameters is therefore required to specify stabilizing gains k_p and k_v . This enhanced modeling effort represents a certain drawback for industrial applications where the cost of parameter identification is often critical. Furthermore, it should be emphasized that the conditions (4.22)–(4.24) are conservative.

Proof. To find a function $V(\tilde{e}, \dot{\tilde{e}})$ such that $\dot{V} < 0, \forall |\dot{\tilde{e}}| \geq (\alpha + \epsilon) |v_0|$ it is useful to separate the linear and the nonlinear parts of the system (4.4).

The linear part $G_1 : \dot{\tilde{z}} \mapsto \dot{\tilde{e}}$ of the system, illustrated in Figure 4.6, is governed by the transfer function

$$G_1(s) = \frac{\sigma_1 s + \sigma_0}{J s^2 + (k_v + \sigma_2)s + k_p} \quad (4.27)$$

Note that $G_1(j\omega)$ is positive real if conditions (4.22)–(4.23) hold. Consider the minimal state representation $\dot{x} = Ax + B\dot{\tilde{z}}$ and $\dot{\tilde{e}} = Cx$ of G_1 in controllable canonical form

$$x = \begin{bmatrix} x_1 \\ x_2 \end{bmatrix}, \quad A = \begin{bmatrix} 0 & 1 \\ -\frac{k_p}{J} & -\frac{k_v + \sigma_2}{J} \end{bmatrix}, \quad B = \begin{bmatrix} 0 \\ 1 \end{bmatrix}, \quad C = \begin{bmatrix} \sigma_0 & \sigma_1 \end{bmatrix} \quad (4.28)$$

Matrices P and Q are chosen to verify the Kalman–Yakubovic–Popov conditions $\frac{1}{2}(PA + A^T P) = -Q$ and $PB = CT$:

$$P = \begin{bmatrix} \frac{k_p \sigma_1 + (k_v + \sigma_2) \sigma_0}{J^2} & \frac{\sigma_0}{J} \\ \frac{\sigma_0}{J} & \frac{\sigma_1}{J} \end{bmatrix}, \quad Q = \begin{bmatrix} \frac{k_p \sigma_0}{J^2} & 0 \\ 0 & \frac{\sigma_1 (k_v + \sigma_2) - \sigma_0 J}{J^2} \end{bmatrix} \quad (4.29)$$

Therefore, P and Q are positive definite if (4.22)–(4.23) hold. With this choice of P and Q , the time derivative of the function $V = \frac{1}{2}x^T Px$ is $\dot{V} = -x^T Qx + \dot{\tilde{z}}\dot{\tilde{e}}$. Introduce the notation

$$\beta := \frac{\tilde{z} + g(v_0)\text{sign}v_0}{g(v_0 - \dot{\tilde{e}})} = \frac{z}{g(v_0 - \dot{\tilde{e}})} \in \left[-\frac{\sup g(\cdot)}{\inf g(\cdot)}, \frac{\sup g(\cdot)}{\inf g(\cdot)} \right] \quad (4.30)$$

then (according to Fact 3.2)

$$\dot{\tilde{z}}\dot{\tilde{e}} = (\pm\beta - 1)\dot{\tilde{e}}^2 + (1 \mp \beta)v_0\dot{\tilde{e}} \quad (4.31)$$

$$\dot{\tilde{z}}\dot{\tilde{e}} \leq \frac{\sup g(\cdot) - \inf g(\cdot)}{\inf g(\cdot)}\dot{\tilde{e}}^2 + \frac{\sup g(\cdot) + \inf g(\cdot)}{\inf g(\cdot)}|v_0\dot{\tilde{e}}| \quad (4.32)$$

and

$$\dot{V} \leq -\frac{k_p}{\sigma_0} \left(\frac{\sigma_0}{J} x_1 \right)^2 - \frac{k_v + \sigma_2 - \frac{\sigma_0}{\sigma_1} J}{\sigma_1} \left(\frac{\sigma_1}{J} x_2 \right)^2 + k_1 \dot{\tilde{e}}^2 + k_2 |v_0| |\dot{\tilde{e}}| \quad (4.33)$$

Setting $\bar{x}_1 = \frac{\sigma_0}{J} x_1$ and $\bar{x}_2 = \frac{\sigma_1}{J} x_2$, and introducing $\dot{\tilde{e}} = \bar{x}_1 + \bar{x}_2$ results in

$$\dot{V} \leq - \left(\frac{k_p}{\sigma_0} - k_1 \right) \bar{x}_1^2 + 2k_1 \bar{x}_1 \bar{x}_2 - \left(\frac{k_v + \sigma_2 - \frac{\sigma_0}{\sigma_1} J}{\sigma_1} - k_1 \right) \bar{x}_2^2 + k_2 |v_0| |\bar{x}_1 + \bar{x}_2| \quad (4.34)$$

To obtain Relations (4.22)–(4.24) it is useful to group the terms $\bar{x}_1 + \bar{x}_2$ in (4.34)

$$\begin{aligned} \dot{V} \leq & - \left(\frac{k_p}{\sigma_0} - k_1 - \frac{k_2}{\alpha} \right) \bar{x}_1^2 + 2 \left(k_1 + \frac{k_2}{\alpha} \right) \bar{x}_1 \bar{x}_2 - \left(\frac{k_v + \sigma_2 - \frac{\sigma_0}{\sigma_1} J}{\sigma_1} - k_1 - \frac{k_2}{\alpha} \right) \bar{x}_2^2 - \\ & - \frac{k_2}{\alpha} (\bar{x}_1 + \bar{x}_2)^2 + k_2 |v_0| |\bar{x}_1 + \bar{x}_2| \end{aligned} \quad (4.35)$$

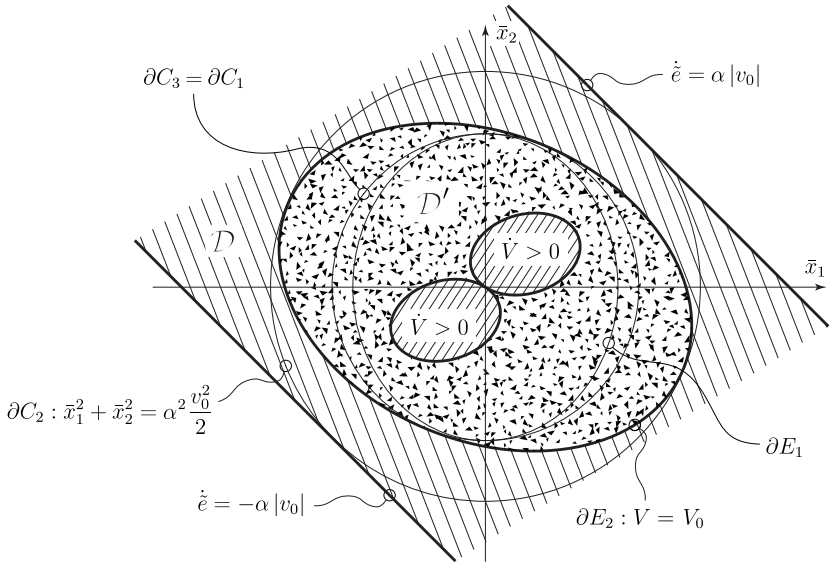


Figure 4.7: PI velocity regulation—Lyapunov analysis.

Because $|\bar{x}_1 \bar{x}_2| \leq \bar{x}_1^2 + \bar{x}_2^2$ and because $-\frac{k_2}{\alpha} (\bar{x}_1 + \bar{x}_2)^2 + k_2 |v_0| |\bar{x}_1 + \bar{x}_2| \leq \frac{k_2}{4} \alpha v_0^2$ Relation (4.35) implies that $\dot{V} < 0$, $\forall(\bar{x}_1, \bar{x}_2)$ such that

$$\left(\frac{k_p}{\sigma_0} - 3 \left(k_1 + \frac{k_2}{\alpha} \right) \right) \bar{x}_1^2 + \left(\frac{k_v + \sigma_2 - \frac{\sigma_0}{\sigma_1} J}{\sigma_1} - 3 \left(k_1 + \frac{k_2}{\alpha} \right) \right) \bar{x}_2^2 > \frac{k_2}{4} \alpha v_0^2 \quad (4.36)$$

With ∂S denoting the border of the set S , the situation, illustrated in Figure 4.7, is discussed below. The ellipsoid ∂E_1 , resulting from setting the equality in (4.36), is enclosed in the circle C_1 specified by

$$\begin{aligned} \partial C_1 : \bar{x}_1^2 + \bar{x}_2^2 = & \frac{\frac{k_2}{4} \alpha v_0^2}{\min \left\{ \frac{k_p}{\sigma_0} - 3 \left(k_1 + \frac{k_2}{\alpha} \right), \frac{k_v + \sigma_2 - \frac{\sigma_0}{\sigma_1} J}{\sigma_1} - 3 \left(k_1 + \frac{k_2}{\alpha} \right) \right\}} \end{aligned} \quad (4.37)$$

To prove that the domain D is reached in finite time, it is sufficient to show that the domain $D' : V = \frac{1}{2}x^T P x \leq V_0$ is reached in finite time for an appropriately chosen V_0 . The ellipsoid E_2 , corresponding to D' in \bar{x}_1 and \bar{x}_2 coordinates is illustrated in Figure 4.7.

It is useful to chose V_0 such that the ellipse $\partial E_2 : V = V_0$ verifies $C_3 \subset E_2 \subset C_2 \subset \mathcal{D}$, where

$$\partial C_2 : \bar{x}_1^2 + \bar{x}_2^2 = \alpha^2 \frac{v_0^2}{2} \quad (4.38)$$

$$\partial C_3 : \bar{x}_1^2 + \bar{x}_2^2 = \alpha^2 \frac{v_0^2}{2} \frac{\lambda_{\min}(P)}{\lambda_{\max}(P)} \quad (4.39)$$

and

$$\frac{\lambda_{\min}(P)}{\lambda_{\max}(P)} = \frac{1 - \sqrt{1 - \frac{4J \frac{\sigma_0}{\sigma_1^2} \left(\frac{k_p}{\sigma_0} + \frac{k_v + \sigma_2}{\sigma_1} - J \frac{\sigma_0}{\sigma_1^2} \right)}{\left(\frac{k_p}{\sigma_0} + \frac{k_v + \sigma_2}{\sigma_1} + J \frac{\sigma_0}{\sigma_1^2} \right)^2}}}{1 + \sqrt{1 - \frac{4J \frac{\sigma_0}{\sigma_1^2} \left(\frac{k_p}{\sigma_0} + \frac{k_v + \sigma_2}{\sigma_1} - J \frac{\sigma_0}{\sigma_1^2} \right)}{\left(\frac{k_p}{\sigma_0} + \frac{k_v + \sigma_2}{\sigma_1} + J \frac{\sigma_0}{\sigma_1^2} \right)^2}}} \quad (4.40)$$

The domain \mathcal{D}' is reached in finite time if the circle C_1 is enclosed in the circle C_3 which results in the condition

$$\underbrace{\frac{k_2}{2\alpha} < \frac{\lambda_{\min}(P)}{\lambda_{\max}(P)} \min \left\{ \frac{k_p}{\sigma_0} - 3 \left(k_1 + \frac{k_2}{\alpha} \right), \frac{k_v + \sigma_2 - \frac{\sigma_0}{\sigma_1} J}{\sigma_1} - 3 \left(k_1 + \frac{k_2}{\alpha} \right) \right\}}_{=: c(a, b)} \quad (4.41)$$

where it is useful to define

$$a := \frac{k_p}{\sigma_0} \quad b := \frac{k_v + \sigma_2 - \frac{\sigma_0}{\sigma_1} J}{\sigma_1} \quad (4.42)$$

Relation (4.41) is illustrated in Figure 4.8 for better understanding. A brief analysis shows that $c(a, b)$ is symmetric about the plane $a = b$ and that the right side of (4.41) cannot be arbitrarily large for large controller gains because

$$\lim_{a = b \rightarrow \infty} c(a, b) = 2J \frac{\sigma_0}{\sigma_1^2} \quad (4.43)$$

which implies that

$$J > \frac{1}{4\alpha} \frac{k_2 \sigma_1^2}{\sigma_0} \quad (4.44)$$

must be checked to verify the conditions of the theorem. If the actual inertia of a drive considered is not sufficient, the present consideration motivates stabilization by means of an additional acceleration feedback. However, this approach is rarely implemented in practice because of the technical limitations that are related to sensor noise and actuator saturation.

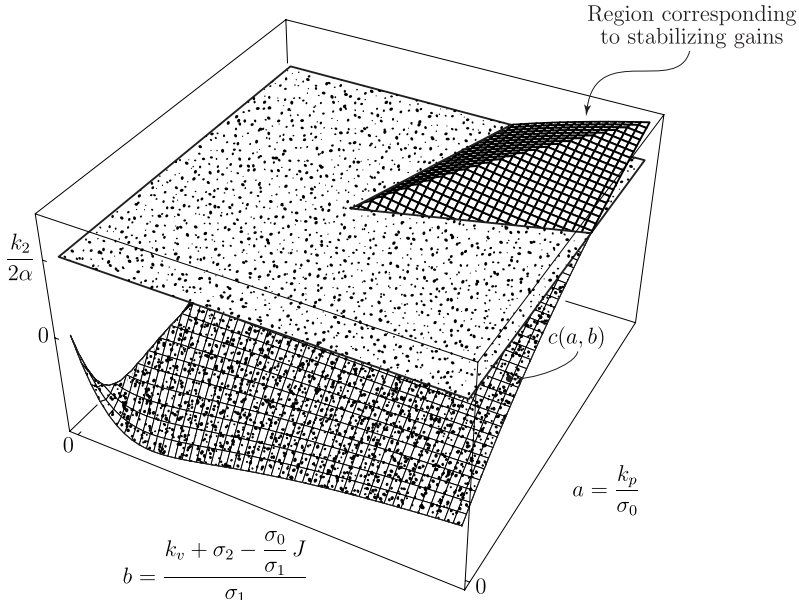


Figure 4.8: PI velocity regulation—stability criterion.

The analysis presented above has shown that

$$\dot{V} < 0 \quad \forall |\dot{\tilde{e}}| > |\alpha v_0| \quad (4.45)$$

if the conditions of the theorem hold, which implies that $\forall \epsilon : 0 < \epsilon < 1 - \alpha \exists t_1 < \infty$ such that

$$|\dot{\tilde{e}}(t)| < (\alpha + \epsilon) |v_0| \quad \forall t > t_1 \quad (4.46)$$

■

Corollary 4.1 Under the conditions of Lemma 4.1 and if the steady-state characteristics are linear

$$F_c = F_s, \quad g(v) = \frac{F_s}{\sigma_0}, \quad k_1 = 0, \quad k_2 = 2 \quad (4.47)$$

then PI velocity regulation is asymptotically stable.

Proof. Observe that the choice of α guarantees that motion is unidirectional $\forall t > t_1$. In this domain, the state \tilde{z} is governed by

$$\begin{aligned} \dot{\tilde{z}} &= -\frac{|v_0 - \dot{\tilde{e}}|}{g(v_0 - \dot{\tilde{e}})} \tilde{z} + (v_0 - \dot{\tilde{e}}) \underbrace{\left(1 - \frac{g(v_0) \text{sign} v_0 \text{sign}(v_0 - \dot{\tilde{e}})}{g(v_0 - \dot{\tilde{e}})}\right)}_{= 0, \text{ if } F_c = F_s} \\ &= 0, \text{ if } F_c = F_s \end{aligned} \quad (4.48)$$

Because the second term in (4.48) is zero \tilde{z} decays exponentially towards zero such that

$$|\tilde{z}(t)| \leq |\tilde{z}(t_1)| \exp\left(-\frac{t}{\min_{\mathcal{D}} \frac{|v_0 - \dot{\tilde{e}}|}{g(v_0 - \dot{\tilde{e}})}}\right) \quad \forall t \geq t_1$$

The system dynamics (4.4) imply also that $\dot{\tilde{e}}$ and \tilde{e} tend exponentially towards zero. ■

Now that it has been shown that the positive invariant set \mathcal{D} of unidirectional motion is reached in finite time, it remains to provide conditions for the controller parameters k_v and k_p guaranteeing that \mathcal{D} is part of the domain of attraction of the desired asymptotically stable equilibrium point. To establish general results for arbitrary steady-state characteristics $g(v)$ the small gain theorem is a conservative, but promising tool. Therefore, the \mathcal{L}_2 -gains of the nonlinear and the linear part of the system are evaluated below.

Lemma 4.2 Consider the system, illustrated in Figure 4.6, and the map $\dot{\tilde{e}} \mapsto y$ governed by

$$\dot{\tilde{z}} = -\frac{|v_0 - \dot{\tilde{e}}|}{g(v_0 - \dot{\tilde{e}})} \tilde{z} + u \quad (4.49)$$

$$y = \tilde{z} \quad (4.50)$$

$$u = \Phi(\dot{\tilde{e}}) = (v_0 - \dot{\tilde{e}}) \left(1 - \frac{g(v_0) \operatorname{sign} v_0 \operatorname{sign}(v_0 - \dot{\tilde{e}})}{g(v_0 - \dot{\tilde{e}})}\right) \quad (4.51)$$

The \mathcal{L}_2 -gain $\gamma_{\dot{\tilde{e}}y}$ of $\dot{\tilde{e}} \mapsto y$, that is $\|y\|_2 \leq \gamma_{\dot{\tilde{e}}y} \|\dot{\tilde{e}}\|_2 + \beta_2$, equals to

$$\gamma_{\dot{\tilde{e}}y} = \left| \sup_{\dot{\tilde{e}} \in \mathcal{D}} \frac{\partial \Phi}{\partial \dot{\tilde{e}}} \right| \sqrt{1 + \left(\frac{\sup_{\dot{\tilde{e}} \in \mathcal{D}} |v_0 - \dot{\tilde{e}}|}{\inf_{\dot{\tilde{e}} \in \mathcal{D}} |v_0 - \dot{\tilde{e}}|} \right)^2} \quad (4.52)$$

where \mathcal{D} is specified in Lemma 4.1 and β_2 is a constant depending on the initial condition $\tilde{z}(t_0)$.

Proof. Introduce the notation

$$\alpha(t) = \frac{|v_0 - \dot{\tilde{e}}|}{g(v_0 - \dot{\tilde{e}})} \geq \inf_{\dot{\tilde{e}} \in \mathcal{D}} \frac{|v_0 - \dot{\tilde{e}}|}{g(v_0 - \dot{\tilde{e}})} = \alpha_0 > 0 \quad (4.53)$$

then

$$y = y_0 \Psi(t, 0) + \int_0^t \Psi(t, \tau) u(\tau) d\tau \quad (4.54)$$

where the state transition function is

$$\Psi(t, \tau) = \exp\left(-\int_\tau^t \alpha(\tau) d\tau\right) \leq e^{-\alpha_0(t-\tau)} = \Psi_0(t, \tau) \quad (4.55)$$

The triangle inequality results in

$$\|y\|_2 \leq \|y_0 \Psi(t, 0)\|_2 + \left\| \int_0^t \Psi(t, \tau) u(\tau) d\tau \right\|_2 \quad (4.56)$$

and because

$$\sup_{\|u\|_2 = \text{const.}} \left\| \int_0^t \Psi(t, \tau) u(\tau) d\tau \right\|_2 \leq \sup_{\|u\|_2 = \text{const.}} \left\| \int_0^t \Psi_0(t, \tau) u(\tau) d\tau \right\|_2 \quad (4.57)$$

Parseval's theorem leads to

$$\|y\|_2 \leq \frac{|y_0| + \|u\|_2}{\alpha_0} \quad (4.58)$$

Therefore, the \mathcal{L}_2 -gain of the map $u \mapsto \dot{z}$, is

$$\gamma_{u\dot{z}} = \frac{1}{\inf_{\dot{\epsilon} \in \mathbb{D}} \frac{|v_0 - \dot{\epsilon}|}{g(v_0 - \dot{\epsilon})}} \quad (4.59)$$

and it follows that the \mathcal{L}_2 -gain of the map $u \mapsto \ddot{z}$ is

$$\gamma_{u\ddot{z}} = \sqrt{1 + \left(\frac{\sup_{\dot{\epsilon} \in \mathbb{D}} \frac{|v_0 - \dot{\epsilon}|}{g(v_0 - \dot{\epsilon})}}{\inf_{\dot{\epsilon} \in \mathbb{D}} \frac{|v_0 - \dot{\epsilon}|}{g(v_0 - \dot{\epsilon})}} \right)^2} \quad (4.60)$$

Finally, note that the constant $0 < \beta_2 < \infty$ could be evaluated explicitly, which however is of no use in practice. ■

Lemma 4.3 Consider the linear part of the system, illustrated in Figure 4.6 which is governed by the transfer function (4.27)

$$G_1(s) = \frac{\sigma_1 s + \sigma_0}{Js^2 + (k_v + \sigma_2)s + k_p}$$

The \mathcal{L}_2 -gain γ_1 of $G_1(s)$, that is $\|\dot{\epsilon}\|_2 \leq \gamma_1 \|y\|_2 + \beta_1$ and β_1 is a constant depending on the initial conditions, is bounded above by

$$\gamma_1 \leq \begin{cases} \frac{\sigma_0}{k_p} & \text{if } k_v + \sigma_2 \leq 2J \frac{\sigma_0}{\sigma_1} \\ \frac{\sigma_1(k_v + \sigma_2)}{2Jk_p} & \text{if } k_v + \sigma_2 > 2J \frac{\sigma_0}{\sigma_1} \end{cases} \quad (4.61)$$

if G_1 is critical- or over-damped

$$k_v + \sigma_2 \geq \sqrt{4k_p J} \quad (4.62)$$

Proof. Trivial. ■

Corollary 4.2 *Under the conditions of Lemma 4.3 and for ‘large’ position gains*

$$k_p \geq J \frac{\sigma_0^2}{\sigma_1^2} \quad (4.63)$$

then

$$\gamma_1 \leq \frac{\sigma_1}{2(k_v + \sigma_2)} \quad (4.64)$$

Theorem 4.1 *PI velocity regulation is globally asymptotically stable if the conditions of Lemma 4.1 and Corollary 4.2 hold and if*

$$k_v + \sigma_2 \geq \frac{1}{2} \sigma_1 \left| \sup_{\dot{\tilde{e}} \in \mathcal{D}} \frac{\partial \Phi}{\partial \dot{\tilde{e}}} \right| \sqrt{1 + \left(\frac{\sup_{\dot{\tilde{e}} \in \mathcal{D}} \frac{|v_0 - \dot{\tilde{e}}|}{g(v_0 - \dot{\tilde{e}})}}{\inf_{\dot{\tilde{e}} \in \mathcal{D}} \frac{|v_0 - \dot{\tilde{e}}|}{g(v_0 - \dot{\tilde{e}})}} \right)^2} \quad (4.65)$$

where

$$\frac{\partial \Phi}{\partial \dot{\tilde{e}}} = g(v_0) \operatorname{sign} v_0 \operatorname{sign}(v_0 - \dot{\tilde{e}}) \frac{g(v_0 - \dot{\tilde{e}}) + (v_0 - \dot{\tilde{e}}) g'(v_0 - \dot{\tilde{e}})}{g^2(v_0 - \dot{\tilde{e}})} - 1 \quad (4.66)$$

Proof. The small gain theorem [35] guarantees that $\|y\|_2$ and $\|\dot{\tilde{e}}\|_2$ are bounded. Because the signals \tilde{e} , $\dot{\tilde{e}}$ and $\ddot{\tilde{e}}$ are bounded (Fact 4.1), also $\ddot{\tilde{e}}$ is bounded which guarantees that the function $\phi(t) = \dot{\tilde{e}}^2(t)$ is a uniformly continuous function on the time interval $t \in [0, \infty)$. Barbalat’s lemma [60] shows that the signal $\dot{\tilde{e}}$ decays to zero. ■

4.1.6 Relevance of the Results for PI Velocity Regulation

The condition (4.65) is conservative because of the use of the small gain theorem. Nevertheless, this result is relevant for practical use because Relation (4.65) is in accordance with the well-known observation that a small viscous damping coefficient $k_v + \sigma_2$ and significant difference between static F_s and kinetic friction F_c “(...) are all favorable to continued vibrations” [91].

The multiplication with σ_1 in (4.65) is a particular property of the *LuGre* model. The statement that a ‘large’ surface material damping σ_1 may be at the origin of stick-slip motion is surprising and no literature references have been found that describe this property for experimental results.

Under the assumption that the *LuGre* model represents all dominant phenomena of friction, the results presented above for PI velocity regulation should be used in the future for an adequate design of drives: to achieve desired motion the bearing should be made of a material with little losses (*e.g.* rolled steel instead of cast iron) and lubrication should be selected so as to guarantee almost linear steady-state characteristics.

4.2 PID Position Control

The synthesis of PI velocity control has been motivated partly by the necessity of adequate performance within an architecture of cascaded control loops. For this approach, the concept is that an outer loop is about 10 times slower than the corresponding inner loop. Unfortunately, this methodology has the disadvantage that in certain situations the separation of time scales of the control loops is incompatible with the application considered.

This motivates the detailed analysis of PID position control presented below. A brief study of the system leads to the decision that both integral action (for a zero permanent error in the presliding regime of friction) and derivative action (to achieve an acceptable overshoot) are required. Therefore, consider the control algorithm

$$u = k_p(q_r - q) + k_v(\dot{q}_r - \dot{q}) + \underbrace{k_i \int_{\tau=t_0}^t (q_r - q) d\tau}_{= u_i} \quad (4.67)$$

where k_p , k_v and k_i denote position, velocity and integral gains, respectively.

In order to explain transient phenomena, observed in particular domains of operation, an analysis using the approach of linearization, considered in Section 4.2.2, is well suited. Nevertheless, in order to exclude globally undesirable oscillations (known as the hunting phenomenon illustrated in Figure 4.9) it is necessary to apply nonlinear techniques, for example the passivity based discussion provided in Section 4.2.3.

4.2.1 Time-Domain Phenomena

Two typical time-domain phenomena are observed for PID position control:

- (i) A limit cycle, called the hunting effect, is frequently observed as soon as the integral action of the controller is switched on. The phenomenon is illustrated in Figures 4.9 and 6.15e.
- (ii) A quite different settling time is observed for the step response (within a range of $\pm 10\%$ of the magnitude of the step) for small and large steps. For ‘small’ displacements, the response is slow, compared to the signals measured for large reference steps. This behavior is illustrated with experimental data in Figure 6.15a–d.

The hunting phenomenon has been extensively discussed for the KFM [7], and it has been shown that also the *LuGre* friction model is able to predict this phenomenon [27]. The main difference between the KFM and the *LuGre* model is that the KFM predicts the hunting effect only if $F_s > F_c$ [7]. In contrast, it is shown below that, to exclude hunting for the *LuGre* model, the position feedback gain k_p must be larger than an explicit lower bound, even in case when $F_s = F_c$. Although, this is not yet a proof of the existence of a limit cycle (because the conditions stated in Theorem 4.2 are conservative) it is nevertheless an indication of a potential problem. Difficulties are related to the surface material damping coefficient σ_1 , which ideally should be made small by mechanical design.

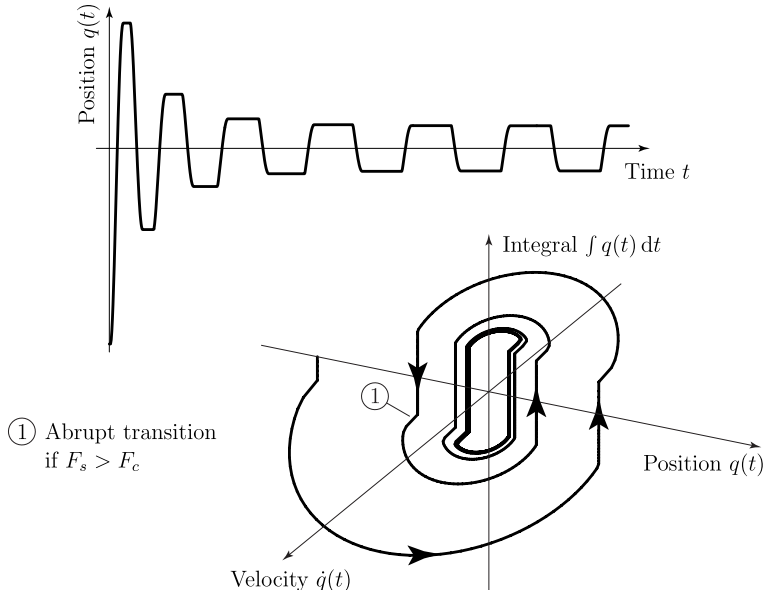


Figure 4.9: Time-domain phenomena for PID position control: the hunting effect.

The particular step response behavior is explained by the frequency domain considerations, presented in Section 4.2.2. In addition, note that the governing parameter is again the characteristic space constant x_s , already used in Section 3.3 for the singular perturbation analysis: a ‘small’ step is specified by a displacement of the same order of magnitude of the characteristic space constant x_s or smaller than x_s .

4.2.2 Simplified PID Synthesis

The approach to parameter identification discussed in Section 3.4 is based on the fact that there are two linear regimes, illustrated in Figure 3.8, for the nonlinear *LuGre* friction model (3.5), (3.8), and (3.10). These regimes are used below for a simplified PID controller synthesis. The results are conditions for local asymptotic stability, and indications about local transient performance.

For high speeds without velocity reversals, characterized by $\dot{q} \gg v_s$, assuming that z has reached its steady-state value $z_{ss} = \text{sign}(\dot{q}) g(\dot{q})$, the system dynamics reduce to

$$J\ddot{q} + \sigma_2\dot{q} + F_g + F_c \text{sign}\dot{q} = u$$

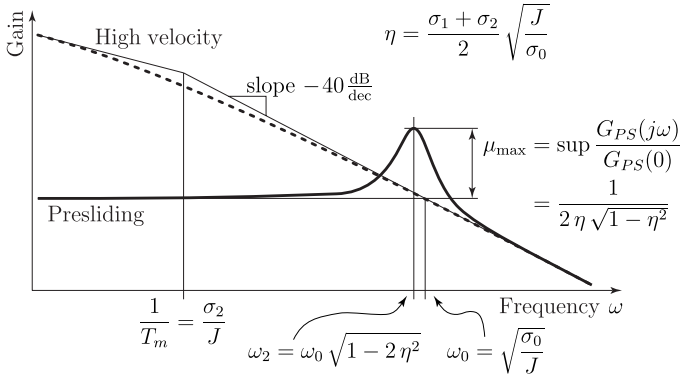


Figure 4.10: Bode analysis of the quasi linear regimes.

and the transfer function for deviation variables is

$$G_{HV}(s) = \frac{\tilde{Q}(s)}{\tilde{U}(s)} = \frac{\frac{1}{\sigma_2}}{s \left(1 + s \frac{J}{\sigma_2} \right)} \quad (4.68)$$

Similarly, the transfer function for small displacements, called presliding regime, is obtained for $|z| \ll g(\dot{q})$

$$G_{PS}(s) = \frac{\tilde{Q}(s)}{\tilde{U}(s)} = \frac{\frac{1}{\sigma_0}}{\frac{J}{\sigma_0} s^2 + \frac{\sigma_1 + \sigma_2}{\sigma_0} s + 1} \quad (4.69)$$

The open-loop Bode diagram for the two transfer functions (4.68) and (4.69) is shown in Figure 4.10. Typically, the mechanical time constant $T_m = \frac{J}{\sigma_2}$ ranges from 0.1 to 10 seconds, the eigenfrequency ω_0 in the presliding regime is located around $100 \frac{\text{rad}}{\text{s}}$, and the relative damping $\eta < 1$ is smaller than one. Furthermore, note that the frequency responses match almost perfectly at ‘high’ frequencies $\omega \gg \omega_0$.

$$G_{PS}(j\omega) \Big|_{\omega \gg \omega_0} \approx G_{HV}(j\omega) \Big|_{\omega \gg \omega_0} \approx \frac{-1}{J\omega^2} \quad (4.70)$$

Based on these two linear regimes, used for identification, controller synthesis can be undertaken by loopshaping. Integral action is required for zero steady-state error in the presliding regime, described by (4.69). Derivative action is necessary to obtain a slope of -20 dB/decade around the crossover frequency, mainly for the high velocity plot.

Small Bandwidth Design

For classical digital controllers, sampling periods range from 1 to 5 milliseconds. Therefore closed-loop bandwidth ω_B should not exceed 100 to 600 rad/s. Controller synthesis based on the Bode plots, shown in Figure 4.10, for the linear regimes ‘high velocity’ and ‘presliding’ provides the following results:

- (i) Design for high velocity leads to a stable solution for both regimes. Nevertheless, Figure 6.15b illustrates that this approach leads to a very slow response for presliding. In addition, the integral term can be at the origin of limit cycles, called hunting.
- (ii) If controller synthesis is based on the presliding regime, it is experimentally observed that instability occurs as soon as the system leaves the presliding regime, *i.e.* this solution is locally stable only. Therefore, such an approach cannot be used for an industrial application.

Large Bandwidth Design

New numerical controllers allow actually sampling periods below 400 microseconds. Therefore, closed-loop bandwidth can be increased. Because the Bode plots for high velocity and presliding in Figure 4.10 match almost perfectly at high frequencies, stable control with excellent performance is achieved for both regimes. In addition, (4.70) shows that only knowledge of the system’s inertia J is required for controller synthesis. This is quite interesting since this approach turns out to be robust with respect to parameter changes in the system. These perturbations are caused by fluctuations in manufacturing (machines of the same type can have different frictional behavior), or temperature variations during operation (*e.g.* difference between winter and summer).

The disadvantage of large bandwidth PID position control is an enhanced requirement on the measurement signal, owing to high feedback gains. Another problem that can arise is related to the existence of flexible transmission elements between motor and load. The corresponding mechanical resonance frequencies are found between 100 Hz and several kHz. Resulting vibrations, observed in common practice, can be eliminated by an appropriately designed notch-filter. However, this also requires high quality sensing. Owing to these problems, often only medium bandwidth design can be applied: in this case, it is observed that the settling times for small and large displacements are comparable, but it also turns out that an undesirable overshoot, illustrated in Figure 6.15c, appears easily for large displacements.

4.2.3 Global Asymptotic Stability

A global approach to synthesis is required since the undesirable hunting phenomenon, illustrated in Figure 4.9, can exist even if the control loop is stable for both linear regimes (high velocity and presliding).

In order to apply the concepts of passivity theory [35], it is necessary to rearrange the system (3.5), (3.8), (3.10) and (4.67) into the form of a ‘suitable’ block diagram. The

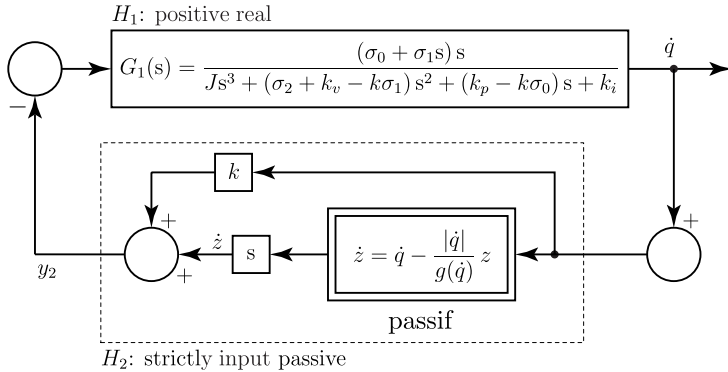


Figure 4.11: Block diagram for PID position control.

term ‘suitable’ emphasizes the fact that this rearrangement can be cumbersome. A block diagram is proposed in Figure 4.11 for the case of a constant reference position $q_r = 0$. The introduction of k is an artifice necessary to acquire general results since the map $\dot{q} \mapsto \dot{z}$ is passive only if $g(\cdot) \equiv \text{const.}$

Theorem 4.2 *Choose any $\varepsilon > 0$ and*

$$k = \frac{\max g(\cdot) - \min g(\cdot)}{\min g(\cdot)} + \varepsilon \quad (4.71)$$

The PID position control loop is globally asymptotically stable if

$$k_p \sigma_0 > k \sigma_0^2 + k_i \sigma_1 \quad (4.72)$$

$$k_v + \sigma_2 > k \sigma_1 + \frac{\sigma_0}{\sigma_1} J \quad (4.73)$$

Proof. In what follows, the conditions of LaSalle’s theorem [60] will be verified. Let $\Omega \in \mathbb{R}^4$ be a compact (closed and bounded) set with the property that every solution of (3.5), (3.8), (3.10) and (4.67) which starts in Ω remains for all future time in Ω . Such a set Ω exists, *i.e.* all the states of the system are bounded, because the denominator of the transfer function

$$G_{z\dot{q}}(s) = \frac{(\sigma_0 + \sigma_1 s) s^2}{J s^3 + (\sigma_2 + k_v) s^2 + k_p s + k_i} \quad (4.74)$$

describing the linear causal map $z \mapsto \dot{q}$ is stable if (4.72)–(4.73) hold, and because the friction state is bounded $z \in \mathbb{C}$.

Second, find a suitable continuous differentiable function $V : \Omega \rightarrow \mathbb{R}$ such that $\dot{V} \leq 0$ in Ω . This objective is achieved by showing: (i) the passivity of the subsystem H_1 in Figure 4.11, and (ii) the strict input passivity of H_2 . The transfer function

$$G_1(s) = \frac{(\sigma_0 + \sigma_1 s)}{J s^3 + (\sigma_2 + k_v - k \sigma_1) s^2 + (k_p - k \sigma_0) s + k_i} \quad (4.75)$$

with k verifying Relation (4.71) is positive real if (4.72)–(4.73) hold. The Kalman–Yakubovich–Popov lemma shows that a positive definite matrix $P \in \mathbb{R}^{3 \times 3}$ and a positive semidefinite matrix $Q \in \mathbb{R}^{3 \times 3}$ exist such that the derivative of the storage function $V = x^T Px$, where $x \in \mathbb{R}^3$ denotes the states of a minimal state space realization of $G_1(s)$, is

$$\dot{V} = -x^T Q x + \underbrace{e_1 \dot{q}}_{= -y_2 \dot{q}} \quad (4.76)$$

Because a particular choice of k guarantees that the map $H_2 : \dot{q} \mapsto y_2$ is strictly input passive

$$y_2 \dot{q} = \dot{z} \dot{q} + k \dot{q}^2 = (1+k) \dot{q}^2 - \frac{|\dot{q}| \dot{q}}{g(\dot{q})} z \geq \left(1+k - \frac{\max g(\cdot)}{\min g(\cdot)}\right) \dot{q}^2$$

the time derivative of V along the solution of the closed-loop system (3.5), (3.8), (3.10) and (4.67) is

$$\dot{V} \leq -x^T Q x - \left(1+k - \frac{\max g(\cdot)}{\min g(\cdot)}\right) \dot{q}^2 \quad (4.77)$$

Third, let E be the set of all points in Ω for which $\dot{q} = 0$. Relation (4.77) implies that system trajectories tend asymptotically to this set. Let M be the largest invariant set in E of the closed-loop system governed by

$$\begin{aligned} \ddot{q} &= -\frac{1}{J} \left((\sigma_2 + k_v) \dot{q} + k_p q + u_i + \sigma_0 z + \sigma_1 \left(\dot{q} - \frac{|\dot{q}|}{g(\dot{q})} z \right) + F_g \right) \\ \dot{u}_i &= k_i q \\ \dot{z} &= \dot{q} - \frac{|\dot{q}|}{g(\dot{q})} z \end{aligned}$$

It follows that the equilibrium manifold M is expressed by $\dot{q} = 0$, $q = 0$, $z \in \mathbb{C}$, where \mathbb{C} is specified by Fact 3.2, and $u_i = \sigma_0 z + F_g$. Note that M is a line segment in Ω .

The system considered is time invariant/autonomous. Therefore, LaSalle's theorem [60] implies that the equilibrium manifold M is asymptotically approached, *i.e.*

$$\lim_{t \rightarrow \infty} \begin{bmatrix} q \\ \dot{q} \\ z \\ u_i \end{bmatrix} = \begin{bmatrix} 0 \\ 0 \\ z_\infty \\ u_{i\infty} \end{bmatrix} \quad (4.78)$$

where $z_\infty \in \mathbb{C}$ is specified by Fact 3.2, and $u_{i\infty} = \sigma_0 z_\infty + F_g$. ■

4.3 Discussion of Results

For PI velocity control, a zero steady-state tracking error is achieved. Monotonic steady-state characteristics guarantee local asymptotic stability. Global asymptotic stability

is achieved for linear steady-state characteristics if the controller gains are large enough, according to (4.22)–(4.24). Therefore, even if system parameters are only known to belong to a certain domain, robust stability can be achieved. However, there is a considerable limitation of PI velocity control, this is the macroscopically observed stop-time at velocity reversals. For small gains and small reference velocities, the stop-time is large.

Similarly, robust stability is achieved for PID position control, if the system parameters are known to belong to a certain domain. Global asymptotic stability of the control loop is guaranteed if conditions (4.72)–(4.73) are verified. Stability does not imply performance. The limitation of PID position control is the observation that small gains lead to very different transient behavior for small and large steps. Arbitrary good performance can be achieved with high controller gains. Nevertheless, the system model is only valid within a certain domain (flexible transmission elements, measurement noise, actuator saturation) which explains the technical limits on the controller gains.

Chapter 5

Enhanced Regulation and Tracking Performance

Objectives

- Presenting a survey of methods for performance enhancement
- Proposing solutions to the problem of friction state observation
- Discussing the topic of robustness versus modeling errors

THE tracking performances, illustrated in Figures 4.1b, 6.14 and 6.15, achieved with a standard PID control architecture are limited and sometimes do not satisfy the specifications for a given application. Furthermore, it may occur that the torque perturbation rejection, or ‘regulation stiffness’, is not satisfactory with PID control.

Therefore it is worthwhile to search for better solutions. If the disturbances in the system have a reasonable amplitude, it is possible to achieve the desired tracking performance by means of model based feedforward friction compensation. In contrast, an increase of torque perturbation rejection can only be achieved with appropriate feedback. To provide the elements of the catalogue of solutions, presented in Chapter 6, here different control algorithms are discussed that lead to enhanced regulation and tracking performances.

Advanced friction compensation has been subject of numerous publications indexed recently [9]. Before the 1990s, performance enhancement was based on the KFM, thereafter dynamic models have also been considered [2, 25, 27, 94]. In fact, it is surprising that Dahl’s friction model, which was developed in the late 1960s and early 1970s, has been used for the synthesis of control only from the beginning of this decade [26].

Firstly in Section 5.1, this chapter presents a survey of feedforward friction compensation techniques. In order to realize feedback compensation, it is necessary to discuss friction state observers—Section 5.2. The estimated state vector resulting is used in Section 5.3 for controller synthesis based on the approach of input–output linearization by

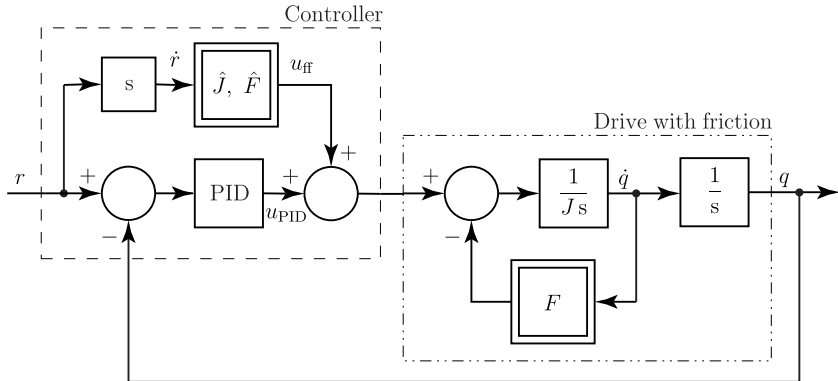


Figure 5.1: Block diagram for model based feedforward friction compensation.

state feedback. The chapter is concluded in Section 5.4 with a summary of the results achieved and some final remarks.

5.1 Feedforward Friction Compensation

The structure of model based feedforward friction compensation is illustrated in Figure 5.1 with a block diagram. In addition to a standard PID control, enhanced tracking performance is achieved with the signal u_{ff} which compensates the friction that would result if $q = r$. Therefore, the key concept is the fact that the compensation signal is based on the reference signal only. Thus, the effects of friction are removed with an exogenous signal, which permits the strong robustness results provided in Section 5.1.3: if the PID control loop is BIBO stable, then the overall system is stable for any choice of the estimated friction model \hat{F} that guarantees a bounded compensation signal u_{ff} .

5.1.1 KFM Based Compensation Applied to the *LuGre* Model

Feedforward friction compensation, based on the KFM, is technically straightforward for simple drives. The friction force resulting from exact tracking of the reference trajectory is calculated and compensated which leads to the feedforward control contribution [5]

$$u_{\text{ff, KFM}} = F_g + J\ddot{r} + \sigma_0 g(\dot{r}) \text{sign}\dot{r} + \sigma_2 \dot{r} \quad (5.1)$$

where the desired reference velocity is denoted by \dot{r} . It has been observed [9] that algorithms of type (5.1) are preferred to feedback solutions in the context of industrial applications. Experimental results achieved with KFM based feedforward compensation have been presented previously together with a comparison of several control approaches [1]. Therein, it is shown that tracking performance is improved with nonlinear model based

feedforward. Experimental results illustrate that the *LuGre* model compensation is required for small displacements of the order of the characteristic space constant x_s , whilst the KFM is sufficient for large displacements.

The KFM based friction compensation has been widely reported. Unfortunately, consistent terminology has not been applied for the term ‘feedforward KFM based compensation’. In certain literature references [56], a contribution $u_c = \hat{F}_c \text{sign}\dot{q}$ to the control action is termed ‘feedforward’ although the compensation signal u_c is obviously based on sensed velocity, representing therefore a ‘feedback’ contribution.

5.1.2 *LuGre* Model Based Compensation

Feedforward friction compensation, based on the *LuGre* model is discussed here in three steps: (i) elaboration of an enhanced velocity control, (ii) extension to positioning, and (iii) discussion of digital implementation issues.

Velocity Control

Model based friction compensation is required in some situations where, for example, the stop time resulting from PI velocity control at velocity reversals (illustrated in Figure 4.1) is not compatible with the application considered. In order to preserve stability of the PI control loop, it is proposed to achieve tracking performance improvement by adding an appropriate system’s inversion based feedforward.

Denoting reference velocity, acceleration and friction state by \dot{r} , \ddot{r} and z_r , respectively, then a feedforward u_{ff} based on the inverse of the system (3.5), (3.8), and (3.10) is

$$u_{\text{ff},\text{LuGre}} = J\ddot{r} + \sigma_2\dot{r} + \sigma_0 z_r + \sigma_1 \left(\dot{r} - \frac{|\dot{r}|}{g(\dot{r})} z_r \right) + F_g \quad (5.2)$$

$$\dot{z}_r = \dot{r} - \frac{|\dot{r}|}{g(\dot{r})} z_r \quad (5.3)$$

The robust stability proofs for the feedforward control scheme that are presented in Section 5.1.3 are based on the assumption that the feedforward control signal is bounded.

Fact 5.1 *The feedforward control signal is bounded $|u_{\text{ff},\text{LuGre}}| < \infty$ for any bounded, differentiable and uniformly continuous reference signal \dot{r}*

Proof. Because z_r is bounded (Fact 3.2)

$$|u_{\text{ff},\text{LuGre}}| \leq J|\ddot{r}| + M(1 + |\dot{r}|)$$

where $M < \infty$ is a constant. ■

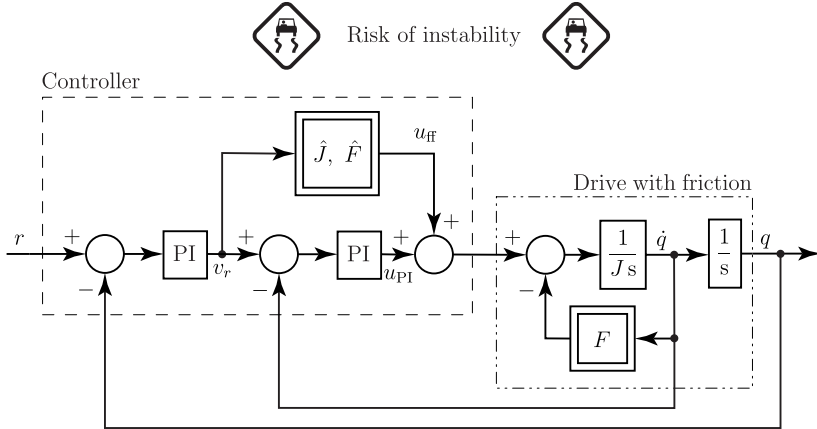


Figure 5.2: Block diagram for cascaded control loops.

Positioning

The architecture for position control is similar to that for velocity control. It should be stressed here that the ‘natural’ approach of cascaded loops, illustrated in Figure 5.2 should not be applied in the design procedure for the following reason: the structure of (5.3) implies for $|z_r| \ll g(v_r)$ the presence of an integrator between the reference velocity v_r of the inner loop and the feedforward control action $u_{ff,LuGre}$:

$$\dot{z}_r \approx v_r \quad \text{if } |z_r| \ll g(v_r) \quad (5.4)$$

Thus, if the reference velocity is generated by a PI position control loop, a double integrator results between the position error and the control signal.

The above motivates the architecture, illustrated in Figure 5.1, with a PID control for perturbation rejection and a model-based feedforward using the reference position to generate an appropriate control contribution u_{ff} that leads to enhanced tracking performance without loss of the robust stability properties

$$e_p = (r - q) \quad (5.5)$$

$$u = u_{ff,LuGre} + k_p e_p + k_d \dot{e}_p + k_i \int_{\tau=t_0}^t e_p d\tau \quad (5.6)$$

where $u_{ff,LuGre}$ is specified by Relations (5.2)–(5.3).

Implementation Issues

Digital implementation of the friction state predictor (5.3) requires particular attention since the z -dynamics can be very fast. In order to solve this problem, an observer modi-

fication has been proposed [2]. In fact the Euler approximation, replacing \dot{z}_r by

$$\dot{z}_r \approx \frac{z_r(kh) - z_r(kh-h)}{h} \quad (5.7)$$

where h denotes the sampling period, leads to serious stability problems. As an alternative to the observer modification, which requires additional attention for parameter tuning, it is proposed to use a formula based on the assumption that \dot{r} remains constant between two samples. Under this condition the system (5.3) is linear and its state transition operator is

$$z_r(kh) = \begin{cases} -a_1 z_r(kh-h) + b_0 \dot{r}(kh) & \forall \dot{r}(kh) \neq 0 \\ z_r(kh-h) & \text{if } \dot{r}(kh) = 0 \end{cases} \quad (5.8)$$

with

$$\begin{aligned} a_1 &= -\exp\left(-\frac{|\dot{r}(kh)|}{g(\dot{r}(kh))} h\right) \\ b_0 &= \frac{g(\dot{r}(kh))}{|\dot{r}(kh)|} (1 + a_1) \end{aligned}$$

Implementing (5.8) leads to an excellent match with reality. For large velocities there is a time-scale separation between the ‘slowly’ varying reference velocity \dot{r} and the ‘rapidly’ varying friction state z_r : the friction state assumes almost instantaneously its steady state value $\frac{F_e}{\sigma_0} \text{sign}\dot{r}$.

5.1.3 Robust Stability

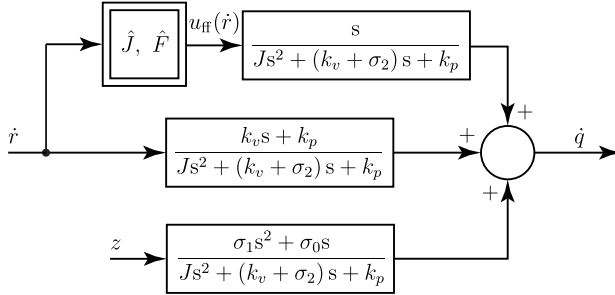
The main advantage of model based feedforward friction compensation is its robustness versus parameter uncertainties that are inherited from the PID feedback design, presented in Chapter 4. Robust stability here means that any ‘sufficiently’ smooth and bounded reference signal leads to a bounded output of the closed-loop system.

Fact 5.2 *The tracking error for control with bounded feedforward, i.e. $u_{\text{ff}} \leq M_{\text{ff}} < \infty$, is bounded for any reasonable choice of the controller parameters that guarantee asymptotic stability of the PID-loop (discussed in Chapter 4).*

Proof. The approach of proving stability is illustrated in Figure 5.3. It is observed that the linear part of the system is driven by bounded signals: Fact 3.2 provides the boundedness of z for any velocity \dot{q} and Fact 5.1 proves that u_{ff} is bounded for any ‘sufficiently smooth’ reference r . The transfer functions, relating the driving signals to the different contributions of the system’s output, is evaluated by writing the linear subsystem in a particular state space form. This leads for velocity control to

$$\begin{bmatrix} \dot{e} \\ \ddot{q} \end{bmatrix} = \begin{bmatrix} 0 & -1 \\ \frac{k_p}{J} & -\frac{k_v + \sigma_2}{J} \end{bmatrix} \begin{bmatrix} e \\ \dot{q} \end{bmatrix} + \begin{bmatrix} 1 \\ \frac{k_v}{J} \end{bmatrix} \dot{r} + \begin{bmatrix} 0 \\ \frac{1}{J} \end{bmatrix} (u_{\text{ff}}(\dot{r}) - \sigma_0 z - \sigma_1 \dot{z}) \quad (5.9)$$

a) PI velocity control



b) PID position control

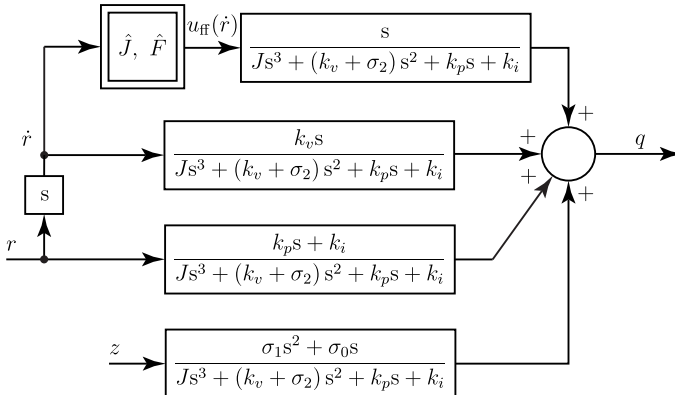


Figure 5.3: Feedforward robustness analysis.

and for positioning to

$$\begin{bmatrix} \dot{u}_i \\ \dot{q} \\ \ddot{q} \end{bmatrix} = \begin{bmatrix} 0 & -k_i & 0 \\ 0 & 0 & 1 \\ \frac{1}{J} & -\frac{k_p}{J} & -\frac{k_v + \sigma_2}{J} \end{bmatrix} \begin{bmatrix} u_i \\ q \\ \dot{q} \end{bmatrix} + \begin{bmatrix} k_i \\ 0 \\ \frac{k_p}{J} \end{bmatrix} r + \begin{bmatrix} 0 \\ 0 \\ \frac{k_v}{J} \end{bmatrix} \dot{r} + \begin{bmatrix} 0 \\ 0 \\ \frac{1}{J} \end{bmatrix} (u_{\text{ff}}(\dot{r}) - \sigma_0 z - \sigma_1 \dot{z}) \quad (5.10)$$

From these state space formulations the transfer functions indicated in Figure 5.3 are deduced directly. It is obvious that the induced infinity and two norms of all these linear subsystems are bounded if the denominators are Hurwitz. Velocity control is therefore stable for any $k_v + \sigma_2 > 0$ and $k_p > 0$. Furthermore, position control is stable if all coefficients of the denominators are positive and if $k_p(k_v + \sigma_2) > Jk_i$, which is true if

(4.72)–(4.73) hold. ■

These conditions are easily verified in practice which indicates the relevance of feed-forward friction compensation in industrial applications: the risk of an accident owing to an unstable control can be excluded even in the presence of considerable uncertainties in the system's parameters! Finally, it is emphasized that such a strong result is certainly not expected for model based feedback friction compensation techniques.

5.1.4 Adaptive *LuGre* Model Based Compensation

Model based feedforward friction compensation is robustly stable, but this property does not allow any conclusion on actual tracking performance. Asymptotic stability of the tracking error is expected for the nominal parameter case only. It is therefore inevitable to have to face the problems of parameter identification and adaptation.

Considerable variations of the parameter values are caused by the dependence on bearing load and preload, temperature and humidity. These environmental conditions, unfortunately, rarely remain constant in industrial applications. In addition, some knowledge of control engineering is required for the use of the identification methodology proposed in Section 3.4. These two facts motivate the elaboration of adaptive control schemes that can serve for an ‘easy to use’ auto-tuning procedure.

Different adaptive control algorithms have been proposed previously. Based on the assumption that either the normal preload or the environmental temperature is unknown, the number of parameters to be estimated on-line have been considerably reduced [25]. Therein, the friction model is modified for the case where the normal preload is unknown

$$\dot{z} = \dot{q} - \theta \frac{|\dot{q}|}{g(\dot{q})} z \quad (5.11)$$

$$F = \sigma_0 z + \sigma_1 \dot{z} + \sigma_2 \dot{q} \quad (5.12)$$

where θ denotes the parameter that must be estimated on-line

$$\dot{\theta} = \gamma \frac{|\dot{q}|}{g(\dot{q})} \hat{z} (\hat{z} - z_m) \quad (5.13)$$

The signal z_m is the ‘measured’ friction state, based on filtered applied torque and velocity signals. The friction state estimate is \hat{z} and γ determines the speed of parameter adaptation.

A more complete adaptive controller synthesis has been presented recently [94, 95]. Therein, the performance of the friction state observer has been improved and adaptation in parallel for several parameters has been considered. Unfortunately, these authors have reformulated the *LuGre* model in order to simplify their *calculi* which makes a comparison with alternative approaches difficult.

Both of these previous methodologies for adaptive friction compensation make extensive use of sensed velocity in both the friction state observer and in the adaptation law. This choice allows establishment of rigorous stability proofs under certain assumptions. Owing to the complexity of these algorithms, however, it is extremely difficult to evaluate

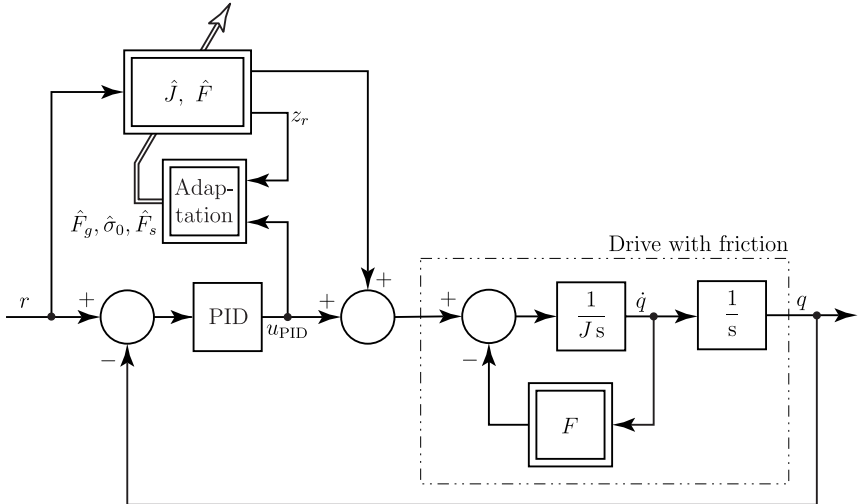


Figure 5.4: Block diagram for adaptive model based feedforward friction compensation.

their robustness versus neglected system properties. Therefore, new algorithms are proposed below which can be used easily and with little risk of catastrophic system behavior in an auto-tuning phase. After this initialization procedure, that can be repeated rapidly several times a day, fixed parameter feedforward friction compensation provides secure operation with enhanced tracking performance.

From the block diagram, illustrated in Figure 5.4, it can be deduced that the output of the PID controller u_{PID} indicates the error between the real system and the model used for feedforward. A mapping from this error signal into parameter space is achieved by multiplication with appropriate signals. The concepts are the following: (i) adaptation is large during periods of time when the influence of the parameter considered on the feedforward control signal is considerable, and (ii) the direction of adaptation is determined based on signals taken within the feedforward block only in order to reduce the risk of instability.

From extended experimental experience, it is observed that adaptation of the parameters for Dahl's curve F_g , σ_0 and F_s is: (i) very interesting from a practical point of view, and (ii) technically straightforward for drives with linear velocity–friction force characteristics where $F_s \approx F_c$. The following ‘semi-intuitive’ adaptation laws are proposed

$$\dot{\hat{F}}_g = \alpha_g u_{\text{PID}} \quad (5.14)$$

$$\dot{\hat{\sigma}}_0 = \alpha_0 u_{\text{PID}} \dot{z}_r \quad (5.15)$$

$$\dot{\hat{F}}_c = \alpha_c u_{\text{PID}} \text{sign} z_r \quad (5.16)$$

where the parameters α_g , α_0 and α_c are chosen to be ‘sufficiently’ small, otherwise a

certain risk exists of instability. These adaptation laws are motivated by the following considerations.

The mean value of the PID control signal estimates the parameter F_g . Therefore, the variation of the parameter estimation is proportional to the actual PID control. It is obvious that the adaptation of the estimated gravity (5.14) is nothing other than an integral term.

The choice for the adaptation of the stiffness at rest (5.15) has been designed such that σ_0 is updated only during zero velocity crossings where the amplitude of the signal \dot{z}_r is considerable and where the influence of the parameter σ_0 on the control action is relevant. In addition, note that the experimental study of the control performance has shown that the product $u_{\text{PID}} \dot{z}_r$ determines a reasonable sign for the parameter adaptation.

A brief analysis of the model results in the observation that it is very difficult to distinguish between the influences of the parameters \hat{F}_g and \hat{F}_c . Different solutions to this problem have been considered previously: multiplication with the sign of the reference velocity sign \dot{r} , with the estimated friction state z_r , and with the sign of the estimated friction state sign z_r . Finally, after an extended experimental study, the last option (5.16) has been retained.

Despite the fact that the adaptation laws (5.14)–(5.16) are very useful in practice, the question of stability arises. It should be noted that the adaptation parameters α_g , α_0 and α_c need to be ‘small’. Furthermore, it is observed experimentally that the ‘smallness’ property of the parameters is related to the amplitude and frequency of the reference signal r , which plays the role of the excitation (necessary for adaptation). Finally, it should be noted that instability can result from an inappropriate choice of the experimental parameters: PID gains k_v , k_p and k_i ; adaptation gains α_g , α_0 and α_c ; shape of the reference r , etc.

5.2 Friction State Observers

In general, the cost of industrial installations is reduced by measuring a limited number of signals only, *i.e.* the full state vector is not available to the controller. Furthermore, in the particular case of drives with *LuGre* model friction, it is not possible to measure the friction state z since this signal is not a physical quantity. Therefore, it is necessary to present an approach for efficient state estimation because enhanced feedback compensation methods, discussed in Section 5.3, require the full state vector.

5.2.1 Tracking Error Based Correction

A tracking error based correction term is proposed in the friction state observer that has been used in the control structure presented by the Lund–Grenoble group [27]

$$\dot{\hat{z}} = \dot{q} - \frac{|\dot{q}|}{g(\dot{q})} \hat{z} + k(r - q) \quad (5.17)$$

where $k > 0$. Proofs for asymptotic tracking of reference velocity and position, respectively, are available [27] making the assumption of exact parameter knowledge. Adaptive

schemes have been analyzed [25], but still under the assumption that the shape of $g(\cdot)$ is known up to a scaling factor.

The Relation (5.17) is a typical observer equation where $-k(r - q)$ denotes the correction term. Because $r - q$ is not necessarily bounded the observer state \hat{z} may not be bounded either. Although asymptotic stability results from a global analysis of the overall system, the fact that \hat{z} is not bounded *a priori* is a drawback because the intrinsic upper and lower bounds of the friction state z provided by Fact 3.2 are very helpful in the stability analysis of PID control. Furthermore, it can be shown by simulation that, already for a small parameter mismatch, bad performance results using the *LuGre*-approach.

5.2.2 Luenberger-like State Observer

In certain applications and for economic reasons only position measurement is available. Thus, not only the friction state z should be observed, but also the velocity \dot{q} . In addition, it is known that the order of the state observer should be as small as possible in order to simplify the problem of stabilization of the closed-loop system. The method introduced for linear systems [64] allows reduction of the order of the state observer to the system's order minus the number of outputs. A friction state observer that applies this concept and requires only position measurement has been proposed for a simple drive with friction [2]. The system (3.5), (3.8), and (3.10) is written in a state space form, with position output $y = q$ appearing explicitly, *i.e.*

$$\begin{cases} \dot{y} &= [1 \ 0] w \\ \dot{w} &= \bar{f}(w) + \begin{bmatrix} 1 \\ J \end{bmatrix} u \end{cases} \quad (5.18)$$

where w denotes the part of the state vector that is to be observed and

$$w = \begin{bmatrix} \dot{q} \\ z \end{bmatrix} \quad (5.19)$$

$$\bar{f}(w) = \begin{bmatrix} -\frac{1}{J} \left(\sigma_0 z + \sigma_1 \left(\dot{q} - \frac{|\dot{q}|}{g(\dot{q})} z \right) + \sigma_2 \dot{q} \right) \\ \dot{q} - \frac{|\dot{q}|}{g(\dot{q})} z \end{bmatrix} \quad (5.20)$$

Furthermore, introducing the notations

$$L = \begin{bmatrix} l_1 \\ l_2 \end{bmatrix} \in \mathbb{R}^2 \quad (5.21)$$

$$\xi = \hat{w} - Lq \quad (5.22)$$

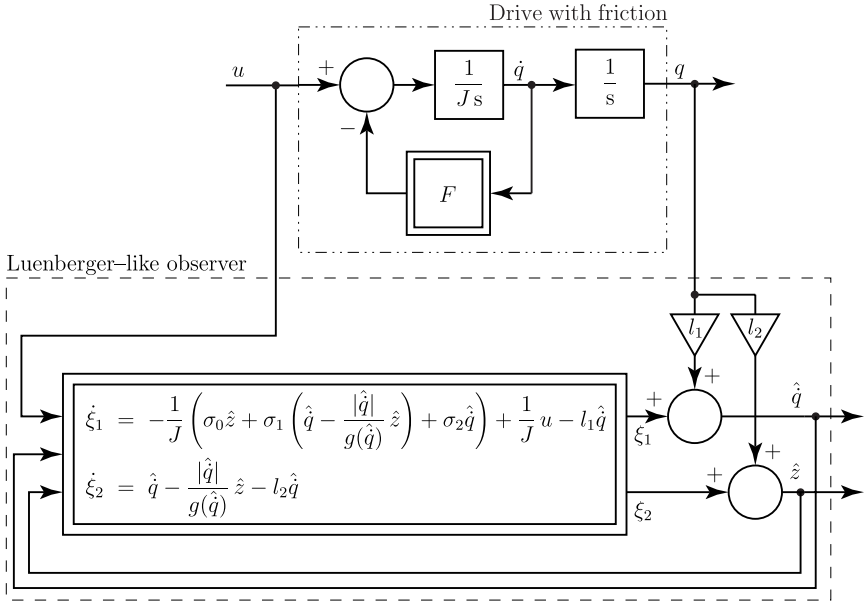


Figure 5.5: Block diagram of a Luenberger-like state observer for a drive with friction.

where L denotes the observer gain vector, and ξ is the observer state vector. Then a Luenberger-like observer for the simple drive with friction is expressed by

$$\begin{aligned} \dot{\xi} &= \bar{f}(\xi + Lq) + \underbrace{\left[\begin{array}{c} \frac{1}{J} \\ 0 \end{array} \right] u - \left[\begin{array}{c} l_1 \\ l_2 \end{array} \right] \left[\begin{array}{cc} 1 & 0 \end{array} \right] (\xi + Lq)}_{= \left[\begin{array}{c} l_1 \\ l_2 \end{array} \right] \hat{q}} \\ &= \left[\begin{array}{c} l_1 \\ l_2 \end{array} \right] \hat{q} \end{aligned} \quad (5.23)$$

A block diagram for Relation (5.23) is shown in Figure 5.5. Note that the observer inputs are the torque u , applied to the drive, and the measured position q .

The observation error $e_{\text{obs}} = w - \hat{w}$ is governed by

$$\dot{e}_{\text{obs}} = \dot{w} - \dot{\hat{w}} = \bar{f}(w) - \bar{f}(\hat{w}) - \left[\begin{array}{cc} l_1 & 0 \\ l_2 & 0 \end{array} \right] e_{\text{obs}} \quad (5.24)$$

where the term $\bar{f}(w) - \bar{f}(\hat{w})$ can be approximated after a first order Taylor expansion of

$\bar{f}(\cdot)$ around the point \hat{w} , *viz.*

$$\bar{f}(w) = \bar{f}(\hat{w}) + \frac{\partial \bar{f}}{\partial w}\Big|_{w=\hat{w}} (w - \hat{w})$$

leading to

$$\dot{e}_{\text{obs}} = \dot{w} - \dot{\hat{w}} \approx \frac{\partial \bar{f}}{\partial w}\Big|_{w=\hat{w}} (w - \hat{w}) - \begin{bmatrix} l_1 \\ l_2 \end{bmatrix} (\dot{q} - \hat{\dot{q}}) = A e_{\text{obs}} \quad (5.25)$$

Therefore, for the Luenberger-like observer of a simple drive with friction, locally and in the nominal parameter case, stability depends on the eigenvalues of A given by

$$\begin{aligned} A &= \frac{\partial \bar{f}}{\partial w}\Big|_{w=\hat{w}} - \begin{bmatrix} l_1 & 0 \\ l_2 & 0 \end{bmatrix} \\ &= \begin{bmatrix} -\frac{1}{J} \left(\sigma_2 + \sigma_1 \left(1 - \hat{z} \frac{g(\hat{q}) \text{sign}\hat{q} + |\hat{q}| g'(\hat{q})}{g^2(\hat{q})} \right) \right) - l_1 & \frac{1}{J} \left(\sigma_1 \frac{|\hat{q}|}{g(\hat{q})} - \sigma_0 \right) \\ 1 - \hat{z} \frac{g(\hat{q}) \text{sign}\hat{q} + |\hat{q}| g'(\hat{q})}{g^2(\hat{q})} - l_2 & -\frac{|\hat{q}|}{g(\hat{q})} \end{bmatrix} \end{aligned} \quad (5.26)$$

where the problem of deriving $|\hat{q}|$ at zero velocity can be solved by defining appropriately the sign-function.

When the estimated state vector is used for control (instead of the actual state vector) then, locally in the state space, the observer poles specified by A append to the closed loop poles of the system. Therefore, it is useful to choose appropriately the observer error dynamics, *i.e.* the eigenvalues of A .

The structure of (5.26) implies that it is not possible to assign any observer error dynamics with an appropriate choice of the observer gain L . Extended simulation of the continuous-time closed-loop system has shown that l_2 does not improve performance. However, a large l_1 leads to a fast response of the velocity estimation error and therefore to a good perturbation rejection: it results directly from (5.26) that, to have a considerable effect on damping, gain l_1 has to be chosen such that $l_1 > \frac{\sigma_1 + \sigma_2}{J}$.

A second relevant property is the dependence of the dynamics on velocity. When $g(\cdot)$ is modeled by a Gaussian function, it is easy to show that for large velocities $|\hat{q}| g'(\hat{q}) = O(0)$. Thus, it is possible to estimate the magnitude of the elements of A as follows

$$A = \begin{bmatrix} O(l_1) & O(\hat{q}) \\ O(1) & O(\hat{q}) \end{bmatrix} \quad (5.27)$$

where, for simplicity, l_2 is chosen to be zero. For large velocities, this leads to the following poles for the observer error dynamics

$$p_{1,2} = \begin{cases} -O(\hat{q}) \\ -O(l_1) + O(1) \end{cases} \quad (5.28)$$

The observer is therefore extremely fast for large velocities which may create certain difficulties related to digital implementation. Therefore, a modification of the observer has been proposed [2], in order to solve this technical problem. Since the troublesome fast observer pole is related to the z dynamics, it has been proposed instead to slow it down by dividing the corresponding vector field component by $1 + \frac{|\hat{q}|}{v_l}$, where the limit velocity v_l is a design parameter. The resulting observer dynamics are

$$\dot{\xi} = \begin{bmatrix} -\frac{1}{J} \left(\sigma_0 \hat{z} + \sigma_1 \left(\hat{q} - \frac{|\hat{q}|}{g(\hat{q})} \hat{z} \right) + \sigma_2 \hat{q} \right) \\ \hat{q} - \frac{|\hat{q}|}{g(\hat{q})} \hat{z} \\ \frac{|\hat{q}|}{1 + \frac{|\hat{q}|}{v_l}} \end{bmatrix} + \begin{bmatrix} \frac{1}{J} \\ 0 \end{bmatrix} u - \begin{bmatrix} l_1 \\ l_2 \end{bmatrix} \hat{q} \quad (5.29)$$

where the choice of v_l has to be made with respect to the sampling period h , for example by limiting the observer dynamics to $0.2\omega_N$ (Nyquist frequency). This leads to

$$v_l = 0.2 \frac{\pi}{h} \frac{F_c}{\sigma_0} \quad (5.30)$$

An alternative problem solution uses the same algorithm (5.8) as the feedforward friction compensation by replacing \dot{r} with \hat{q} in the formulae. Because in continuous time

$$\dot{\xi}_2 = \hat{q} - \frac{|\hat{q}|}{g(\hat{q})} \underbrace{(\xi_2 + l_2 q)}_{= \hat{z}} - l_2 \hat{q} \quad (5.31)$$

the state transition of the observer is governed by

$$\xi_1(kh + h) = \xi_1 - \frac{h}{J} \left(\sigma_0 \hat{z} + \sigma_1 \left(\hat{q} - \frac{|\hat{q}|}{g(\hat{q})} \hat{z} \right) + \sigma_2 \hat{q} - u \right) - h l_1 \hat{q} \quad (5.32)$$

$$\xi_2(kh + h) = \begin{cases} -a_1 \xi_2 + b_0 \left((1 - l_2) \hat{q} - \frac{|\hat{q}|}{g(\hat{q})} l_2 q \right) & \text{if } \hat{q} \neq 0 \\ \xi_2 & \text{if } \hat{q} = 0 \end{cases} \quad (5.33)$$

where the right-hand side is evaluated at kh and

$$\begin{aligned} a_1 &= -\exp \left(-\frac{|\hat{q}|}{g(\hat{q})} h \right) \\ b_0 &= \frac{g(\hat{q})}{|\hat{q}|} (1 + a_1) \end{aligned}$$

This last algorithm has been retained for the experimental comparison, presented in Section 6.3.7, because the direct digital implementation (5.32)–(5.33) seems to be more adequate than the algorithm that results from discretization of the modified observer (5.29).

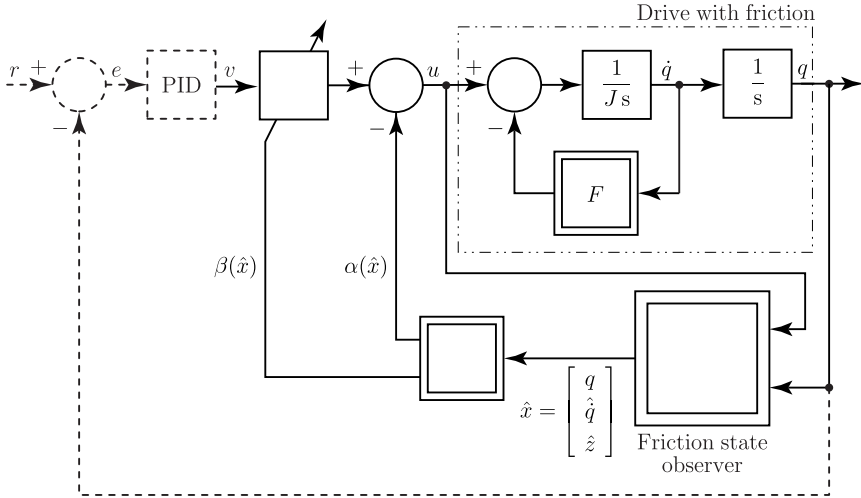


Figure 5.6: Block diagram for input–output linearization by state feedback.

5.3 Input–Output Linearization by State Feedback

The methodology of input–output linearization by state feedback is an approach that allows a modular, and thus simplified, synthesis of the control algorithm. The motivation for linearization techniques, using state feedback, is to achieve a full linearization of the dynamics or, if this is not possible, at least the linearization of the input–output behavior.

The control structure which is based on this approach is illustrated in Figure 5.6 with a block diagram. Owing to the nonlinear characteristics of friction F , it is cumbersome to evaluate exactly the performance that would be achieved with a standard PID controller. Therefore, the linearizing control $u = -\alpha(\hat{x}) + \beta(\hat{x})v$ is introduced. The resulting map between the auxiliary control v and the position signal q is linear under certain assumptions on the observability of the system ‘drive with friction’. In a second step, emphasized by the dashed stroke, a surrounding standard PID control loop can be closed. Then it is straightforward to analyze the overall control performance.

5.3.1 KFM Based Compensation Applied to the *LuGre* Model

Friction compensation based on the *LuGre* model is computationally more complex than a KFM compensation. This motivates an analysis of the performance of a control that uses a KFM based input–output linearization approach, which has been proposed in numerous literature references. Unfortunately, the KFM feedback compensation is rarely applied successfully because undesirable oscillations result easily from this approach. For

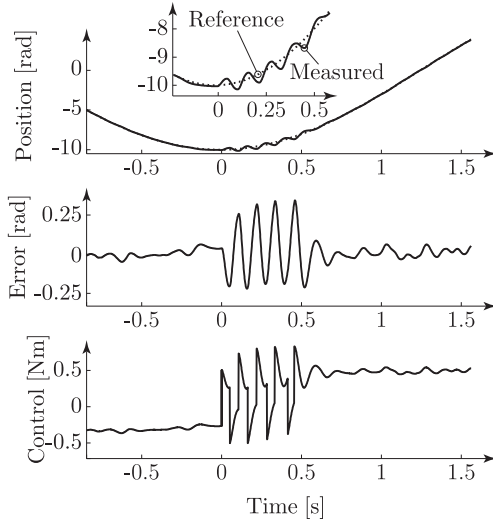


Figure 5.7: Performance of KFM friction compensation based on sensed velocity.

completeness of this text, consider the control

$$u = k_p e + k_v \dot{e} + F_g + J\ddot{r} + \sigma_2 \dot{q} + \sigma_0 g(\dot{q}) \operatorname{sign}\dot{q} + (1 - |\operatorname{sign}\dot{q}|) F_s \operatorname{sign}(k_p e + k_v \dot{e} + J\ddot{r}) \quad (5.34)$$

A simplified version of the control algorithm (5.34), *i.e.* without acceleration feedforward $J\ddot{r}$, has been applied previously to a Toshiba robot and experimental data discussed [61]. The combination of (3.2), (3.22) and (5.34) leads to

$$J\ddot{e} + k_v \dot{e} + k_p e = -p(\dot{e}) \quad (5.35)$$

The perturbation p , specified by (3.23) with $\zeta - \bar{\zeta} = \eta$, can be expressed as a function of the reference \dot{r} , the velocity error $\dot{e} = \dot{r} - \dot{q}$ and the deviation η from the unperturbed model

$$p = -\epsilon (\zeta - \bar{\zeta}) \underbrace{\left(\sigma_0 - \sigma_1 \frac{|\dot{r} - \dot{e}|}{g(\dot{r} - \dot{e})} \right)}_{\eta} \quad (5.36)$$

$$\begin{aligned} \epsilon \dot{\zeta} &= -\underbrace{\frac{|\dot{r} - \dot{e}|}{g(\dot{r} - \dot{e})}}_{\leq 0} (\zeta - \bar{\zeta}) \end{aligned} \quad (5.37)$$

For appropriate controller gains k_v and k_p and for ‘sufficiently’ large reference velocities \dot{r} motion of the drive in closed loop is unidirectional. In this situation, exponential

stability of η is achieved if $F_c = F_s$. The time constant corresponding to the damping of the perturbation p is deduced from (3.31) and (3.33)

$$T_p = \frac{1}{\alpha} = \frac{x_s}{\min(|\dot{r}| - |\dot{e}_{\max}|)} = O(\epsilon) \quad (5.38)$$

In this case, the position and velocity errors $e(t)$ and $\dot{e}(t)$ decay exponentially towards zero. This fact is illustrated in Figure 5.7 with experimental data (it has been observed that $F_s \approx F_c$ for this particular setup and with the lubricant chosen). Just after the zero reference velocity transition, important oscillations are observed. These undesirable vibrations disappear as soon as the reference velocity is ‘sufficiently’ large (around $t = 0.5$ s).

The previous analysis has shown that KFM based feedback compensation can be applied successfully to large velocity tracking tasks. At low velocities and for positioning tasks, undesirable chattering is observed. To achieve better performance for zero velocity transitions, various modifications have been proposed for estimation of the actual velocity of the drive. Many literature references discussing this topic have been cited previously [9]. Nevertheless, until now no satisfactory solutions have been presented.

5.3.2 LuGre Model Based Compensation

Consider the *LuGre* model (3.5), (3.8), and (3.10) for a simple drive with friction. Full state space linearization is not achievable, neither with position nor with velocity measurement, because the system’s relative degree is smaller than its order. In addition, consideration of the friction state z as an output does not make sense in practice. Therefore, only input–output linearization can be achieved. A brief analysis of the equation of motion (3.8) shows that the composite control

$$u = \sigma_0 z - \sigma_1 \frac{|q|}{g(\dot{q})} z + v \quad (5.39)$$

linearizes the relation $v \mapsto \dot{q}$. Note that the term $\sigma_1 \dot{q}$ is not incorporated in (5.39) because this term is: (i) useful by increasing damping, and (ii) does not introduce any nonlinearity. Synthesis for the new control v in an additional step is straightforward using standard linear techniques: therefore, the approach simplifies the work of the control engineer.

The composite control (5.39) has been successfully applied to various systems [2, 25, 27, 94]. However, because the friction state z is not measurable, it has been necessary to analyze different approaches to state observation. The overall control performance is strongly related to the properties of the state observer.

In addition, closed-loop performances and stability are related to the behavior of the zero dynamics, *i.e.* the dynamics of the states for a zero output $q = 0$ and $\dot{q} = 0$. In this situation, the friction state z does not decay asymptotically to zero, but retains its actual value. This implies that for a positioning task where $\dot{q} \rightarrow 0$, asymptotic tracking of the friction state z by the observer state \hat{z} cannot be guaranteed.

5.4 Discussion

Various approaches have been presented in this chapter that achieve enhanced regulation and tracking performance. It is observed that pure feedforward solutions are stable in a relatively large domain of control parameters. Excellent tracking, however, requires knowledge of the friction parameters. The parameter estimation problem can be solved either by the identification methodology, provided in Section 3.4, or by an adaptive scheme, proposed in Section 5.1.4.

If considerable external perturbation is present, large loop-gains are necessary in order to achieve the specified regulation performance. This can be realized with an input-output linearization technique. It has been observed that the *LuGre* model based compensation leads to excellent performance while the KFM based solution exhibits unacceptable chattering for small reference velocities.

Chapter 6

Applications

Objectives

- Illustrating the theoretical considerations of this thesis
- Discussing a particular actuator technology that is based on friction
- Applying PID and enhanced controller synthesis to an industrial drive

MOST previous work on friction modeling and compensation concentrates on specific limited domains: either research was restricted to certain particular mathematical properties, or development focused on one application only, without generalization of the results obtained. However, real improvement of performance requires an interdisciplinary approach, including physics, mechanics, mathematics and control engineering. In addition, the industrial environment of the various applications should be considered for control synthesis.

Therefore, the aim of this chapter is to illustrate the theoretical results presented previously, and also to discuss innovative techniques for high precision actuation of industrial drives. These two possible viewpoints emphasize the relevance of the subjects studied here for further scientific research as well as for industrial applications.

A global discussion of drives with friction has been undertaken previously for the modeling and compensation of friction in an industrial PUMA robot [5]. Therein, in contrast with standard mechanical or tribological textbooks, the topics related to lubrication and friction have been considered from the viewpoint of the control engineer. This approach has led to preliminary results in specifying the dominant phenomena and in identifying the driving parameters.

Because appropriate lubricant selection is extremely important to achieve the desired machine operation, first it is useful to present certain observations on lubricant properties—Section 6.1. Thereafter two applications are examined: (i) the modeling of an inertial drive is presented in Section 6.2, starting from a tribological study of the sur-

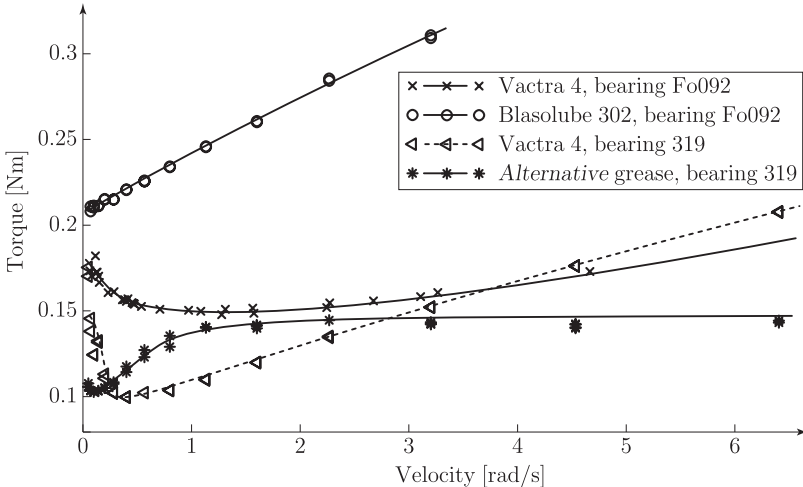


Figure 6.1: Lubricant selection.

faces in relative motion; and (ii) the identification and control of the vertical axis of an industrial electrical-discharge machining installation is discussed in Section 6.3, ending with a catalogue of solutions intended to help the user of drives with friction.

6.1 Lubricant Selection

In order to provide useful hints as to lubricant selection, first, the properties of different lubricants are studied for a pair of ball bearings, manufactured by SKF (part no. BSA 206 C/DFA). The journal diameter is 30 mm, the exterior diameter is 62 mm, and the width is 16 mm. The preload of the bearing is defined both by the tightening of the assembly and by the machining tolerances of the balls and the races.

Different experimental velocity–friction force characteristics are shown in Figure 6.1. Nonmonotonic velocity–friction force characteristics are observed for Mobil Oil Vactra No. 4 lubricant. Although all bearings are of the same dimensions, it is observed that the bearings Fo092 and 319 do not present exactly the same characteristics for Vactra 4 lubrication because the preloading procedure has not been perfectly controlled. Finally, it should be emphasized that the properties of oil lubricated drives can be kept extremely stable over time by continuous lubricant refreshment.

Almost linear velocity–friction force characteristics and high friction levels are observed for the grease Blasolube 302 lubricant. These approximately linear steady-state characteristics are very useful for the synthesis of asymptotically stable control loops. However, note that the observed behavior changes slowly with time because lubricant refreshment is more difficult with grease than with oil.

With *another* widely used grease, monotonic velocity–friction force characteristics are observed with the test procedure considered. However, it is not possible to operate EDM machines, manufactured by Charmilles Technologies S.A., with this grease. This is because of a particular memory effect: very large friction (several times larger than kinetic friction F_c) is experienced for small displacements when passing over the position of a previous reversal point. Because known friction models do not represent this phenomenon, it may become necessary to develop new friction models and associated test procedures that enable characterization of the problems observed in practice with the *alternative*¹ grease that had to be rejected.

Based on the observations presented above, the following decisions were made. Mobil Oil Vactra No. 4 is used for the inertial drive, presented in Section 6.2, because stick-slip motion is a desired phenomenon. The grease Blasolube 302 is applied to the vertical axis used to achieve the experimental data, presented in Section 6.3, and illustrating the results of this research work in the domain of standard and advanced control of drives with friction.

6.2 Modeling of an Inertial Drive

Inertial slider actuators have been developed in the late 1980s [75, 80] for probe positioning in scanning tunneling microscopes. These new actuators present the advantage that extremely fine positioning (in the nanometer range) is possible with high accuracy and at reasonable cost. The load mass of these actuators for microscopic applications is in the order of up to 1 kg. Recently, this technology has been applied [21] to micro-manipulators with loads of a few grams. A ‘smart’ design of the actuator, combining driving and guiding functionalities, is straightforward if the transported loads are relatively small.

The inertial drive shown in Figure 6.2 has been designed and manufactured [29] at the Institut d’automatique during the summer of 1997 for the purpose of illustrating friction phenomena. The conversion from electrical to mechanical energy is realized with a stacked piezoactuator which has very interesting dynamical properties.

This section is organized as follows: first, the experimental setup is described in Section 6.2.1; then, the concepts of operation are explained in Section 6.2.2 using experimental closed-loop data achieved with a simple control algorithm; the properties of the main frictional interface are measured and discussed in Section 6.2.3; and finally, a mathematical model is developed for the complete setup in Section 6.2.4.

6.2.1 Description of the Setup

The stacked piezoactuator, referenced by (1) in Figure 6.3, has a range of 10 μm and can produce a force of up to 500 N. These values are compatible both with the range of the useful friction levels and the gravity contribution for a load of several kilograms. The small mass (2), manufactured from the male part of a V-bearing, is preloaded against

¹Experimental study of the properties does not yet enable deciding whether the undesirable behavior observed is related to this particular product only, or whether this is a general property of greases. Therefore, it is preferred not to indicate the name of the product.

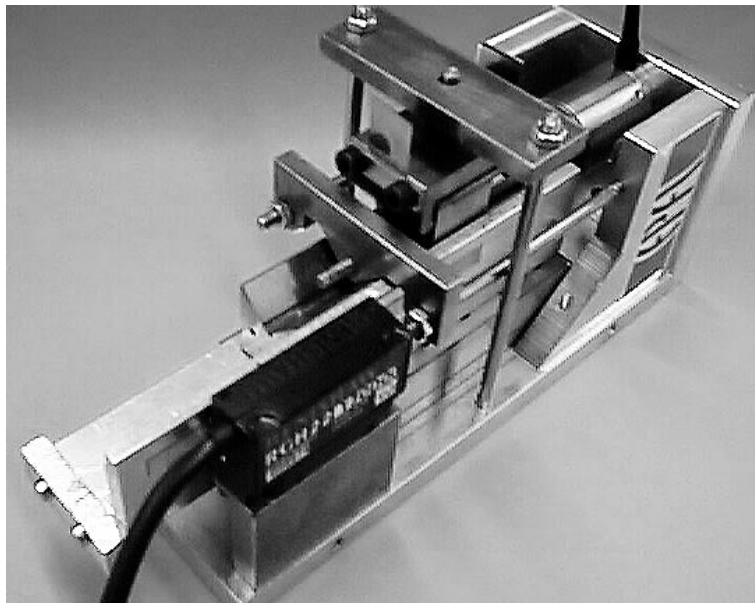


Figure 6.2: Photograph of an inertial drive.

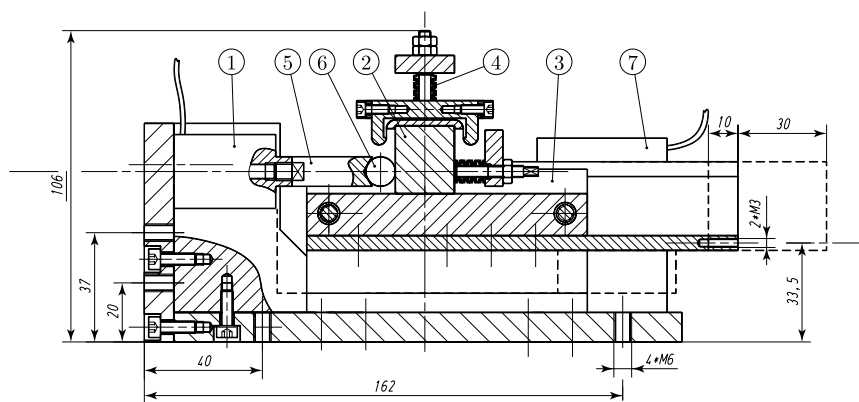


Figure 6.3: Drawing of an inertial drive.

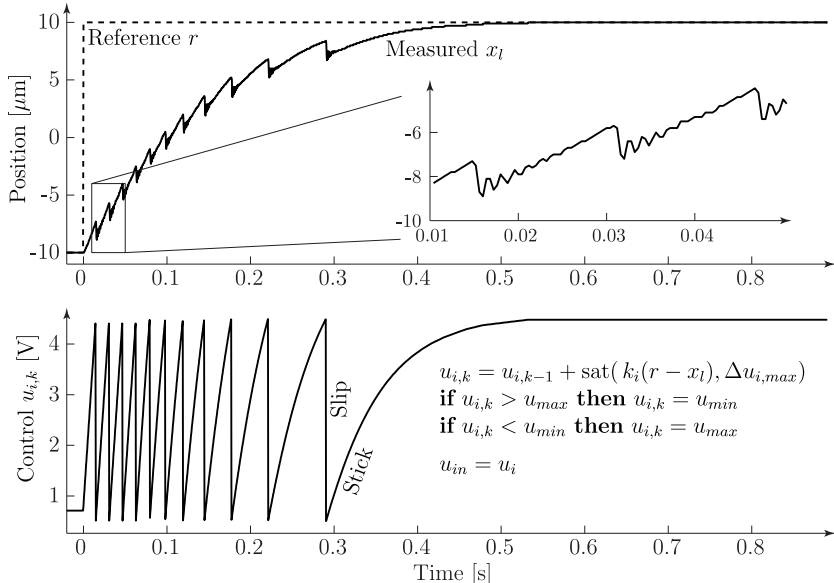


Figure 6.4: Simple stick-slip control.

the female part (3) by means of elastic rings (4). Motion from the piezoactuator to the small mass is transmitted by a shaft (5) and the ball (6) in order to meet geometric and stress requirements. The latter system is also preloaded. Finally, the position of the load, which is fixed rigidly to piece (3), is measured by an incremental optical encoder (7) with a resolution of $0.1 \mu\text{m}$.

6.2.2 Simple Control

To increase understanding of the working principles of an inertial drive, it is worthwhile to observe the performance resulting from the use of a simple controller, as illustrated in Figure 6.4. The reference step of $20 \mu\text{m}$ is tracked after 11 steps (stepping mode). Final position within a range of several microns is achieved in a smooth manner (scanning mode).

More insight into the mechanism of operation is achieved with an analogy to a pizza baker: to place a pizza into the oven, the pastry is slowly introduced with a spatula which is then withdrawn rapidly; the pizza stays approximately where it is, owing to its inertia and the limited friction force between the pastry and the spatula. Owing to this mechanism of operation, where periods of sticking are followed by periods of slipping, inertial actuators are also called stick-slip actuators.

For the inertial drive considered, a step consists of a fast motion of the piezo (1),

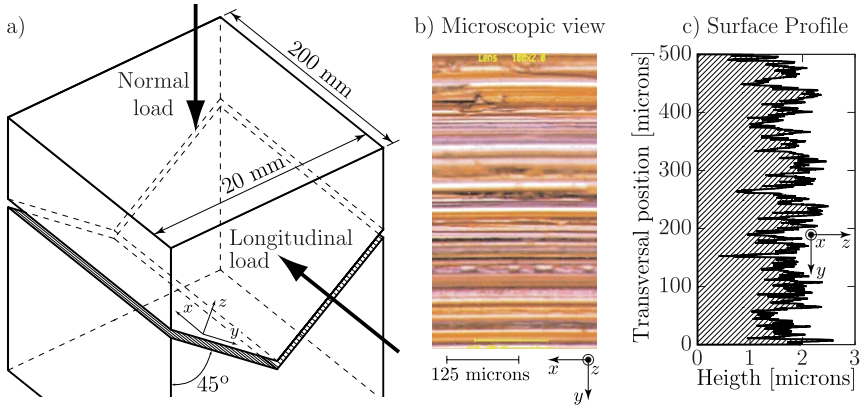


Figure 6.5: Description of the races analyzed.

$$\text{Standard deviation of the height} \quad s = 4.7185 \times 10^{-7} \text{ m}$$

$$\text{Standard deviation of the slope} \quad \dot{s} = 0.5703$$

$$\text{Standard deviation of the curvature} \quad \ddot{s} = 3.4260 \times 10^6 \text{ m}^{-1}$$

$$\text{Density of peaks} \quad D_L = 9.5611 \times 10^5 \text{ # /m}$$

$$\text{Spectrum width parameter} \quad \beta = 0.2464$$

Table 6.1: Statistical parameters of equivalent surface.

leading to slipping at the interface between the slider (2) and the load (3). The resulting mechanical excitation is very rich in frequencies, leading to considerable vibrations. A brief analysis of the position signal shown in Figure 6.4 indicates that the eigenfrequency of the system is located around 600 Hz. These oscillations are caused by the relatively flexible interface between the ball (6) and the flat surface of the slider (2). If these vibrations cannot be eliminated by a better mechanical design, an enhanced control algorithm must be found that increases damping.

6.2.3 Analysis of the V-Bearing

The principal part of an inertial drive is the frictional interface between the slider (2) and the load (3). These parts have been realized in the setup considered with a linear V-bearing. Therefore, exact study of the friction phenomena observed at the interface between these surfaces has been necessary for the mechanical design of the prototype. In addition, these results provide an excellent validation of the tribology theory summarized in Chapter 2.

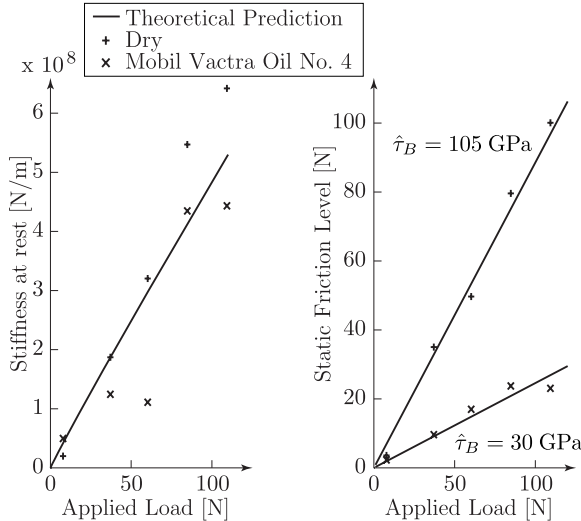


Figure 6.6: Experimental verification of tribological results.

Experimental data is taken from the V-bearing, shown in Figure 6.5a. The longitudinal motion is achieved with manual actuation by a micrometer screw. The experimental setup has been equipped with a capacitive force and with an inductive position sensor (accuracy ± 40 nm). The particular non-isotropic surface topology of the contacting surfaces, illustrated by the microscopic view in Figure 6.5b, is a result of the workpiece finish by milling. The surface profile of the races has been acquired, see Figure 6.5c, and the statistical parameters indicated in Table 6.1 have been evaluated. These parameters and the mechanical constants for the materials of the bearing can be used to evaluate numerically the stiffness at rest that is predicted by Relations (2.7) and (2.17) for different normal preload forces.

Based on the Dahl's curve experiment, discussed in Section 3.4.4, the results shown in Figure 6.6 are achieved. It is observed that the static friction level F_s and the stiffness at rest σ_0 depend linearly on the applied normal load. Therefore, the space constant $x_s = \frac{F_s}{\sigma_0}$ that characterizes Dahl's curve, see Figure 3.8, is independent of normal load N : for the dry contact its value is $x_s = 180$ nm, and for the thick oil film $x_s = 50$ nm.

The measured stiffness at rest is independent of lubrication, which confirms the assumptions proposed in Section 2.3.2; moreover, the theoretical predictions and the experimental data points match. These observations support the statement that the physics related to the properties represented by the parameter σ_0 for very small displacements, are well understood.

In addition, it results from the plots shown in Figure 6.6 that static friction is reduced by the oil film, applied into the interface, by approximately a factor of 3.6. The identified

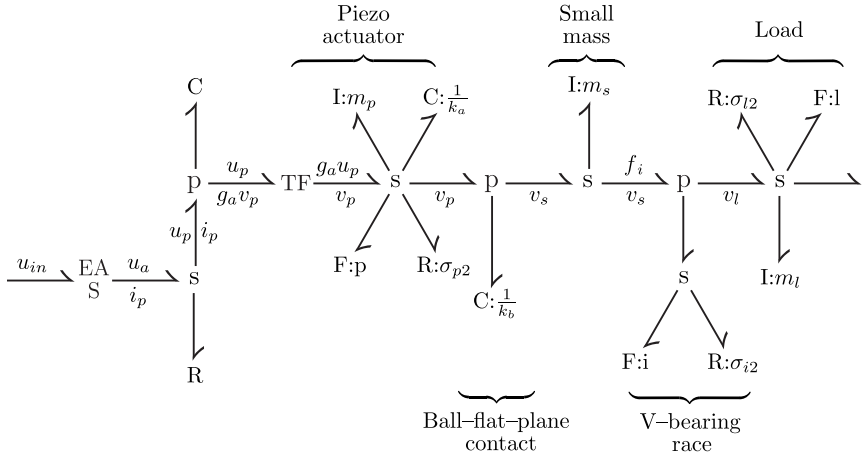


Figure 6.7: Bond graph of an inertial drive.

shear strength τ_B for the unlubricated case is one order of magnitude larger than the value that has been calculated for a clean crystal surface of α -iron [69]. This difference can be explained by imperfections in the crystal structure at the interfaces between the pair of races considered and interlocking in the x -direction due to surface roughness.

6.2.4 Modeling

The last issue to be solved is the development of a simulation model for the relatively complex setup. The objective is to base the mechanical design on simulation data in order to meet the specifications given with the manufacturing of one prototype only. The requirement for the drive built at the Institut d'automatique was the possibility of actuation in both horizontal and vertical directions where gravity components must be overcome.

When the methodology, recalled in Appendix A.1, is applied to the inertial drive system, the bond graph shown in Figure 6.7 results. The serial ‘s’ junctions correspond to the rigid bodies of the system (overbraces in Figure 6.7) and the parallel ‘p’ junctions are related to the interfaces between them (underbraces in Figure 6.7).

The bond graph methodology is a very efficient technique for rapid modeling of complex systems because of the following advantages: (i) the systematic assignment of bond graph junctions to rigid bodies and interfaces accelerates modeling of the mechanical part of the setup considered; (ii) the electrical and the mechanical parts of the system are described with the same symbols; and (iii) the link between these two domains is straightforward with the concept of the transformer ‘TF’. Alternative approaches can lead to the equations of motion also, however the risk of introducing errors is considerable compared to a systematic methodology like bond graphs.

A voltage amplifier, denoted by EAS (effort amplifier with saturation), with gain g_e

transforms the low power signal u_{in} into the voltage u_a and the associated current i_p which flows across the piezo-crystal. For technical reasons the amplifier output current i_p is bounded by i_{\max} . The equivalent output resistance R is evaluated using the data sheet of the amplifier. Furthermore, the response time depends on the capacitance C of the piezo-crystal. In addition, it is proposed to use an empirical linear model $g_a v_p$ for the influence of the deformation velocity v_p of the piezo. Therefore, if the amplifier current is not saturated, the input circuit is described by

$$i_p = C \frac{du_p}{dt} + g_a v_p \quad (6.1)$$

$$u_a = g_e u_{in} = R i_p + u_p \quad (6.2)$$

and if the amplifier current is saturated and as long as $u_a \neq g_e u_{in}$

$$i_p = i_{\max} \operatorname{sign} u_{in} = C \frac{du_p}{dt} + g_a v_p \quad (6.3)$$

$$u_a = R i_{\max} \operatorname{sign} u_{in} + u_p \quad (6.4)$$

It is known that switching between these two models for saturated and non-saturated amplifier current can create simulation problems. However, an extended discussion of the relevance of, and possible solutions to, these difficulties is outside the scope of this chapter.

The mechanical part of the piezoactuator with the mobile mass m_p is subject to 6 forces: (i) the driving force $g_a u_p$ delivered by the piezo-effect; (ii) the linear, and (iii) the nonlinear contribution of the internal friction force $f_p(v_p, w_p)$; (iv) the elastic force of the piezo-crystal $k_a x_p$; (v) the force $k_b(x_p - x_s)$ transmitted through the elastic ball-flat-plane contact; and (vi) the force used for acceleration of the mass m_p . The model for the mechanical part of the piezoactuator is thus of order 3. The natural system states are piezo position x_p , velocity v_p and friction state w_p .

To get the state space model for the mechanical part of the piezo the rules proposed in Section A.2 can be applied: (i) the state derivatives are the velocities and accelerations of the rigid bodies, and (ii) the generalized force transmitted through an interface is expressed by a causal map, between the difference of velocities at the contact and the resulting force. This methodology leads to the system dynamics

$$\dot{x}_p = v_p \quad (6.5)$$

$$\dot{v}_p = \frac{1}{m_p} \left(g_a u_p - \sigma_{p2} v_p - \sigma_{p0} w_p - \sigma_{p1} \left(v_p - \frac{\sigma_{p0}}{F_{cp}} |v_p| w_p \right) - k_a x_p - k_b (x_p - x_s) \right) \quad (6.6)$$

$$\dot{w}_p = v_p - \frac{\sigma_{p0}}{F_{cp}} |v_p| w_p \quad (6.7)$$

where an empirical linear model for the driving force $g_a u_p$ delivered by the piezo-effect is used. A simplified form of the *LuGre* friction model is describing the internal friction in the piezoactuator. This approach has been chosen although multiple Coulomb models in parallel have been proposed previously [44] to describe the hysteresis effect observed for piezoactuators. The description of internal friction using the *LuGre* model is simply more

efficient for virtual prototyping because the integrated modeling minimizes the number of states and parameters and optimizes simulation speed by a continuous right-hand side to the equations of motion $\dot{x} = f(x, u)$. In addition, for simplicity it is assumed that the maximum static friction F_{sp} equals the Coulomb level F_{cp} .

For the ball–flat–plane contact, the Hertz model could be used, leading to a cubic relationship between the displacement and the force. However, owing to the preload force, which is assumed to be dominant, the linearized model is certainly sufficient.

On the slider, or small mass m_s , only two forces are acting besides the inertial force, namely the transmitted force $k_b(x_p - x_s)$ and the interfacial friction force $f_i(v_s - v_l, w_i)$. The corresponding dynamics are

$$\dot{x}_s = v_s \quad (6.8)$$

$$\dot{v}_s = \frac{1}{m_s} \left(-\sigma_{i2} (v_s - v_l) - \sigma_{i0} w_i - \sigma_{i1} \left(v_s - v_l - \frac{\sigma_{i0}}{F_{ci}} |v_s - v_l| w_i \right) + k_b (x_p - x_s) \right) \quad (6.9)$$

$$\dot{w}_i = v_s - v_l - \frac{\sigma_{i0}}{F_{ci}} |v_s - v_l| w_i \quad (6.10)$$

where x_s , v_s , and w_i denote slider position, slider velocity, and interfacial friction state, respectively. Although oil lubrication has been chosen for this interface, resulting in a certain difference between the breakaway force F_{si} and F_{ci} , a simplified *LuGre* model is used in Relation (6.10), but only for complexity reduction of the formulae presented herein.

The load mass m_l is driven by the interfacial friction force $f_i(v_s - v_l, w_i)$ and slowed down by the bearing friction $f_r(v_l, w_r)$

$$\dot{x}_l = v_l \quad (6.11)$$

$$\begin{aligned} \dot{v}_l &= \frac{1}{m_l} \left(-\sigma_{i2} v_l + \sigma_{i2} (v_s - v_l) + \sigma_{i0} w_i + \sigma_{i1} \left(v_s - v_l - \frac{\sigma_{i0}}{F_{ci}} |v_s - v_l| w_i \right) \right) + \\ &\quad + \frac{1}{m_l} \left(-\sigma_{i0} w_r - \sigma_{i2} \left(v_l - \frac{\sigma_{i0}}{F_{cl}} |v_l| w_r \right) \right) \end{aligned} \quad (6.12)$$

$$\dot{w}_r = v_l - \frac{\sigma_{i0}}{F_{cl}} |v_l| w_r \quad (6.13)$$

where x_l and v_l are load position and velocity, respectively, while w_r is the bearing friction state.

The model parameter identification is still an open problem. Nevertheless, it is possible to read a certain number of parameters from the data sheets, and to estimate certain additional values from physical properties (surface roughness, Young's modulus etc.) The remaining (unknown) parameters can be tuned interactively in order to match the simulation and experimental data. This leads to the following values: $C = 10^{-6}$ F, $g_e = 100$, $R = \frac{C}{2\pi 1500} \Omega$, $i_{max} = 0.5$ A, $g_a = 5.6$ NV⁻¹, $k_a = 560 \cdot 10^6$ N m⁻¹, $m_p = 0.05 + 7800 \cdot 0.025 \cdot \pi \frac{0.01^2}{4}$ kg, $\sigma_{p0} = 10^9$ N m⁻¹, $\sigma_{p1} = 10^5$ N s m⁻¹, $\sigma_{p2} = 0$, $F_{cp} = 500$ N, $k_b = 10^7$ N m⁻¹, $m_s = 7800 \cdot 0.02^3$ kg, $m_l = 1$ kg, $\sigma_{i0} = 0.2 \cdot 10^9$ N m⁻¹, $\sigma_{i1} = 2000$ N s m⁻¹, $\sigma_{i2} = 200$ N s m⁻¹, $F_{ci} = 10$ N, $\sigma_{i0} = 20 \times 10^6$ N m⁻¹, $\sigma_{i1} = 5000$ N s m⁻¹, $\sigma_{i2} = 500$ N s m⁻¹, $F_{cl} = 0.6$ N.

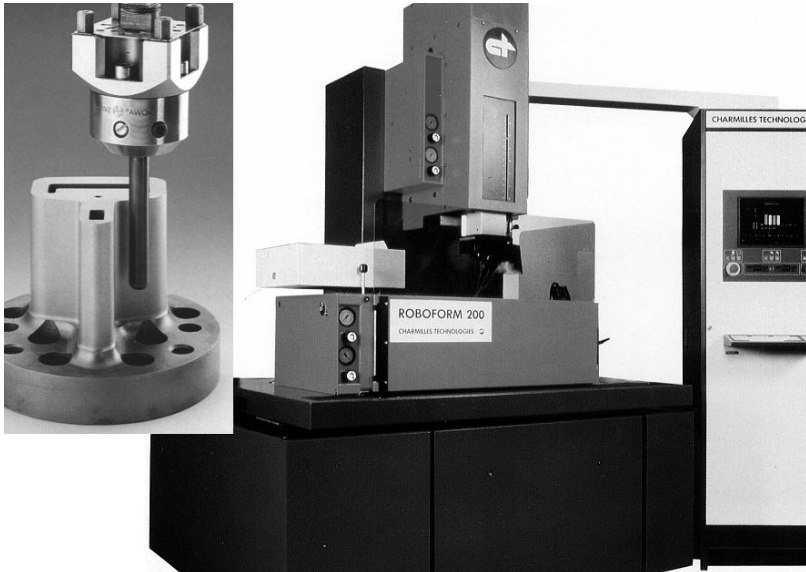


Figure 6.8: Electrical discharge machining.

6.3 Control of a Vertical Axis for EDM

The second application, presented herein, is the control of a vertical axis. This drive has been designed and manufactured by Charmilles Technologies S.A. (Meyrin, Switzerland) and is used for tool positioning in Electrical Discharge Machining (EDM). In order to provide the industrial context of this work, first a brief description of EDM is presented in Section 6.3.1. In Section 6.3.2 the vertical axis considered is described. Section 6.3.3 provides the parameter identification results. In Section 6.3.4 the tracking performance resulting from PI velocity control is illustrated. Section 6.3.5 presents the experimental data achieved with PID position control. In Section 6.3.6 the feedforward approaches are discussed. Section 6.3.7 illustrates the performance achieved with the input-output linearization approach. Finally, in Section 6.3.8 a catalogue of solutions to position control is presented, summarizing the previous results.

In the EDM process, metal is removed by generating high frequency sparks through a small gap filled with a dielectric fluid. This technique enables machining of complicated shapes in hard metals, including refractory alloys. The principal domains of application for EDM are production of molds (used for casting, injection or sintering) and dies (needed for extrusion, cutting or heading). There are two types of EDM machines: (i) the die sinker machine illustrated in Figure 6.8 and (ii) the wire machine.

For die sinkers, the cathode is usually the workpiece and the anode serves as the

shaping tool. Furthermore, any shape can be cut into the workpiece by matching that of the (negative image) electrode. Although undesirable, there is some erosion of the electrode (tool) which is called the wear and has to be minimized and controlled. The electrode does not come into physical contact with the workpiece and, therefore, does not exert any force (except via plasma pressure) upon it. This enables machining of extremely fine structures. Historically, heavy hydrocarbon liquids, such as cutting oils, have been used as dielectrics in die sinkers. Today's technological drawbacks for die sinking EDM is the corner wear and the contamination of the dielectric.

The wire machine cuts and shapes like a jigsaw. Here water is generally used as the dielectric. The moving cathode wire can cut at different angles into the anodic workpiece. Although the wire and the workpiece do not come into physical contact, the wire is shaped by the electrostatic and the hydrodynamic forces. This deformation leads to geometrical errors on the workpiece that are reduced by an appropriate axis control. The pulse times for wire machines are usually smaller than for die sinkers to allow high erosion rates on the workpiece. Some erosion of the moving cathodic wire is allowed, but high erosion results in wire breakage, the dominant practical and economic problem in wire EDM operation.

6.3.1 Brief Description of the EDM Process

A necessary condition for achieving good machining quality is to control the gap between the electrode (tool) and the workpiece. The sparking gap ranges from about 10 to 100 microns, respectively for finish and roughing. The control problem is therefore the regulation of the gap, that is measured only indirectly by processing some secondary signals since the actual gap is not measurable.

Some concepts of modern EDM control have been described in review [79]. Therein, a simplified linear model has been used to describe the dynamic behavior locally in the state space. Furthermore, an adaptive control scheme has been proposed to achieve enhanced machining performance.

The basic elements of EDM that have been subject to standards [96] are illustrated in Figure 6.9. The vertical displacement of the electrode (tool) is clearly indicated in the drawing that shows the workpiece and the electrode. In order to understand the operation of EDM, consider the experimental voltage and current signals of the plots to the right. Material removal is achieved by generating high frequency sparks through the gap between the electrode and the workpiece. By an appropriate choice of the polarity and other process parameters, the wear of the electrode is minimized, and material removal on the workpiece is optimized. A complete description of the process and the concepts of parameter selection is already available [36, 74].

The voltage and current profiles show a cycle of three phases, see Figure 6.9. First, a high voltage is applied during the delay time t_d . Then, the spark is formed and machining takes place during the period t_e with a machining current of I_{\max} and a voltage across the gap of U_{arc} . At the end of the cycle, the desired dielectric properties are recovered during the pause time t_o . In the case of the die sinkers manufactured by Charmilles Technologies S.A., the discharge current I_{\max} is controlled and the discharge voltage depends on the gap's properties.

A plasma channel grows during the on-time t_e . Unlike a gas, the surrounding dense

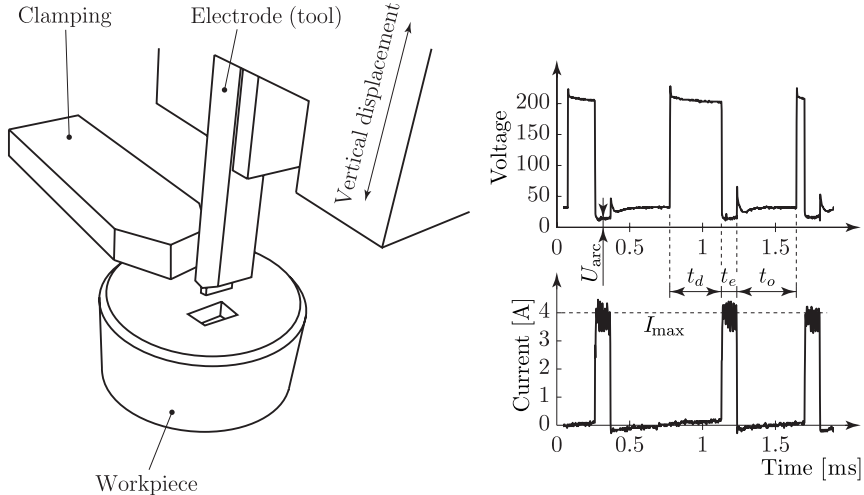


Figure 6.9: Operation of electrical discharge machining.

liquid dielectric restricts the plasma growth, concentrating the input energy $U_{\text{arc}} I_{\text{max}} t_e$ into a very small volume. Energy densities of up to 3 J/mm^3 result, causing local plasma temperatures to reach as high as $40'000 \text{ K}$. Dynamic plasma pressures rise to as much as 3 kbar owing mainly to inertial (density) effects. Viscosity effects are thought to be responsible for the plasma shape. During this on-time, the high-energy plasma melts both electrode (tool) and the workpiece by thermal conduction, but limited material vaporization occurs owing to the high plasma pressures. Furthermore, the anode first melts rapidly owing to the absorption of fast-moving, light electrons at the start of the pulse, but then begins to resolidify after a few microseconds. This is thought to be caused by the expansion of the plasma radius at the anode which causes a decrease in the local heat flux at the anode surface. Melting of the cathode is delayed in time by one or two orders of magnitude beyond that of the anode, owing to the lower mobility of the heavy, positive ions. Moreover, because the cathode is emitting electrons, the plasma radius at the cathode is also much smaller, thereby behaving like a point heat source. The temperature rise in the electrodes results from conduction and the Joule effect. It was found that Joule heating is negligible. This is because the current density decreases strongly with increasing depth beneath the electrode surface.

At the end of the on-time, a pause period t_o begins. During this period, a violent collapse of the plasma channel and the vapor bubble occurs, causing the superheated, molten liquid on the surface of both electrodes to explode into the liquid dielectric. While some of this material is carried away by the dielectric, the remainder of the melt in the cavities resolidifies into place, awaiting removal by a later spark.

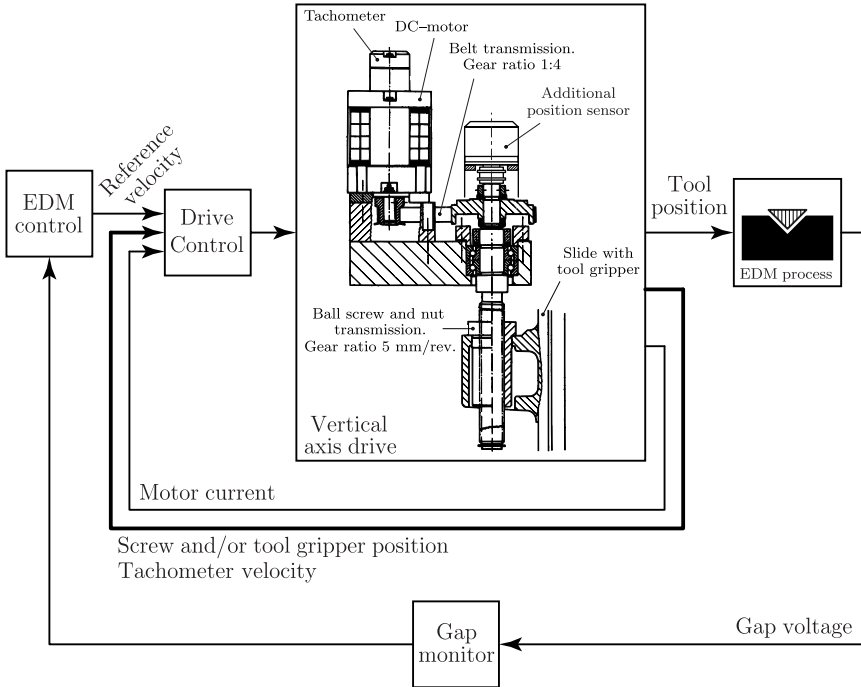


Figure 6.10: Scheme of a vertical axis drive and block diagram for EDM control.

6.3.2 Drive of the Vertical Axis and Overall Control Structure

The complete control structure of an EDM axis is illustrated in Figure 6.10 with a block diagram. The input to the EDM process is the vertical position of the tool. This position is combined with internal states of the EDM process to give the electrical gap width. A typical gap voltage signal for EDM is illustrated in Figure 6.9. The input of the EDM control is based upon an analysis of this gap voltage, realized by a complex electronic circuit, called the gap monitor. This monitoring and the EDM control are implemented in a multi-processor architecture that also includes some application specific integrated circuits (ASIC). One of the outputs of this machining controller is the reference velocity for the vertical axis.

The drive consists of a DC-motor, a belt transmission with gear ratio 1:4 and a ball screw and nut transmission with gear ratio 5 mm/revolution. All bearings are preloaded in order to eliminate backlash. Velocity is measured either directly with a tachometer or by means of numerical derivation of the signal from an optical position sensor. Two position sensors are available: an additional optical encoder of resolution 200'000 increments per

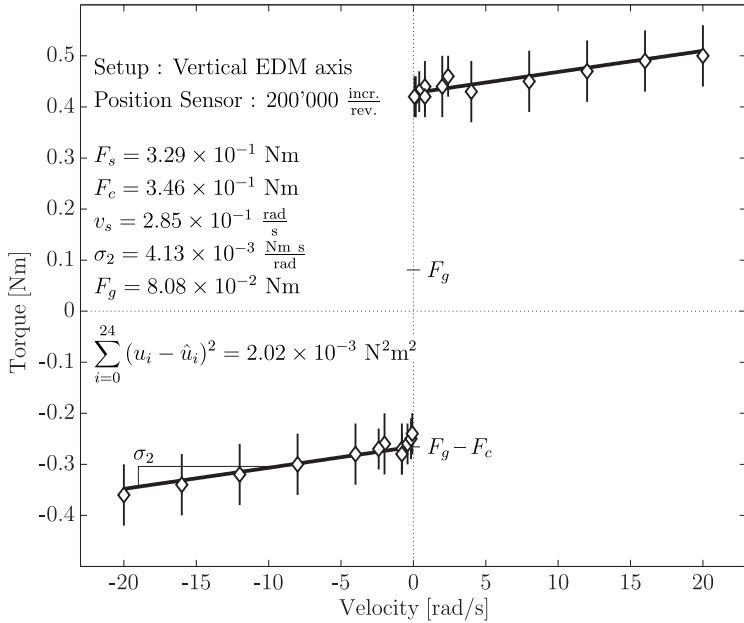


Figure 6.11: Identification: steady-state characteristics.

revolution, mounted on the ball screw, and the standard linear encoder of resolution $0.5 \mu\text{m}$ on the tool gripper. In order to make physical sense, all parameters and signals are reduced to motor variables in the following.

It is experimentally verified that the velocity measurement based on numerical derivation of the screw position has a better signal-to-noise ratio than the tachometer mounted on the motor axis. The linear position sensor on the tool gripper has only a resolution of 2'500 increments per motor revolution. All data presented in the following are based therefore on the additional optical encoder, mounted on the screw.

The drive control is implemented in a heterogeneous architecture, including an analog sliding mode motor current control loop, and a digital velocity and/or position control algorithm.

6.3.3 Identification Results

Steady State Characteristics Identification results for the steady state characteristics are shown in Figure 6.11. The 24 data points are obtained from tracking of a triangular position reference with various amplitudes and frequencies. Owing to perturbations in the drive, considerable uncertainties are present which are indicated by the error bars.

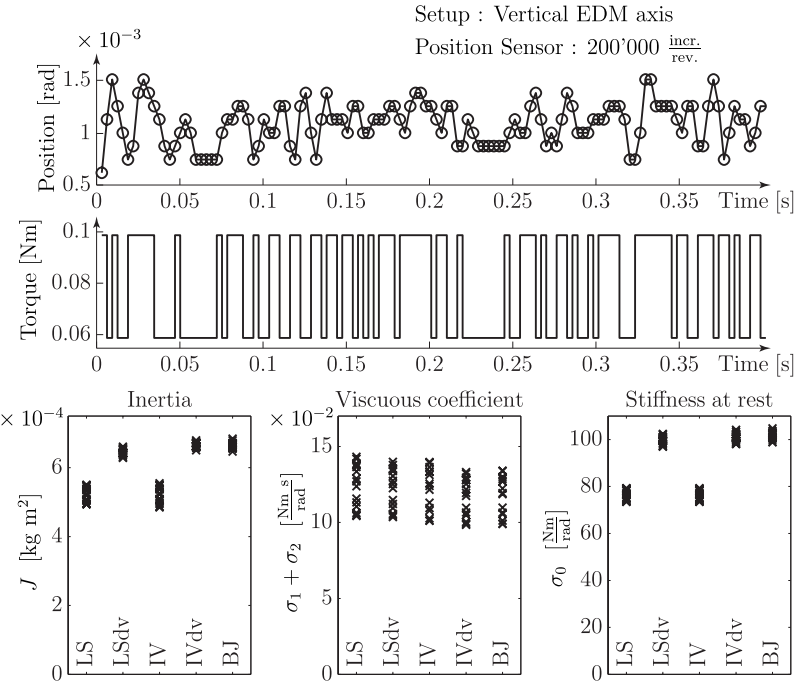


Figure 6.12: Identification: dynamics for presliding.

Parameter identification is based on the optimization of the quadratic torque prediction error. It results that the characteristics for positive and negative velocities, respectively, is quasi linear, *i.e.* $F_s \approx F_c$. Therefore, the parameter v_s identified makes only little sense. Furthermore, the influence of the offset term F_g appears clearly in Figure 6.11.

The comparison of the results for this and the following experiments is simplified in the summary that is provided in Table 6.2 at the end of this section.

Dynamics in the Presliding regime Identification results for the dynamics in the presliding regime are shown in Figure 6.12. On top, the temporal evolutions of torque input and position output are shown. It is easily verified that the system remains within presliding because the amplitude of the torque excitation is only $0.1F_s$. At the bottom, a comparison of different parametric identification methods is provided: least squares (LS), least squares using deviation variables (LSdv), instrumental variables (IV) after 20 iterations, instrumental variables using deviation variables (IVdv) after 20 iterations, and Box–Jenkins (BJ). Each cross indicates the result for a set of 3000 samples at a sampling period of 3.14 milliseconds. In order to provide an indication of reproducibility, 15 data

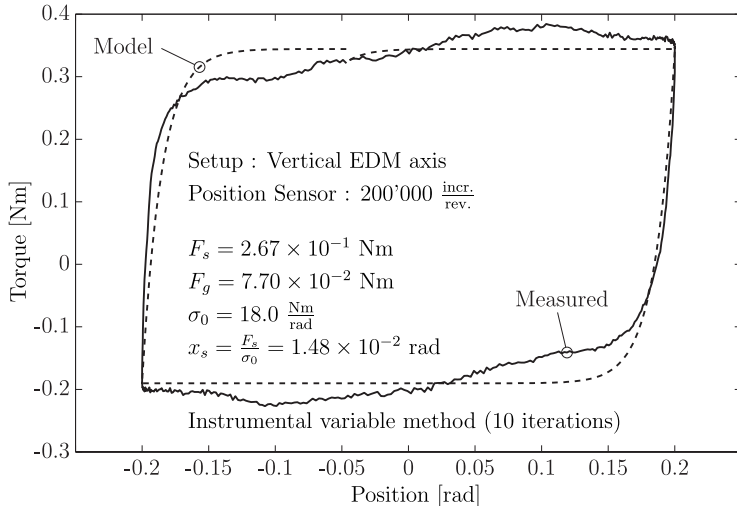


Figure 6.13: Identification: Dahl's curve.

sets are analyzed for each parameter and each method.

It is observed that the use of deviation variables is mandatory to obtain unbiased results for the least squares and the instrumental variable methods. For the Box–Jenkins method, the mean of the signals not need to be removed before entering the algorithm. The different estimations for inertia J and the stiffness at rest σ_0 remain within an interval of $\pm 10\%$ around the mean value. The results for the damping coefficient $\sigma_1 + \sigma_2$, however, are only reproducible within $\pm 20\%$. A comparison with previous identification results [3] shows that the reproducibility can be increased considerably by increasing the resolution of the position sensor.

Dahl's Curve Identification results for Dahl's curve are illustrated in Figure 6.13. It is observed that the estimates for the parameters F_g and F_s are in agreement with those achieved based on the steady-state characteristics experiment. However, the comparison of the plots for the model and those measured indicate certain differences. The parameter σ_0 that results from the iterative instrumental variable method, applied to estimate the parameters in (3.51), is underestimating reality. A comparison of the data in Table 6.2 also indicates that the value for σ_0 , measured in the presliding regime, is about 5 times larger than the value achieved from Dahl's curve.

Better results from Dahl's curve might be achieved if an alternative optimization criterion was selected. In addition, consistency of the results from the different identification experiments could be increased if the perturbations in the drive were reduced.

<i>Parameter [unit]</i>	<i>Steady state</i>	<i>Presliding IVdv</i>	<i>Dahl's curve</i>	<i>Adaptive feedforward</i>
J [kg m ²]	—	$6.66 \times 10^{-4} \pm 3\%$	—	—
F_g [Nm]	$8.08 \times 10^{-2} \pm 125\%$	—	$7.70 \times 10^{-2} \pm 70\%$	4.82×10^{-2}
F_s [Nm]	$3.29 \times 10^{-1} \pm 20\%$	—	$2.67 \times 10^{-1} \pm 20\%$	2.94×10^{-1}
F_c [Nm]	$3.46 \times 10^{-1} \pm 20\%$	—	—	
v_s [$\frac{\text{rad}}{\text{s}}$]	(2.85×10^{-1})	—	—	—
σ_0 [$\frac{\text{Nm}}{\text{rad}}$]	—	$1.01 \times 10^2 \pm 5\%$	(1.80×10^1)	3.13×10^1
σ_1 [$\frac{\text{Nm s}}{\text{rad}}$]		$1.12 \times 10^{-1} \pm 40\%$	—	—
σ_2 [$\frac{\text{Nm s}}{\text{rad}}$]	$4.13 \times 10^{-3} \pm 100\%$	—	—	—
$\sigma_1 + \sigma_2$ [$\frac{\text{Nm s}}{\text{rad}}$]	—	$1.17 \times 10^{-1} \pm 33\%$	—	—
x_s [rad]		$3.26 \times 10^{-3} \pm 26\%$	(1.48×10^{-2})	9.39×10^{-3}

Table 6.2: Numerical values for a vertical EDM axis (in parenthesis, the values with only limited confidence).

Summary A comparison of the results achieved from the different experiments is provided in Table 6.2. Because of the particular properties of the vertical axis drive, some values have only limited technical meaning, this is emphasized using parenthesis. For the other entries, the estimated reproducibility is indicated in percent around the mean value.

The considerable uncertainty for the results achieved with the steady-state characteristics is related to a (position dependent) torque ripple that is present in the drive. This additional perturbation is caused by: the collector of the DC-motor, machining errors in the ball bearings, and dust that inevitably enters the mechanism after a certain time of operation.

The evaluation of the values for the material damping σ_1 and the characteristic space constant x_s requires the two experiments steady-state characteristics and dynamics in presliding. Furthermore, excellent reproducibility is observed for the results achieved from the dynamics in presliding.

For completeness, the parameters identified with the adaptive feedforward algorithm, proposed in Section 5.1.4, are indicated in the last column. The experimental conditions are specified in Section 6.3.6. Because the adaptation gains are chosen such that the parameter values change only very slowly, the indication of confidence intervals is obsolete. Observe that the estimation of gravity F_g is in agreement with the results from the other experiments. Furthermore, note that the identification of the friction levels $F_c = F_s$ and of the stiffness at rest σ_0 leads to values that are in between those achieved from Dahl's curve and those obtained from the steady-state and presliding experiments. The estimated characteristic space constant x_s is of the same order of magnitude for all experiments.

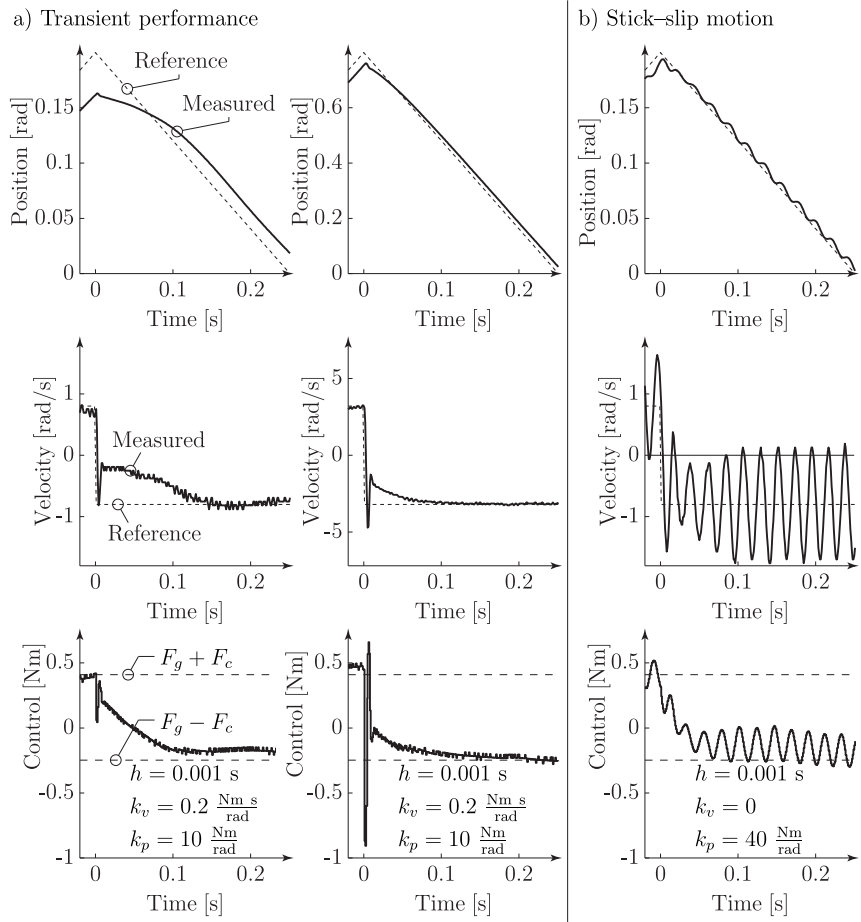


Figure 6.14: Performance of PI velocity control.

6.3.4 PI Velocity Control

Experimental data achieved for the PI velocity control (4.2) with the vertical EDM axis is shown in Figure 6.14. The control parameter values, for example the sampling period h for digital implementation, the velocity gain k_v and others, are indicated for completeness of the presentation. In (Plot a), the transient performance for reference velocity steps (with zero velocity crossing) is illustrated. The scaling of the axis is chosen in order to

allow comparison for a small and a large step.

The velocity gain k_v and the position gain k_p are selected in order to verify the stability requirements (4.22) and (4.23) with the mean values for the parameters, summarized in Table 6.2. Unfortunately, the control parameters that result from a worst case analysis cannot be implemented for technical reasons: the gains required are too large and the measurement noise saturates the control action. For this technological reason and owing to the limited industrial value of the theoretical developments in Section 4.1.5, checking of additional conditions for global asymptotic stability are left to the reader.

A detailed analysis of (Plot a) shows that the reference step induces a glitch in the applied torque. This control impulse is sufficient to drive the measured velocity very close to the reference velocity for a short period of time. Thereafter, the measured velocity settles to an intermediate value and regains its reference only after a time that is dependent on the step size. Therefore, the observed control performance that is achieved with PI velocity control can be acceptable for applications with generally large velocities. This conclusion expresses simply industrial experience, where model based friction compensation schemes are rarely implemented.

However, certain risks remain with PI velocity control. The undesirable phenomenon of stick-slip motion can appear even for drives with $F_s \approx F_c$ as illustrated in Figure 6.14b. It is observed that the system's nonlinearity is at the origin of continuous oscillations around the setpoint. Frequencies, ranging from 10^{-4} to 20 Hz, have been observed previously [59]; but, as illustrated in Figure 6.14b, also larger frequency can appear. Often, the phenomenon of stick-slip motion is amplified by the torque ripple that is generally present in drives.

A particular property of the vertical EDM axis considered is that $F_s \approx F_c$. Therefore, the oscillations, related to the stick-slip phenomenon, must include zero velocity transitions in order to excite the system's nonlinearities that are at the origin of the observed limit cycling.

6.3.5 PID Position Control

Various results for point-to-point tracking achieved with the PID control (4.67) are shown in Figure 6.15a-d. The control parameters are indicated in the plots. The Bode plots corresponding to the high velocity and the presliding regime are provided in Figure 6.16. Because the objective of this section is to illustrate only generic properties, it is left to the reader to check the global asymptotic stability conditions, provided in Theorem 4.2, for each case shown.

In order to reduce undesirable control saturation effects, the reference trajectory is low-pass filtered according to

$$H_{lp}(z) = \frac{(1 - \alpha) z}{z - \alpha} \quad (6.14)$$

with a settling time that should be compatible with the EDM application. For the experimental results shown in Figure 6.15 the filter parameter is $\alpha = 0.8$.

When the results for PID control are compared, it is observed that: (i) small bandwidth PID control leads to acceptable performance for large steps (Plot a) but to large settling

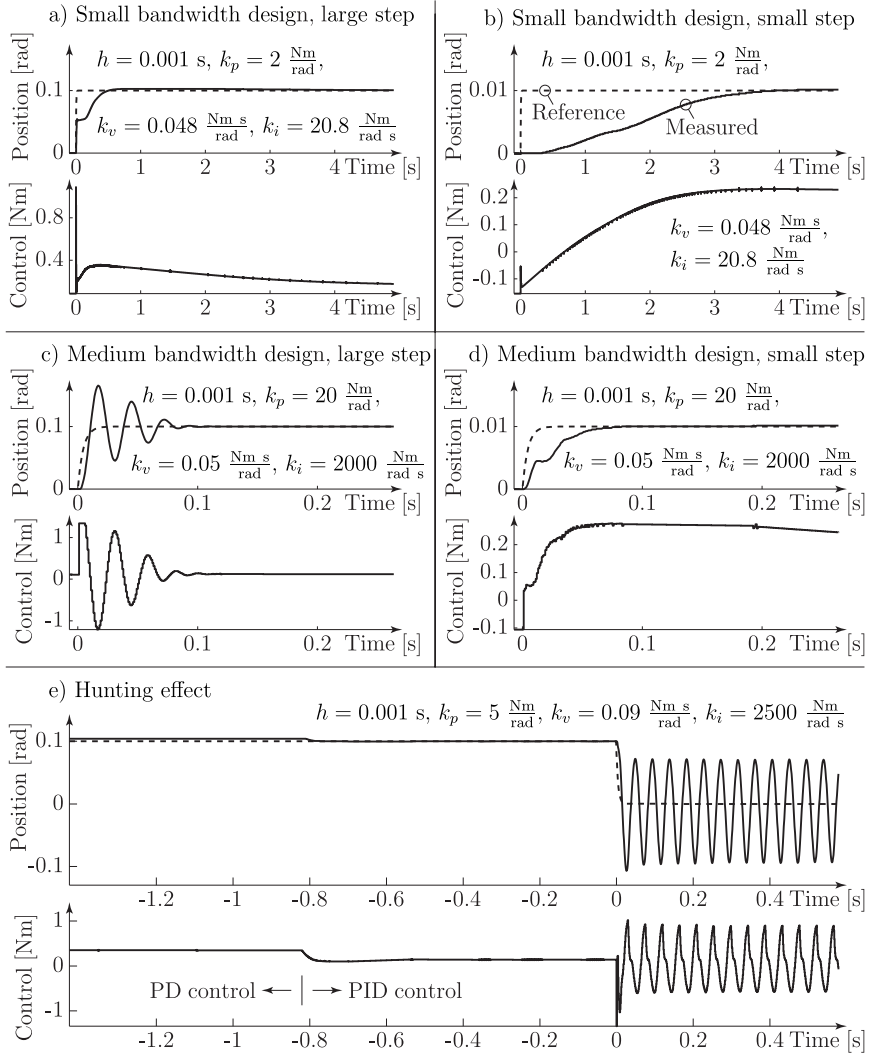


Figure 6.15: Performance of PID positioning.

times for very fine positioning (Plot b); and (ii) medium bandwidth PID control (Plots c–d) leads to comparable settling times for small and large displacements. Further increase

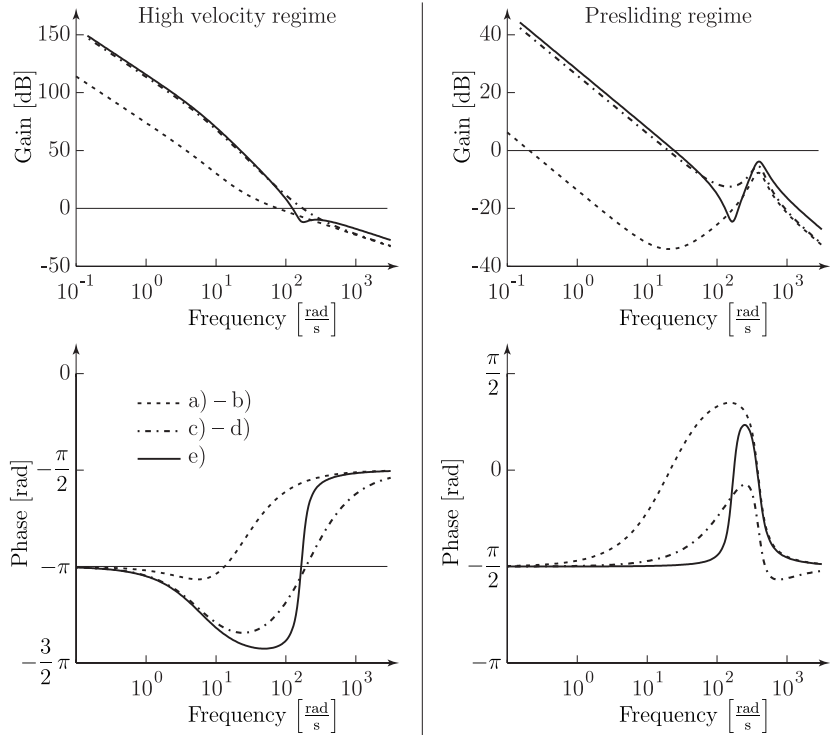


Figure 6.16: PID positioning: simplified synthesis with Bode plots.

of controller gains, *i.e.* large closed-loop bandwidth, requires enhanced sensing quality, which has not been available.

In addition, note that small and medium bandwidth controller design, based on the presliding regime only, leads almost inevitably to unstable solutions within the high velocity regime. This fact is displayed in (Plot c) by the badly damped oscillations, and in (Plot e) with the initiation of the hunting effect (stable limit cycle/oscillation around a constant reference, maintained by the system's nonlinearity). An explanation for this behavior can be obtained from an analysis of the corresponding Bode plots in Figure 6.16: the phase and gain margins for the high velocity regime of case (c) are almost zero, and even worse, the high velocity regime of case (e) is obviously unstable. The closed-loop nonlinear system is therefore not globally asymptotically stable, although, in the presliding regime, all controller configurations shown have excellent stability margins (infinite gain margin and a phase margin of at least $\frac{\pi}{2}$).

The relevance of an appropriate PID controller synthesis is illustrated in Figure 6.15e.

The objective is to exclude the oscillations observed in that experiment for time $t > 0$. This goal is achieved if the closed-loop regulation system (constant reference) is globally asymptotically stable.

At the beginning of the experiment shown in Figure 6.15e, only PD control has been applied, leading to an observable steady state error resulting from friction. About 0.8 s before the reference step, the integral action is switched on. Immediately, the positioning error moves towards zero, *i.e.* the closed-loop system is (locally) asymptotically stable. However, it is obvious that the reference step moves the system states out of the domain of attraction of the invariant set containing the reference position. Rapidly, a stable limit cycle is established, called the hunting effect. The frequency of about 25 Hz for these vibrations is relatively high compared to other experiments [27, 49], where only 0.04 and 0.3 Hz have been reported. This difference in observed frequency can presumably be explained by the fact that $F_s \approx F_c$ for the vertical EDM axis considered.

6.3.6 Feedforward Friction Compensation

The interest for model based friction compensation results, for example, from an analysis of the tracking performance achieved for a sinusoid reference of amplitude 0.2 rad $\approx 20x_s$ and frequency 1 Hz. The results for PD, PID, and PID with *LuGre* feedforward control are shown in Figure 6.17 with plots for position, positioning error and motor torque. The control parameters are summarized in Table 6.3.

The identification procedure completed in Section 6.3.3 required about one day for preparing the experiments and analyzing the data. This is relatively time consuming, and, as a more efficient approach, it is proposed to apply directly the adaptive control scheme (5.14)–(5.16) to the simple feedforward algorithm (5.2)–(5.3), (5.6). The parameter adaptation with relatively small gains α_g , α_0 and α_c leads, after about 5 minutes, to the numerical values indicated in Table 6.2.

When tracking is achieved with PD control only, see Figure 6.17a, it is observed that a considerable position error (about 7 mrad) is present. Performances are improved, as illustrated in (Plot b), already to a quite acceptable level by simply adding integral action. However the quadrature glitch, observed in the error plot after velocity reversals at time $t = 0.25$ and 0.75 s, has still an amplitude of 2 mrad. Finally, excellent tracking is achieved by the PID+*LuGre*-feedforward control algorithm which reduces the quadrature glitch to about 1 mrad, see (Plot c). To illustrate the relevance of the approach, the feedforward control signal is shown in the torque plot: feedforward control matches almost perfectly overall control action and the PID controller concentrates on perturbation rejection.

Furthermore, the measurement noise level is indicated in the error plots by the value for one sensor increment $\Delta = \frac{2\pi}{50'000} = 1.25 \times 10^{-4}$ rad. The quadrature glitch for PID control is therefore 16 increments, whilst the maximum position error resulting for control with the additional *LuGre* model based feedforward is only 8 encoder increments.

Real-time results comparing the performance achieved with feedforward based on the two friction models have been presented recently [1]. However, the results achieved with the KFM based feedforward compensation are not shown here because of the small interest for the application considered.

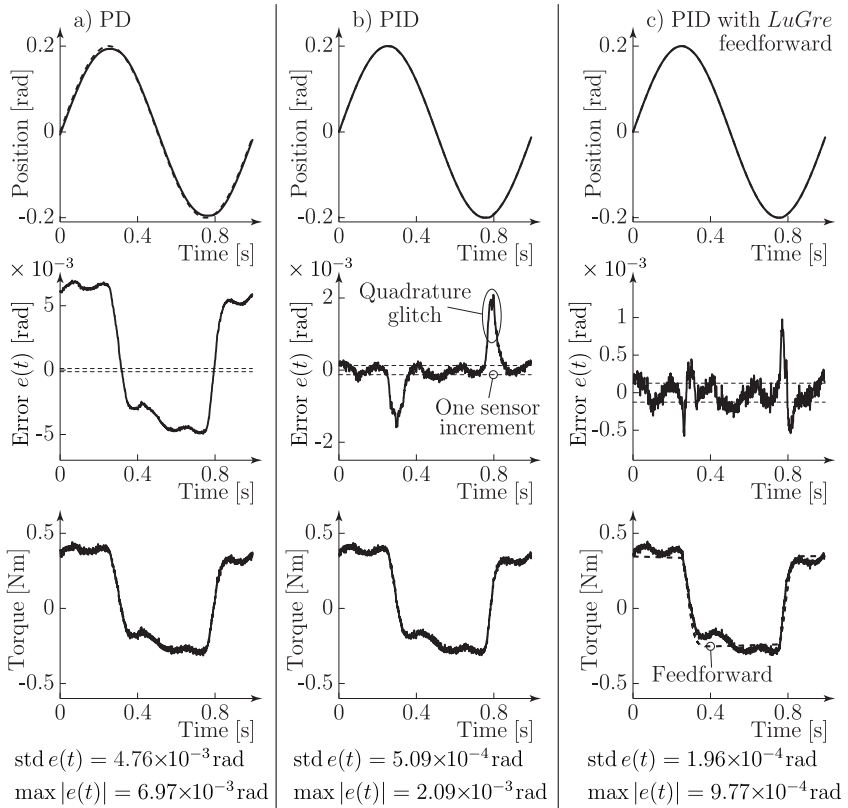


Figure 6.17: Sinus tracking: PD, PID, and PID with *LuGre* feedforward.

6.3.7 Input–Output Linearization by State Feedback

Performances achieved by different input–output linearization techniques are illustrated in Figure 6.18 with the tracking behaviour for the same sinusoid reference signal as used in the previous section. This allows comparison of maximal positioning errors $\max |e(t)|$ and standard deviations $\text{std } e(t)$.

Figure 6.18a shows the performance achieved: with the friction state observer (5.17), proposed by the Lund–Grenoble group [27], the input–output linearization (5.39), and a PID control. Internal stability problems that arise from the digital implementation of the friction state observer have been solved using a similar approach to the feedforward algorithm (5.8). Implementation details can be found in the C-code in Appendix B.

Although no stability proofs are available when integral action is chosen, this option

	PD	PID	<i>LuGre</i> feedforward	<i>LuGre</i> feedback	Luenberger observer	KFM feedback
<i>h</i> s	1.00×10^{-3}					
k_p $\frac{\text{Nm}}{\text{rad}}$	6.00×10^1	6.00×10^1	6.00×10^1	6.00×10^1	2.00×10^2	6.00×10^1
k_d $\frac{\text{Nm s}}{\text{rad}}$	1.50×10^{-1}	1.50×10^{-1}	1.50×10^{-1}	1.50×10^{-1}	—	1.50×10^{-1}
k_i $\frac{\text{Nm}}{\text{rad s}}$	—	6.00×10^3	6.00×10^3	6.00×10^3	2.00×10^4	—
\hat{F}_g Nm	—	—	4.82×10^{-2}	4.82×10^{-2}	4.82×10^{-2}	4.82×10^{-2}
\hat{F}_s Nm	—	—	2.94×10^{-1}	2.94×10^{-1}	2.94×10^{-1}	2.94×10^{-1}
$\hat{\sigma}_0$ $\frac{\text{Nm}}{\text{rad}}$	—	—	3.16×10^1	3.16×10^1	3.16×10^1	—
k_v $\frac{\text{Nm s}}{\text{rad}}$	—	—	—	—	5.00×10^{-1}	—
α_g $\frac{1}{\text{s}}$	—	—	1.00×10^{-2}	—	—	—
α_0	—	—	1.00×10^2	—	—	—
α_c $\frac{1}{\text{s}}$	—	—	1.00×10^{-1}	—	—	—
\hat{J} kgm ²	—	—	6.66×10^{-4}			
$\hat{\sigma}_1$ $\frac{\text{Nm s}}{\text{rad}}$	—	—	1.12×10^{-1}			
$\hat{\sigma}_2$ $\frac{\text{Nm s}}{\text{rad}}$	—	—	4.13×10^{-3}			

Table 6.3: Parameters for real-time experiments (position control).

is selected because experience has shown that the tracking performance can be increased. However, note that a certain risk exists of creating an unstable control loop by the addition of the integral action. The positioning error signal with this control approach contains a quadrature glitch of 1.4 mrad that is about 40% larger than for the feedforward solution. In addition, observe that the friction compensation signal ‘model based control’ is noisy, which is not the case for the feedforward solution. These observations lead to the conclusion that the robust, adaptive feedforward solution is preferred to the feedback approach.

In the next phase, the Luenberger-like observer has been implemented. The corresponding results are shown in Figure 6.18b. Because velocity is estimated by the state observer, the resulting relatively smooth signal (compared to a simple numeric derivative) can be used for feedback in order to increase damping. The Luenberger-like observer based algorithm has given very promising results for the tracking of reference steps [2], however, in the context of sinus reference tracking and with a sampling period of $h = 1$ ms for digital implementation, the performance is very comparable to the other approaches (feedforward and the *LuGre* observer). The increased complexity of the algorithm implemented, the difficult tuning procedure, and the relatively low robustness versus parameter uncertainties (compared to the feedforward solution) are the main disadvantages of the

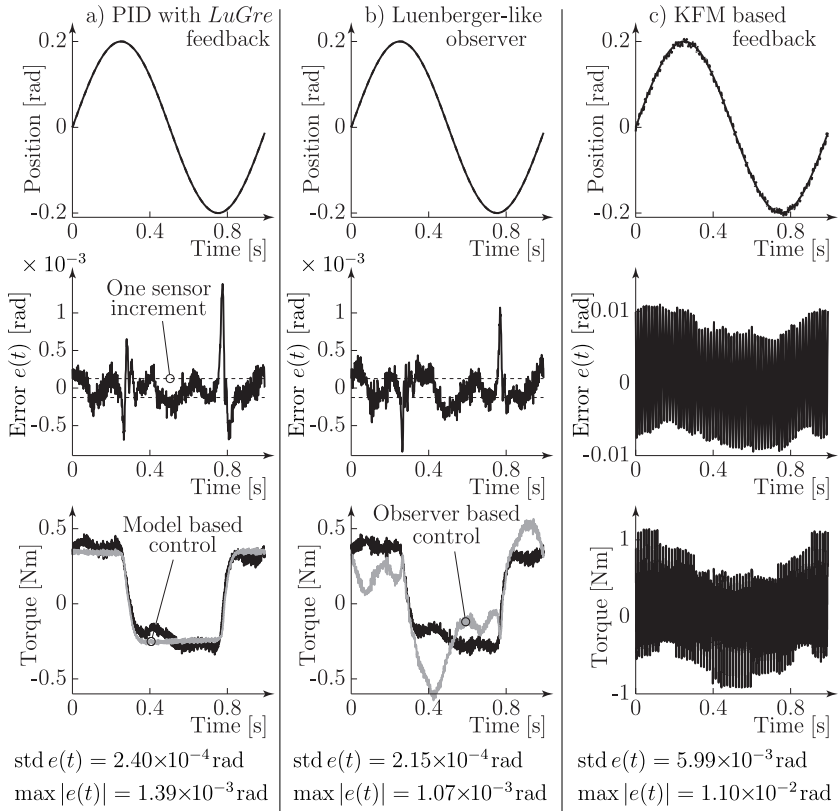


Figure 6.18: Sinus tracking: input–output linearization.

Luenberger-like observer based compensation approach.

Finally, the tracking performance for the KFM based feedback friction compensation is shown in (Plot c). Persistent oscillations are observed for this particular benchmark test because the reference velocity is never high enough to enter the region where exponential stability is achieved. It is therefore obvious why the KFM based compensation algorithm has only limited success in real applications.

6.3.8 Catalogue of solutions

The catalogue of solutions for position control is shown in Table 6.4. It is obvious that the robust PD and PID algorithms require a small identification effort and that robust

	PD	PID	<i>LuGre</i> feedforward	Adaptive <i>LuGre</i> feedforward	<i>LuGre</i> feedback	Luenberger observer	KFM feedback
Identification effort	😊	😊	😢	😊	😢	😢	😊
Robust stability	😊	😊	😊	?	?	?	😢
Step response	😢	😊	😊	😊	😊	😊	😢
Sinus tracking	😢	😊	😊	😊	😊	😊	😢

Table 6.4: Catalogue of solutions for position control.

stability is easily achieved. The drawback is that the tracking performance resulting from PD or PID control, is limited.

Model based compensation techniques require a considerable identification effort, unless an adaptive scheme or the simple KFM is used. Robust stability is easy to prove for feedforward solutions, whilst no proofs are available for the complex feedback algorithms, and worse still, it is known that the KFM based algorithm often leads to undesirable vibrations. Excellent sinus tracking performance is achieved with the *LuGre* model based algorithms. However, due to the fact that the problem of actuator saturation has not yet been solved, only medium performance is achieved for step responses.

From these considerations, it is concluded that the ‘best’ solution for drive control in industrial applications is formed by two phases: (i) the adaptation of the control parameters for a suitable benchmark reference during an initialization/auto-tuning phase, followed by (ii) a fixed parameter *LuGre* model based feedforward compensation during normal machine operation. The parameters for auto-tuning can be fixed once by a control engineer for a whole family of products. Thereafter, during the whole life-cycle of the machine, operators can independently update the controller parameters by calling up the initialization procedure.

Chapter 7

Conclusions

THE results presented in this work include modeling, identification and control of drives with friction. The topics discussed are presented from different viewpoints: physics, mechanics, nonlinear systems analysis and digital control. Therefore, it aims to be a user's manual for engineers, faced with the problems encountered during control synthesis for drives with friction. Below, the relevance of the methodologies proposed and potential directions for further research are summarized.

7.1 Relevance of the Methodologies Proposed

The results presented previously can be classified into two categories: (i) modeling of the drive based on technical drawings and experimental data, and (ii) synthesis of the controller. These two phases have been illustrated in Figure 1.2 in order to provide a context for the postulations announced in Chapter 1 and discussed in the following.

- Three experiments are necessary to identify all model parameters
- The *LuGre* model must be considered for applications with small displacements
- The stability analysis is simplified with a passivity based approach
- Feedforward is the best solution for input-output linearization
- An easy-to-use auto-tuning procedure is available with the adaptive feedforward control algorithm.

During the discussion of the issues and solutions that appear in these two steps (modeling and controller synthesis), several new results have been presented. From three experiments it is possible to estimate all of the parameters of a simple drive with friction. This achievement is indispensable to the usefulness of all further discussion.

Modeling for control aims to provide the adequate model complexity (number of states and parameters) for a given application. Therefore, possible model simplifications must be discussed. In certain particular cases, a rigorous model order reduction has been achieved with the singular perturbation theory: modern complex models are required in all situations with 'small' displacements. Applying the concepts presented, it is now

possible to decide whether a given application requires the use of the complex *LuGre* model, or whether the simple KFM describes the dominant phenomena with sufficient precision. The governing parameter for this decision is the characteristic displacement $x_s = \frac{F_s}{\sigma_0}$ of the drive.

To achieve excellent tracking performance, a high loop-gain approach, which is extremely sensitive to measurement noise, can be applied. An alternative methodology is an input-output linearization that can be achieved: either by feedback, based on an estimation of the actual states; or by feedforward, based on an appropriately generated control action that compensates the friction force that would appear in the case of perfect tracking. For industrial applications with important security demands, simple solutions based on a PID control loop are preferred. In practice, model based feedback compensation approaches will probably never be important for high precision positioning applications because of the numerous drawbacks and dangers observed previously: difficulties in guaranteeing stability, chattering observed in the case of parameter mismatch *etc.* Feedforward model based friction compensation techniques, however, present a considerable interest in practice because of the small additional computing power required and the simple and safe tuning procedure.

Proofs for robust closed-loop stability have been achieved with a passivity based approach. This methodology allows a modular analysis because the input-output properties of appropriately chosen subsystems can be used to evaluate the behavior of the overall system. The conditions for asymptotic stability of the closed-loop are expressed with relations in the control parameter space, for example $k_v > \dots$. In addition, it is possible to estimate the robustness of the tracking performance with the concept of induced norms of maps in the signal space.

Finally, a catalogue of solutions for the control of drives with friction has been presented. It shows that PID control, enhanced by adaptive feedforward, is the most interesting algorithm because the identification effort is reduced, and stability of the closed-loop results if the adaptation gains are sufficiently small. In addition, acceptable step response and excellent sinus tracking performance is achieved. The problem of control of simple drives with friction is therefore solved, and it is claimed that any further improvement of tracking performance will be related to a considerable technological investment (better sensors and motors) and scientific effort (more complex models for friction). The C-Code for all algorithms discussed is listed in Appendix B for completeness, and for eventual testing for other applications.

The objective of this work has been achieved: a generic solution is provided for the synthesis of control for drives with friction. This has been accomplished through the discussion of a large variety of aspects: description of the physical phenomena, integrated friction modeling and parameter identification, and methodologies for friction force compensation.

7.2 Further Research Directions

In this work, the modeling of complex drives has been briefly discussed. However, solutions to the problem of model parameter identification are not presented for these drives.

The following situations require further investigation. For drives with several friction interfaces, for example the inertial drive setup, it is probably necessary to increase the number of sensors in order to identify all of the parameters of the system. The same problem of observability arises for drives with flexible transmission elements where one output is presumably sufficient also.

To extend the results on controller synthesis, the adaptive control architectures should be analyzed in more detail. A rigorous stability analysis of the indirect adaptation law proposed, that has been skipped herein, could, for example, be based on a singular perturbation analysis.

In addition, new algorithms could take into account model enhancements that describe the reversal point memory and other phenomena. Although these new controllers will be based on a better description of physical reality, it is not certain, however, that they will also provide better control performance than the *LuGre* model based algorithms in terms of performance and stability. Therefore, it would be interesting to know the relevance of the modeling mismatch accepted with the *LuGre* model in order to provide a valuable basis for deciding whether the *LuGre* model really needs to be extended or whether the results presented in this work are sufficient to achieve the performance specified for the application considered.

Appendix A

Modeling of Complex Systems

Modeling and simulation are central to the design of control systems, since for complex, large-scale, nonlinear industrial plants, the analytical design approaches known do not apply, or require an unacceptable effort. Several software packages, see Table A.1, for object oriented modeling have been proposed therefore in order to help mechanical design engineers.

Nevertheless, severe problems remain for a correct description of multi-body mechanisms with friction, when the KFM is used. The typical computer formulation of the KFM is based on switching between particular regions of operation. It can be observed that the transitions between these domains are difficult, mainly when different switching events take place simultaneously [73]. Note that the unique existence of exactly one solution for the initial value problem is not even shown mathematically for these situations, which explains the difficulties encountered.

Fortunately, the use of the dynamic *LuGre* model introduces a normalization that makes simulation straightforward. Below, it is shown that even for complex systems the model can be transformed into a set of ordinary differential equations if the *LuGre* model is used, instead of a system of difficult differential algebraic equations resulting from the application of the KFM.

A.1 Bond Graphs for Mechanical Systems

The main problem arising when modeling large systems is that the control engineer is easily restricted to three fundamental concepts [28]: (i) state-space models form the basis of physics, (ii) signals capture physics, and (iii) causality forms the basis of physics. In [28], energy or power flow methods are suggested to solve the problem of modeling complex systems in an efficient way.

If all forces in the system are conservative, *i.e.* for a system without dissipation, it is possible to use Lagrangian or Hamiltonian equations to model the mechanical device. This approach, however, which is based on the total energy of the system, does not allow use of the energy of subsystems. Therefore, no modular analysis is possible which presents a considerable drawback.

To overcome these deficiencies, the bond graph representation [43] was developed in the early 1960s. The fundamental concept that is used in bond graphs is the power

<p><i>Mechanical Dynamics, Inc. pioneered the field of mechanical system simulation, and has remained focused on this technology since its founding in 1977. The ADAMS software is a widely-used mechanical system simulation tool.</i></p> <p><i>Web-address http://www.adams.com/</i></p>
<p><i>Knowledge Revolution was formed in 1989 to address the emerging market for the simulation of mechanical systems. Knowledge Revolution is now one of the leading unit provider of software that allows users to model and animate mechanical systems. The company's principle product Working Model, provides an environment for design, analysis, and distribution of virtual mechanical prototypes. The company's motion simulation technology is also used in Interactive Physics, which is used in educational physics software.</i></p> <p><i>Web-address http://www.krev.com/</i></p>
<p><i>Dynasim was founded in 1992 by H. Elmquist. Dynasim's mission is to develop the software tools that industry needs for solving demanding modeling and simulation problems. The emphasis is on handling large, multi-domain systems efficiently. The company's product Dymola is a general purpose modeling language. It is suitable for modeling mechanical, electrical, thermo-dynamical and chemical systems, etc. Bond graph methodology can be used.</i></p> <p><i>Web-address http://www.dynasim.se/</i></p>

Table A.1: Software packages for object oriented modeling.

conservation law. The energy flow from one point of the system to another is denoted in Figure A.1c by a harpoon. The power transferred is the product of the two adjunct variables, called the effort and the flow in bond graph terminology. In the context of mechanical systems, the force is generally assigned to the effort, and the relative velocity represents the flow variable.

The notations and properties of bond graphs are illustrated in Figure A.1 by the example of two masses m_1 and m_2 , placed one above the other. A force u is applied to mass 1, and the two masses move at speeds v_1 and v_2 . The bond graph, Plot (c), is formed of two types of junctions: at 's' or serial junctions, all flow variables are equal and the effort variables sum to zero; at 'p' or parallel junctions, the flow variables sum to zero and the effort variables are all equal. For a mechanical setup, the serial 's' junctions correspond to the rigid bodies of the system and the parallel 'p' junctions are related to the interfaces between them. For systems with distributed masses, it is possible to use the concept of fields of masses which, however, is outside the scope of this summary.

For bond graph modeling of systems with friction, two particular elements are required. The one-port 'R' or resistor represents viscous friction with the effort $f_v = \sigma_2 v$ proportional to the flow. The second one-port 'F' represents the nonlinear part of the friction force that is described by the KFM or the *LuGre* model.

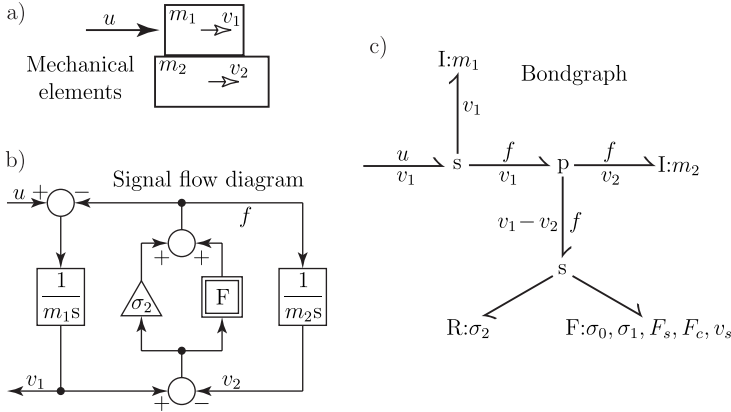


Figure A.1: Graphical representations of a drive with friction.

A.2 From Bond Graphs to Ordinary Differential Equations

The bond graph representation of a mechanical system is too abstract to be handled directly by commercial simulation software. Therefore, it is necessary to transform the bond graph representation into differential algebraic equations. A procedure for systematic model transformation is available [43]. This approach is well suited to computer-aided modeling environments. It is observed that, after elimination of intermediate variables, four groups of equations remain: state derivatives, non-states, internal system outputs, and system outputs

$$\dot{x} = f_x(x, u, v, \dot{z}) \quad (\text{A.1})$$

$$z = f_z(x, u, v, \dot{z}) \quad (\text{A.2})$$

$$w = 0 = f_w(x, u, v, \dot{z}) \quad (\text{A.3})$$

$$y = f_y(x, u, v, \dot{z}) \quad (\text{A.4})$$

where x is the vector of state variables associated with inertial and spring elements with integral causality; z denotes the vector of non-state variables associated with inertial and spring elements with derivative causality (\dot{z} contains the corresponding derivatives); v and w are the vectors of additional (internal) inputs and outputs that are required to express constraints in the system; and finally u and y denote the system's inputs and outputs.

For an efficient simulation, it is crucial to describe the system by a set of ordinary differential equations, *i.e.* only with relations of type (A.1) and (A.4). Thus it is necessary to eliminate nonstate equations (A.2) by an appropriate assignment of causality, and to solve all algebraic constraints (A.3) analytically.

For drives with friction, for example the one illustrated in Figure A.1, the following rules lead to the solution desired: (i) the state derivatives (A.1) are the velocities and accelerations of the rigid bodies, and (ii) the generalized force transmitted through an interface is expressed by a causal map, between the difference of velocities at this contact and the resulting force. These two rules lead to the signal flow diagram, shown in Figure A.1b. If the *LuGre* model is used in the friction block ‘F’ then it is straightforward to represent the bond graph shown in Figure A.1c by a set of ordinary differential equations, *i.e.* only with relations for state derivatives and system outputs.

Appendix B

C-Code Program Listing: Real-Time Task

THE real-time experiments have been achieved within a framework for fast real-time applications [85] which has been developed for the MacOS version of LabVIEW. Measured positions are sampled by a hardware clock at precisely defined time instants. The control algorithm is called afterwards through a high priority system interrupt.

```
/*-----*/
/*
/* Project : PhD Thesis "Friction Modeling, Identification and Compensation"
/* Task :    Real-Time Control of a Drive with Friction
/* Author : Friedhelm Altpeter, Institut d'automatique, EPFL
/*
/*-----*/
/*-----*/
#include <fp.h>
#include <Types.h>

#include "RT_DLL.h"
#include "fungen.h"
#include "read_position.h"

#define MAXOUTPUT (10.0)
#define TWOPID (6.28318530718)
#define DAOFFSET (1.8e-3)
#define PRECISION (1e-3)

/*---- number of states and parameters -----*/
#define NB_STATES (13)
#define NB_PARAMS (36)
```

```

/*---- control parameter declaration -----*/
#define waveform      (p[0])    /* signal generator */
#define amplitude     (p[1])
#define frequency     (p[2])
#define offset        (p[3])
#define masterreset   (p[4])    /* sensor resolution */
#define D_on_off      (p[5])
#define Td             (p[6])    /* derivative time constant */
#define I_on_off       (p[7])
#define Ti             (p[8])    /* integral time constant */
#define kp             (p[9])    /* proportionnal gain */
#define ARW_Level     (p[10])   /* anti-reset windup level */
#define ARW_on_off    (p[11])
#define load_var_flag (p[12])   /* 0: motor variables, 1: load variables */
#define BO_or_BF      (p[13])   /* 0: open-loop, 1: closed-loop control */
#define Km             (p[14])   /* torque constant */
#define ResScrew       (p[15])   /* resolution screw sensor [increments/revolution] */
#define ResLin         (p[16])   /* resolution linear sensor [m/increment] */
#define comp_select    (p[17])   /* compensation selector */
#define Inertia        (p[18])   /* inertia [kg m^2] */
#define F_c            (p[19])   /* Coulomb level [Nm] */
#define F_s            (p[20])   /* break away torque [Nm] */
#define F_g            (p[21])   /* gravity contribution [Nm] */
#define v_s            (p[22])   /* Stribeck velocity [rad/s] */
#define s0              (p[23])   /* stiffness at rest [Nm / rad] */
#define s1              (p[24])   /* viscous friction [Nm s/rad] */
#define s2              (p[25])   /* bristle viscous friction [Nm s/rad] */
#define alpha_g         (p[26])   /* adaptation gains */
#define alpha_0         (p[27])
#define alpha_c         (p[28])
#define Adapt_on_off   (p[29])
#define h               (p[30])
#define alpha           (p[31])   /* reference filter parameter */
#define klugre          (p[32])   /* estimator gain proposed by LuGre */
#define l_1             (p[33])   /* Luenberger observer gains */
#define l_2             (p[34])
#define k_hatdotq      (p[35])   /* velocity feedback based on Luenberger velocity
estimation */

/*---- controller state declaration -----*/
#define phase          (x[0])    /* phase of signal generator */
#define randval         (x[1])    /* real random value */
#define ref_1           (x[2])    /* last reference and measure values */
#define ref_2           (x[3])
#define mes_1           (x[4])
#define mes_2           (x[5])
#define u_i             (x[6])    /* integral contribution to control */
#define hatz            (x[7])    /* friction state estimation */
#define xi_1             (x[8])   /* Luenberger observer states */
#define xi_2             (x[9])
#define hatF_g          (x[10])   /* friction parameter estimations */
#define hats0            (x[11])
#define hatF_c          (x[12])

```

```

/*--- declaration of switch between control algorithms -----*/
#define NO_MODEL_BASED 0
#define LUGRE_FF 1
#define LUGRE_FB_LIN 2
#define KFM_FB_LIN 3
#define LUENBERGER 4

/*--- Gaussian model for steady state characteristics -----*/
#define g(v)          ( (F_c + (F_s-F_c)*exp(-v*v/(v_s*v_s))) / s0 )

/*--- declaration of state and parameter vector -----*/
double x[NB_STATES];
double p[NB_PARAMS];

/*--- computer simulation adapted sign function -----*/
double signf(double x);
double signf(double x) {
    if (x > PRECISION) return 1.0;
    else if (x < -PRECISION) return -1.0;
    else return 0.0;
}

/*--- mathematical sign function -----*/
double sign(double u);
double sign(double u) {
    if (u>0.0)
        return(1.0);
    else if (u<0.0)
        return(-1.0);
    else
        return(0.0);
}

/*--- saturation function -----*/
double sat(double u, double lim);
double sat(double u, double lim) {
    if (u > lim)
        return(lim);
    else if (u < -lim)
        return(-lim);
    else
        return(u);
}

```

```

/*---- control algorithm (called at every sampling period) -----
long UserFunction(void);
long UserFunction(void){

    int cc;

    /***** *****/
    /* definition of internal signals */
    /***** *****/

    double FunGenOut = 0.0;      /* output of the function generator */
    double u_pid = 0.0;          /* PID control action */
    double u_c = 0.0;            /* compensator control action */
    double Control = 0.0;        /* total control action */
    double q, dotq, ddotq;       /* measure position, velocity and acceleration */
    double r, dtr, ddotr;        /* reference position, velocity and acceleration */
    double hatdotq, hatdotz;     /* estimations of velocity, friction state and friction
                                  state derivative */

    /***** *****/
    /* retrieve the control parameters */
    /***** *****/

    for (cc=0; cc<NB_PARAMS; cc++)
        Get(0,cc,p+cc);

    if (masterreset)
        for (cc=0; cc<NB_STATES; cc++)
            x[cc] = 0.0;

    if (Adapt_on_off) {
        F_g = hatF_g;
        s0 = hats0;
        F_c = hatF_c;
        F_s = hatF_c;
    } else {
        hatF_g = F_g;
        hats0 = s0;
        hatF_c = F_c;
    }

    /***** *****/
    /* retrieve the actual position of the system */
    /***** *****/

    if (load_var_flag)
        /* pion2m in load variables */
        q = ((5e-3) / ResScrew) * 0.25 * ReadPositionInIncrements();
    else
        /* pion2rad in motor variables */
        q = (4.0 * TWOPi / ResScrew) * 0.25 * ReadPositionInIncrements();
}

```

```

/*****/
/* execute function generator */
/*****/

fungenUpdateStates(&phase, frequency, h);
fungenOutputs(&FunGenOut, phase, amplitude, offset, waveform);

/*****/
/* some signal filtering */
/*****/

/* evaluate outputs */
{
    double ref_f;

    ref_f = alpha * ref_1 + (1-alpha) * FunGenOut;
    dotq = (q - mes_1) / h;
    dotr = (ref_f - ref_2) / (2 * h);
    ddotq = (q - 2.0 * mes_1 + mes_2) / (h * h);
    ddotr = (ref_f - 2.0 * ref_1 + ref_2) / (h * h);
    r = ref_1;
}

/* update states */
ref_2 = ref_1;
ref_1 = alpha * ref_1 + (1-alpha) * FunGenOut;
mes_2 = mes_1;
mes_1 = q;

/*****/
/* execute PID control algorithm */
/*****/

/* evaluate output */
u_pid = kp * (r - q);
if (D_on_off)
    u_pid += kp * Td * (dotr - dotq);
if (I_on_off)
    u_pid += u_i;

/* update state */
if (B0_or_BF) {
    if ((Ti != 0.0) && (I_on_off))
        u_i = u_i + kp * h * (r - q) / Ti;
    else
        u_i = 0.0;
}
if (ARW_on_off)

```

```

        u_i = sat(u_i, fabs(ARW_Level));
    } else
        u_i = 0.0;

/*
***** execute model based friction compensation control algorithm *****
***** */

/* evaluate friction compensation output */
switch ((int)comp_select) {

    case LUGRE_FF :
        u_c = Inertia * ddotr + s0 * hatz
            + s1 * ( dotr - hatz * fabs(dotr) / g(dotr) ) + s2 * dotr + F_g;
        hatdotz = ( dotr - hatz * fabs(dotr) / g(dotr) );
        break;

    case LUGRE_FB_LIN :
        u_c = Inertia * ddotr + s0 * hatz - s1 * hatz * fabs(dotq) / g(dotq)
            + (s2 + s1) * dotr + F_g;
        hatdotz = ( dotq - hatz * fabs(dotq) / g(dotq) );
        break;

    case KFM_FB_LIN :
        u_c = Inertia * ddotr + s0 * g(dotq) * signf(dotq)
            + (1 - fabs(signf(dotq))) * F_s * sign(u_pid + Inertia * ddotr)
            + s2 * dotr + F_g;
        hatdotz = 0.0;
        break;

    case LUENBERGER :
        hatdotq = xi_1 + l_1 * q;
        hatz = xi_2 + l_2 * q;

        u_c = Inertia * ddotr + s0 * hatz
            + s1 * ( hatdotq - hatz * fabs(hatdotq) / g(hatdotq) )
            + s2 * dotr + F_g + k_hatdotq * (dotr - hatdotq);

        hatdotz = (hatdotq - hatz * fabs(hatdotq) / g(hatdotq)) - l_2 * hatdotq;
        break;

    case NO_MODEL_BASED :
    default :
        u_c = 0.0;
        hatdotz = 0.0;
}

/*
* evaluate control action output */
if (B0_or_BF) {
    Control = u_pid + u_c;
} else {
    Control = FunGenOut;
}

```

```

}

Control = sat(Control, 1.34); /* Amplifier limitations */

/* update states */
if (B0_or_BF) {
    double a1, b0;

    switch ((int)comp_select) {

        case LUGRE_FF :
            if (0.0 != dotr) {
                a1 = -exp( -h * fabs(dotr) / g(dotr) );
                b0 = (1.0 + a1) * g(dotr) / fabs(dotr);
                hatz = -a1 * hatz + b0 * dotr;
            }
            hatdotq = dotq;
            break;

        case LUGRE_FB_LIN :
            if (0.0 != dotq) {
                a1 = -exp( -h * fabs(dotq) / g(dotq) );
                b0 = (1.0 + a1) * g(dotq) / fabs(dotq);
                hatz = -a1 * hatz + b0 * (dotq + klugre * (r - q));
            }
            hatdotq = dotq;
            break;

        case LUENBERGER :
            hatdotq = xi_1 + l_1 * q;
            hatz = xi_2 + l_2 * q;

            xi_1 += h * ( (Control - s0 * hatz
                           - s1 * (hatdotq - hatz * fabs(hatdotq) / g(hatdotq))
                           - s2 * hatdotq
                           - F_g) / Inertia - l_1 * hatdotq );

            if (0.0 != hatdotq) {
                a1 = -exp( -h * fabs(hatdotq) / g(hatdotq) );
                b0 = (1.0 + a1) * g(hatdotq) / fabs(hatdotq);
                xi_2 = -a1 * xi_2 + b0 * (hatdotq
                                           - fabs(hatdotq) / g(hatdotq) * l_2 * q
                                           - l_2 * hatdotq );
            }
            } break;

        case KFM_FB_LIN :
        case NO_MODEL_BASED :
        default :
            xi_1 = 0.0;
            xi_2 = 0.0;
            hatz = 0.0;
            hatdotq = dotq;
    }
}

```

```

        }

    /* **** */
    /* execute parameter adaptation law */
    /* **** */

    if ((B0_or_BF) && (LUGRE_FF == ((int)comp_select)) && (Adapt_on_off)) {
        hatF_g += h * alpha_g * u_pid;
        hats0 += h * alpha_0 * u_pid * hatdotz;
        hatF_c += h * alpha_c * u_pid * sign(hatz);

        Set(0,21, hatF_g);
        Set(0,23, hats0);
        Set(0,19, hatF_c);
    }

    /* **** */
    /* check for numerical problems (e.g. divisions by zero) */
    /* **** */

    for (cc=1; cc<NB_STATES; cc++)
        if (isnan(x[cc])) x[cc]=0.0;

    /* **** */
    /* output control action */
    /* **** */

    Control = Km * sat( Control / Km, MAXOUTPUT );
    DA(0, 0.5 * ((Control / Km) - DAOFFSET) );

    /* **** */
    /* store signal traces */
    /* **** */

    SetInternal(0, r); /* Reference position */
    SetInternal(1, q); /* Screw measurement */
    SetInternal(2, Control); /* Last applied torque */
    SetInternal(3, u_c); /* Compensator control action */
    SetInternal(4, hatz); /* Friction state */
    SetInternal(5, hatdotz); /* Derivative of friction state */

    return(0);
}

/*--- END OF FILE -----*/

```

Bibliography

- [1] F. Altpeter, F. Ghorbel, and R. Longchamp. A singular perturbation analysis of two friction models applied to a vertical EDM-axis. In *3rd IFAC Workshop on Motion Control*, pages 7–12, Grenoble, France, September 1998.
- [2] F. Altpeter, P. Myszkowski, M. Kocher, and R. Longchamp. Friction compensation: PID synthesis and state control. In *European Control Conf.*, session TH-M II, Brussels, July 1997.
- [3] F. Altpeter, P. Myszkowski, and R. Longchamp. Identification for control of drives with friction. In *Conf. on Contr. of Industrial Systems*, volume 1, pages 673–677, Belfort, France, May 1997.
- [4] F. Altpeter, D. Neculescu, and R. Longchamp. Friction modeling and identification issues for electric drives. In *Electromotion '97*, pages 149–154, Cluj-Napoca, Romania, May 1997.
- [5] B. Armstrong-Hélouvry. *Control of Machines with Friction*. Kluver Academic Publishers, Massachusetts, 1991.
- [6] B. Armstrong-Hélouvry. Stick slip and control in low-speed motion. *IEEE Trans. Autom. Control*, 38(10):1483–1496, October 1993.
- [7] B. Armstrong-Hélouvry and B. Amin. PID control in the presence of static friction: A comparison of algebraic and describing function analysis. *Automatica*, 32(5):679–692, 1996.
- [8] B. Armstrong-Hélouvry and C. Canudas de Wit. *The Control Handbook*, chapter Friction Modeling and Compensation, pages 1369–1382. CRC Press, 1996.
- [9] B. Armstrong-Hélouvry, P. Dupont, and C. Canudas de Wit. A survey of models, analysis tools and compensation methods for the control of machines with friction. *Automatica*, 30(7):1083–1138, 1994.
- [10] J. P. Aubin and A. Cellina. *Differential Inclusions*. A Series of Comprehensive Studies in Mathematics (264). Springer-Verlag, Berlin Heidelberg, 1984.
- [11] T. W. Barbee, L. Seaman, R. Crewdson, and D. Curran. Dynamic fracture criteria for ductile and brittle metals. *J. of Materials*, 7(3):393–401, 1972.

- [12] B. Bhushan. *Tribology and Mechanics of Magnetic Storage Devices*. Springer-Verlag, New York, 1990.
- [13] B. Bhushan. *The Engineering Handbook*, chapter Tribology: Friction, Wear, and Lubrication, pages 210–229. CRC Press, 1996.
- [14] P. J. Blau, editor. *ASM Handbook: Friction, Lubrication and Wear Technology*, volume 18. ASM International. The Materials Information Society, 1992.
- [15] P.-A. Bliman. *Etude Mathématique d'un modèle de frottement sec: le modèle de P. R. Dahl*. PhD thesis, Univ. Paris IX-Dauphine, U. E. R. Mathématiques de la décision, 1990.
- [16] P.-A. Bliman. Mathematical study of the Dahl's friction model. *European Journal of Mechanics, A/Solids*, 11(6):835–848, 1992.
- [17] P.-A. Bliman and M. Sorine. A system-theoretic approach of systems with hysteresis. application to friction modelling and compensation. In *European Control Conference*, volume 4, pages 1844–1849, Groeningen, 1993.
- [18] P.-A. Bliman and M. Sorine. Easy-to-use realistic dry friction models for automatic control. In *European Control Conference*, pages 3788–3794, Roma, 1995.
- [19] L. C. Bo and D. Pavelescu. The friction–speed relation and its influence on the critical velocity of stick–slip motion. *Wear*, 82:277–289, 1982.
- [20] F. P. Bowden and D. Tabor. The area of contact between stationary and between moving surfaces. *Proc. Royal Society of London, A* 169:391–413, 1938.
- [21] J.-M. Breguet and Ph. Renaud. A 4-degrees-of-freedom microrobot with nanometer resolution. *Robotica*, 14:199–203, 1996.
- [22] P. W. Bridgman. Shearing phenomena at high pressures, particularly in inorganic compounds. *Proc. American Academy of Arts and Sciences*, 71(9):387–460, January 1937.
- [23] B. J. Briscoe, B. Scruton, and F. R. Willis. The shear strength of thin lubricant films. *Proc. Royal Society of London, A* 333:99–114, 1973.
- [24] C. Canudas de Wit. Comments on “A new model for control of systems with friction”. *IEEE Trans. Autom. Control*, 43(8):1189–1190, August 1998.
- [25] C. Canudas de Wit and P. Lischinsky. Adaptive friction compensation with dynamic friction model. In *IFAC World Cong.*, volume E, pages 197–202, San Francisco, 1996.
- [26] C. Canudas de Wit, H. Olsson, K. J. Åström, and P. Lischinsky. Dynamic friction models and control design. In *American Control Conf.*, pages 1920–1926, San Francisco, 1993.

- [27] C. Canudas de Wit, H. Olsson, K. J. Åström, and P. Lischinsky. A new model for control of systems with friction. *IEEE Trans. Autom. Control*, 40(3):419–425, March 1995.
- [28] F. E. Cellier, H. Elmquist, and M. Otter. *The Control Handbook*, chapter Modeling from Physical Principles, pages 99–108. CRC Press, 1996.
- [29] T. Conus. Projet de 8ème semestre: Entraînement ‘stick-slip’ avec actionneur piezo. Technical Report 50324, Institut d’Automatique, Ecole Polytechnique Fédérale de Lausanne, 1997.
- [30] J. S. Courtney-Pratt and E. Eisner. The effect of tangential force on the contact of metallic bodies. *Proc. Royal Society of London, A* 238:529–549, 1956.
- [31] J. F. Cuttino and T. A. Dow. Contact between elastic bodies with an elliptic contact interface in torsion. *Trans. ASME: J. of Applied Mechanics*, 64(1):144–148, March 1997.
- [32] P. R. Dahl. Solid friction damping of spacecraft oscillations. In *AIAA Guidance, Navigation and Control Conf*, AIAA Paper No. 75-1104, Boston, 1975.
- [33] P. R. Dahl. Measurement of solid friction parameters of ball bearings. In *6th Annual Symposium on Incremental Motion Control Systems and Devices*, pages 49–61, U. of Illinois, May 1977.
- [34] C. A. de Coulomb. *Théorie des machines simples, en ayant égard au frottement de leurs parties et à la roideur des cordages*. Bachelier Librairie, Quai des Augustins, Paris, 1781. Nouvelle édition, 1821.
- [35] C. A. Desoer and M. Vidyasagar. *Feedback Systems: Input–Output Properties*. Academic Press Replica Reprint, New York, 1975.
- [36] D. D. DiBitonto, P. T. Eubank, M. R. Patel, and M. A. Barrufet. Theoretical models of the electrical discharge machining process. I a simple cathode erosion model. *J. Appl. Phys*, 66(9):4095–4103, November 1989.
- [37] D. Dowson. *History of Tribology*. Longman Inc., New York, 1979.
- [38] D. Dowson, G. R. Higginson, J. F. Archard, and A. W. Crook. *Elasto-hydrodynamic Lubrication, SI Edition*. Pergamon Press, Oxford, 1977.
- [39] P. E. Dupont and E. P. Dunlap. Friction modeling and control in boundary lubrication. In *American Control Conf.*, pages 1910–1914, San Francisco, 1993.
- [40] H. Elmquist, F. E. Cellier, and M. Otter. Object-oriented modeling of hybrid systems. In *Europ. Simulation Symposium*, Delft, 1993.
- [41] H. A. Francis. Application of spherical indentation mechanics to reversible and irreversible contact between rough surfaces. *Wear*, 45:221–269, 1977.

- [42] C. Ganseman, J. Swevers, T. Prajogo, and F. Al-Bender. An integrated friction model with improved presliding behaviour. In *Symposium on Robot Control*, pages 159–164, Nantes, France, September 1997.
- [43] P. Gawthrop and L. Smith. *Metamodelling: For Bond Graphs and Dynamic Systems*. Prentice Hall Int. Ltd, Hertfordshire, UK, 1996.
- [44] M. Goldfarb and N. Celanovic. Modeling piezoelectric stack actuators for control of micromanipulation. *IEEE Contr. Syst. Magazine*, 17(3):69–79, June 1997.
- [45] J. A. Greenwood and J. B. P. Williamson. Contact of nominally flat surfaces. *Proc. of the Royal Society of London*, 295:300–319, April 1966.
- [46] P. Guillaume, R. Pintelon, and J. Schoukens. Nonparametric frequency response function estimators based on nonlinear averaging techniques. In *IEEE Conf. Instrumentation and Measurements Technology*, pages 3–9, New York, May 1992.
- [47] T. Gyalog, M. Bammerlin, R. Lüthi, E. Meyer, and H. Thomas. Mechanism of atomic friction. *Europhysics Letters*, 31(5-6):269–274, 1995.
- [48] D. A. Haessing and B. Friedland. On the modeling and simulation of friction. *Trans. ASME: J. of Dynamic Systems, Measurement, and Control*, 113(3):354–362, September 1991.
- [49] K. Hamiti, A. Voda-Besançon, and H. Roux-Buisson. Position control of a pneumatic actuator under the influence of stiction. *Contr. Engr. Practice*, 4(8):1079–1088, 1996.
- [50] A. Harnoy, B. Friedland, and H. Rachoor. Modeling and simulation of elastic and friction forces in lubricated bearings for precise motion control. *Wear*, 172:155–165, 1994.
- [51] D. P. Hess and A. Soom. Friction at a lubricated line contact operating at oscillating sliding velocities. *Trans. ASME: J. of Tribology*, 112(1):147–152, January 1990.
- [52] F. Holzweissig and H. Dresig. *Lehrbuch der Maschinendynamik*. Fachbuchverlag Leipzig GmbH, Leipzig, 3rd edition, 1992.
- [53] C. Hsieh and J.-C. Lin. Micro dynamic stiction model and control of a hub-appendage type system. In *ASME Design Engineering Technical Conferences*, DETC97/VIB-3784, Sacramento, 1997.
- [54] C. Hsieh and Y.-C. Pan. Modeling of static friction and the analysis of integral controls for precision positioning. Personal communication, January 1997.
- [55] W. D. Iwan. A distributed-element model for hysteresis and its steady-state dynamic response. *Trans. ASME: J. of Applied Mechanics*, 88:893–900, December 1966.

- [56] M. Iwasaki and N. Matsui. Observer-based nonlinear friction compensation in servo drive system. In *4th Int. Workshop Advanced Motion Contr.*, pages 344–348, Tsu-City, Japan, March 1996.
- [57] C. F. Jenkin. A mechanical model illustrating the behaviour of metals under static and alternating loads. *Engineering*, 114:603, November 1922.
- [58] D. Karnopp. Computer simulation of stick-slip friction in mechanical dynamic systems. *Trans. ASME: J. of Dynamic Systems, Measurement, and Control*, 107(1):100–103, March 1985.
- [59] S. Kato, N. Sato, and T. Matsubayashi. Some considerations on characteristics of static friction in machine tool slideway. *Trans. ASME: J. of Lubrication Technology*, 94:234–247, July 1972.
- [60] H. K. Khalil. *Nonlinear Systems*. Macmillan Publishing Company, New York, 1992.
- [61] T. Kubo, G. Anwar, and M. Tomizuka. Application of nonlinear friction compensation to robot arm control. In *IEEE Int. Conf. Robotics and Automation*, pages 722–727, San Francisco, 1986.
- [62] P. A. Lischinsky. *Compensation de frottement et commande en position d'un robot hydraulique industriel*. PhD thesis, Laboratoire d'Automatique de Grenoble, Inst. National Polytechnique de Grenoble, 1997.
- [63] L. Ljung. *System Identification*. Prentice-Hall, Inc., Englewood Cliffs, New Jersey, 1987.
- [64] D. G. Luenberger. An introduction to observers. *IEEE Trans. Autom. Control*, AC-16(6):596–602, 1971.
- [65] R. Lüthi, E. Meyer, M. Bammerlin, L. Howald, H. Haefke, T. Lehmann, C. Lop-pacher, H.-J. Güntherodt, T. Gyalog, and H. Thomas. Friction on the atomic scale: An ultrahigh vacuum atomic force microscopy study on ionic crystals. *J. Vac. Sci. Technol.*, B 14(2):1280–1284, 1996.
- [66] H. Matsukawa and H. Fukuyama. Theoretical study of friction: One-dimensional clean surfaces. *Physical Review*, B 49(24):17286–17292, June 1994.
- [67] E. Meyer, R. Lüthi, L. Howald, M. Bammerlin, L. Scandella, J. Gobrecht, A. Schumacher, and R. Prins. Friction force spectroscopy. In *Proc. of the NATO Advanced Research Workshop and Adriatico Research Conf. on Physics of Sliding Friction*, pages 349–367, Miramare, Trieste, Italy, June 1996.
- [68] R. D. Mindlin. Compliance of elastic bodies in contact. *J. of Applied Mechanics*, 16:259–268, 1949.
- [69] H. Motohisa and S. Kazumasa. Atomistic locking and friction. *Physical Review*, B 41(17):11837–11851, June 1990.

- [70] P. R. Nayak. Random process model of rough surfaces. *Trans. ASME: J. of Lubrication Technology*, 93(3):398–407, July 1971.
- [71] D. O'Regan. *Existence Theory for Nonlinear Ordinary Differential Equations*. Kluwer Academic Publishers, Dordrecht, The Netherlands, 1997.
- [72] N. A. Osborne and D. L. Rittenhouse. The modeling of friction and its affects on fine pointing control. In *AIAA Guidance, Navigation and Control Conf*, AIAA Paper No. 74-875, Anaheim, 1974.
- [73] M. Otter. *Objektorientierte Modellierung mechatronischer Systeme am Beispiel geregelter Roboter*. PhD thesis, DLR Oberpfaffenhofen, VDI-Verlag GmbH, Düsseldorf, Reihe 20, Nr. 147, 1995.
- [74] M. R. Patel, M. A. Barrufet, P. T. Eubank, and D. D. DiBitonto. Theoretical models of the electrical discharge machining process. II the anode erosion model. *J. Appl. Phys.*, 66(9):4104–4111, November 1989.
- [75] D. W. Pohl. Dynamic piezoelectric translation devices. *Rev. Sci. Instrum.*, 58(1):54–57, January 1987.
- [76] K. Popp and P. Stelter. Stick-slip vibrations and chaos. *Phil. Trans. Royal Society of London, A* 332:89–105, 1990.
- [77] E. Rabinowicz. *Friction and Wear of Materials*. John Wiley & Sons, Inc, New York, 2nd edition, 1995.
- [78] E. Rabinowicz and D. Tabor. Metallic transfer between sliding metals: an autoradiographic study. *Proc. Royal Society of London, A* 208:455–475, 1951.
- [79] K. P. Rajurkar and W.-M. Wang. Advances in EDM monitoring and control systems using modern control concepts. *Int. J. Electrical Machining*, 2(2):1–8, January 1997.
- [80] Ch. Renner, Ph. Niedermann, A. D. Kent, and Ø. Fischer. A vertical piezoelectric inertial slider. *Rev. Sci. Instrum.*, 61(3):965–967, March 1990.
- [81] O. Reynolds. On the theory of lubrication. *Proc. Royal Society of London*, 177:157–234, 1886.
- [82] J. R. Rice and A. L. Ruina. Stability of steady frictional slipping. *Trans. ASME: J. of Applied Mechanics*, 50(2):343–349, June 1983.
- [83] J.-A. Ruan and B. Bhushan. Atomic-scale friction measurements using friction force microscopy: Part I — general principles and new measurement techniques. *Trans. ASME: J. of Tribology*, 116:378–388, April 1994.
- [84] R. J. Rumpel. On the qualitative behaviour of nonlinear oscillators with dry friction. *Zeitschrift für angewandte Mathematik und Mechanik*, 76(Suppl. 2):665–666, 1996.

- [85] C. Salzmann, D. Gillet, R. Longchamp, and D. Bonvin. Framework for fast real-time applications in automatic control education. In *4th IFAC Symposium on Advances in Control Education*, pages 345–350, Istanbul, Turkey, 1997.
- [86] J. B. Sampson, F. Morgan, D. W. Reed, and M. Muskat. Studies in lubrication: Friction behaviour during the slip portion of the stick-slip process. *J. of Applied Physics*, 14:689–700, December 1943.
- [87] U. D. Schwarz, H. Bluhm, H. Hölscher, W. Allers, and R. Wiesendanger. Friction in the low-load regime: Studies on the pressure and direction dependence of frictional forces by means of friction force microscopy. In *Proc. of the NATO Advanced Research Workshop and Adriatico Research Conf. on Physics of Sliding Friction*, pages 369–402, Miramare, Trieste, Italy, June 1996.
- [88] G. Spinnler. *Conception des Machines*, volume 1. Presses Polytechniques et Universitaires Romandes, Lausanne, 1994.
- [89] J. S. Stevens. Some experiments in molecular contact. *The Physical Review*, 8(1):49–53, 1899.
- [90] R. Stribeck. Die wesentlichen Eigenschaften der Gleit- und Rollenlager. *Zeitschrift des Vereins Deutscher Ingenieure*, 46(36,38):1341–1348,1432–1438, 1902.
- [91] S. Thomas. Vibrations damped by solid friction. *Philosophical Magazine and J. of Science*, 9(57):329–345, March 1930.
- [92] G. A. Tomlinson. A molecular theory of friction. *Philosophical Magazine and J. of Science*, 7(46):905–939, June 1929.
- [93] A. Tustin. The effects of backlash and of speed-dependent friction on the stability of closed-cycle control systems. *J. of the Institution of Electrical Engineers*, 94(2A):143–151, 1947.
- [94] P. Vedagarbha, D. M. Dawson, and M. Feemster. Tracking control of mechanical systems in the presence of nonlinear dynamic friction effects. In *American Control Conf.*, pages 2284–2288, Albuquerque, 1997.
- [95] P. Vedagarbha, D. M. Dawson, and M. Feemster. Tracking control of mechanical systems in the presence of nonlinear dynamic friction effects. Personal communication, September 1997.
- [96] Verein Schweizerischer Maschinen-Industrieller, Normenbüro (éd.). *Norme Suisse SN 237550 Usinage par électro-érosion: 1–1980, 2–1980 and 3–1983*.
- [97] A. Visintin. *Differential Models of Hysteresis*. Springer-Verlag, Berlin, 1994.
- [98] W. Weibull. A statistical distribution function of wide applicability. *Trans. ASME: J. of Applied Mechanics*, 18:293–297, September 1951.

- [99] M. Weiss and F. J. Elmer. *Physics of Sliding Friction*, chapter A Simple Model for Wearless Friction: The Frenkel–Kontorova–Tomlinson Model, page 163 ff. Kluwer Academic Publishers, 1996.
- [100] J. A. Williams. *Engineering Tribology*. Oxford University Press Inc, New York, 1994.
- [101] P. Young. *Recursive Estimation and Time-Series Analysis*. Springer Verlag, Berlin, 1984.
- [102] G. Zambelli and L. Vincent. *Matériaux et contacts: Une approche tribologique*. Presses Polytechniques et Universitaires Romandes, Lausanne, Switzerland, 1998.
- [103] G. Zames. On the input–output stability of time-varying nonlinear feedback systems. Part I: Conditions derived using concepts of loop gain, conicity and positivity. *IEEE Trans. Autom. Control*, 11(2):228–238, April 1966.

Curriculum Vitae

Friedhelm ALTPETER

Haus Arno

3952 Susten (VS), Switzerland

e-mail: friedhelm.altpeter@ieee.org

Born in Hannover (Germany) on March 8, 1968.

Nationality: Swiss.

Languages: German (mother tongue), French, English.

Hobbies: mountaineering, jogging.



Education

1983–1988 *Kollegium Spiritus Sanctus* Brig, Maturity: science (University entrance).

1988–1993 *École polytechnique fédérale de Lausanne, Section microtechnique*. Multi-disciplinary field which includes mechanical engineering, automation, electronics engineering and production techniques.

1993–1999 *École polytechnique fédérale de Lausanne, Institut d'automatique*. PhD student, research and teaching assistant.

Technical Experience

1989–1991 During studies, trainee with **ALUSUISSE**, Sierre

1989 (6 weeks): Machining techniques

1990 (14 weeks): Thermal treatments and the properties of aluminum

1991 (8 weeks): Quality System ISO-9000

1993–1999 Setup and maintaining of the acquisition system ‘Experimental Frequency Response’ for the student’s laboratory.

1994–1999 Collaboration with **Charmilles Technologies S.A.** (Meyrin, Switzerland): Control of an electrical discharge machining axis (die sinking).

1996–1999 Development of a high precision real-time architecture for **MacOS**, based on programmable logic devices (AMD families MACH4xx and MACH5xx).

List of Publications

- [AARTC-95] F. Altpeter, Ch. Salzmann, D. Gillet and R. Longchamp, A General Instrument for Real-Time Control and Data Acquisition. In *IFAC Workshop on Algorithms and Architectures for Real-Time Control*, pages 323–327, Ostend, Belgium, May 31–June 2, 1995.
- [RAM-95] F. Ghorbel, F. Altpeter and R. Longchamp, Integral Manifold Control of a Mechanical System with a Flexible Shaft. In *Int. Conf. on Recent Advances in Mechatronics*, pages 722–727, Istanbul, August 14–16, 1995.
- [MC-95] F. Altpeter, F. Ghorbel and R. Longchamp, Control of Drives with Flexible Transmission. In *IFAC Workshop on Motion Control*, pages 315–322, Munich, October 9–11, 1995.
- [EM-97] F. Altpeter, D. Neculescu and R. Longchamp, Friction Modeling and Identification Issues for Electric Drives. In *Electromotion '97*, pages 149–154, Cluj-Napoca, Romania, May 8–9, 1997.
- [CIS-97] F. Altpeter, P. Myszkowski and R. Longchamp, Identification for Control of Drives with Friction. In *IFAC Conf. on Control of Industrial Systems*, volume 1, pages 673–677, Belfort, France, May 20–22, 1997.
- [IAS-97] F. Altpeter, R. Longchamp and F. Kaestli, Charmilles-EPFL : les étincelles d'une collaboration fructueuse. *Ingénieurs et Architectes Suisses*, 123(15):326–329, 1997.
- [ECC-97] F. Altpeter, P. Myszkowski, M. Kocher and R. Longchamp, Friction Compensation: PID Synthesis and State Control. In *European Control Conference*, Session TH-M 11, Paper No. ECC192, Brussels, Belgium, July 1–4, 1997.
- [ISEM-98] F. Altpeter, J. Cors, M. Kocher and R. Longchamp, EDM Modeling for Control. In *12th Int. Symp. for Electromachining*, pages 149–155, Aachen, Germany, VDI Berichte 1405, May 11–13, 1998.
- [MC-98] F. Altpeter, F. Ghorbel, R. Longchamp, A Singular Perturbation Analysis of Two Friction Models Applied to a Vertical EDM-Axis. In *3rd IFAC Workshop on Motion Control*, pages 7–12, Genoble, France, September 21–23, 1998.
- [CDC-98] F. Altpeter, F. Ghorbel, R. Longchamp, Relationship Between Two Friction Models: A Singular Perturbation Approach. In *37th IEEE Conf. on Decision and Control*, pages 1572–1574, Tampa, Florida, USA, December 16–18, 1998.

Index

- \mathcal{L}_2 -gain, 63
- Adaptive control, 79, 108, 113
- Area of contact
 - apparent, 10
 - real, 10, 13
- Attraction
 - domain of, 56
- Autonomous system, 50
- Bandwidth, 69, 110
- Barbalat's lemma, 65
- Bearing
 - ball, 92, 108
 - journal, 15
 - linear roller, 2
 - preloaded, 79, 92, 104
 - rolling contact, 15
 - V-bearing, 93, 96
- Bode diagram, 68, 110
- Bond graph, 98, 123
- Break-away, 14, 16, 19, 24, 26
- Cascaded control loops, 48, 66, 76
- Characteristic
 - space constant, 34, 36, 39, 67, 75, 97, 108
 - velocity, 25, 37
- Chattering, 88
- Contact
 - Hertz, 12, 100
 - model, 11–13
- Coulomb, 17
 - level, see *kinetic friction level*
 - model, see *friction model KFM*
- Dahl, 20, 28, 44, 97
 - curve, see *friction force–position relationship*
- Deviation variables, 43, 50, 107
- Die sinking EDM, 101
- Differential algebraic equations, 123–126
- Digital implementation, 76, 85, 127
- Eigenfrequency, 68
- Electrical discharge machining
 - complete control structure, 104
 - process description, 102
 - technology, 101
- Equilibrium point, 53, 56
- Feedback compensation, see *input–output linearization*
- Feedforward compensation
 - LuGre* model based, 75, 113
 - adaptive, 79
 - KFM based, 74
- Frequency response, 41
- Friction
 - definition, 1
 - model
 - bristle, 29
 - integrated, 23, 100
 - kinetic (KFM), 24–27
 - Lund–Grenoble *LuGre*, 27–33
 - position–force relationship, 20, 33, 44, 107
 - state
 - bounded, 30
 - observer, 81–85
 - predictor, 76
 - velocity–force characteristics, 14, 15, 37, 40, 54–56, 80, 92, 105
- Grease, 92
- Greenwood and Williamson, 11
- Han-window, 42

- High speed, see *regime*
- Hunting, see *phenomena*
- Hurwitz, 53, 78
- Identification
 - Box-Jenkins, 43
 - instrumental variable method, 43
 - intercorrelation method, 41
 - least-squares algorithm, 43
 - mean quadratic prediction error, 41
- Impulse response, 51
- Induced norm
 - infinity, 51, 78
 - one, 52
- Inertial slider actuators, 93
- Initial value problem, 30
- Input–output linearization
 - LuGre* model based, 88, 114
 - KFM based, 86, 116
- Jacobian, 53
- Kalman–Yakubovic–Popov lemma, 59
- Kalman–Yakubovich–Popov lemma, 71
- Karnopp, 27
- KFM, see *friction model KFM*
- Kinetic friction level, 14, 24, 81
- LaSalle’s theorem, 70–71
- Linearization, 53
- Lubrication
 - definition, 1
 - regimes, 13–16
 - selection, 92
- Luenberger, 82–85, 115
- LuGre*, see *friction model LuGre*
- Mechanical time constant, 68
- Micro-manipulators, 93
- Microscopy, 93
- Motion
 - aperiodic/chaotic, 56
 - regular, 50
 - unidirectional, 35, 63
- Object oriented modeling, 123
- Oil, 92
- Orbit, 56
- Ordinary differential equations, 123–126
- Parseval’s theorem, 64
- Passivity, 30–32, 69
- Performance index, 109
 - local transient, 67
- Phenomena
 - hunting, 66, 69, 112
 - input–output, 28
 - normal force, 12
 - stick–slip motion, 26, 48, 95, 110
 - stop time, 49
 - velocity regimes, 13–16
- Piezoactuator, 93
 - model, 99
- Positive invariant set, 57, 63
- Positive real, 59, 71
- Preisach model, 33
- Presliding, see *regime*
- Quadrature glitch, 113, 115
- Quantization noise, 42
- Real-time task, 127
- Regime
 - high speed, 41, 67
 - presliding, 17, 19, 42, 68, 106
- Reversal point memory, 33, 92
- Robustness
 - parameter uncertainties, 77
- Root-locus (closed-loop), 53
- Settling time, 66
- Shear strength, 15, 17, 19, 20, 98
- Simple drive, 3
- Singular perturbation, 33–38
- Small gain theorem, 65
- Smart design, 93
- Stability
 - boundary layer, 36
 - experimental illustration, 113
 - global, 50
 - global asymptotic, 56, 69
 - local, 84
 - local asymptotic, 53, 67

- ultimate, 57
- Static friction level, 19, 24, 97
- Step response, 109, 110
- Stick-slip motion, see *phenomena*
- Stiffness at rest, 18–19, 81, 97
- Stribeck, 13
- Surface topology, 97
- Taylor, 83
- Tikhonov, 35
- Triangle inequality, 64
- Tribology, 1, 9
- Wear, 1
- Wire EDM, 102